



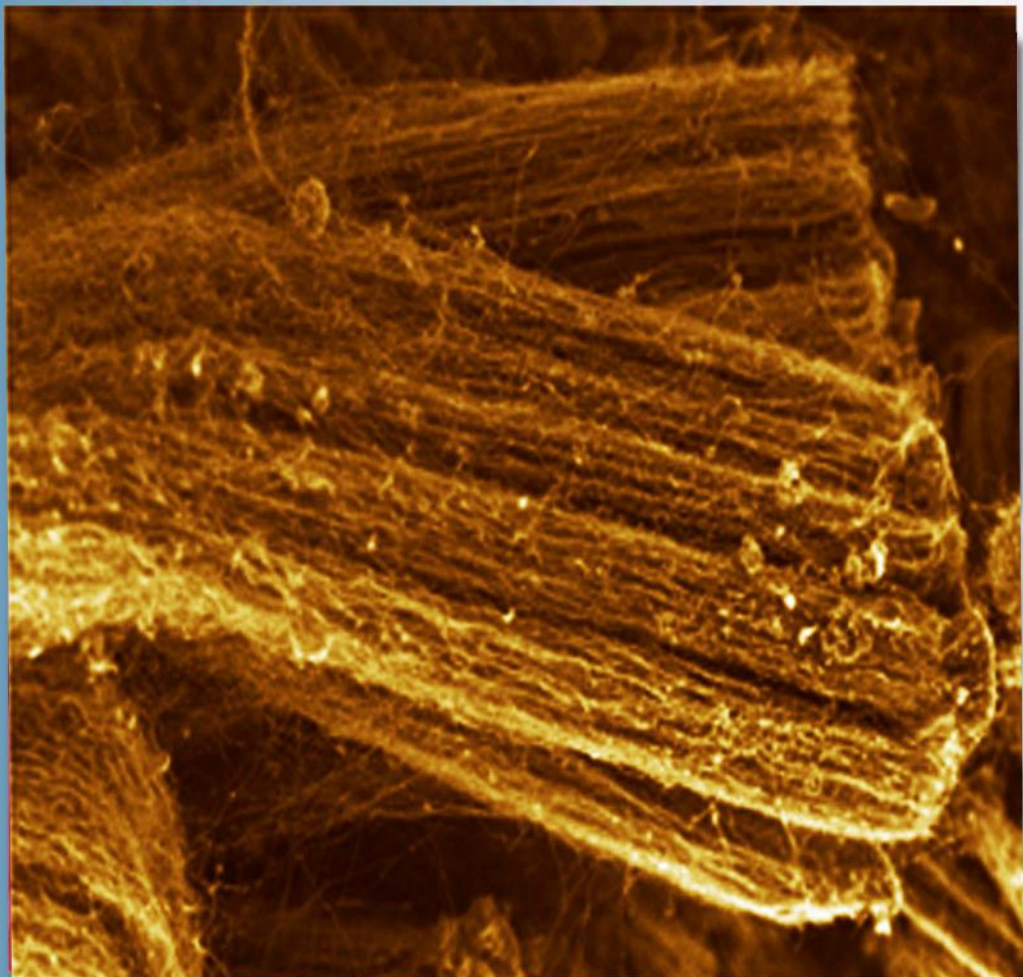
ISSN 1028-8546

Volume XXVII Number 2
Section: En July, 2021

Azerbaijan Journal of Physics

Fizika

www.physics.gov.az
jophphysics.wixsite.com/ajpphysics
www.physics.gov.az/ajpfizika.html



Institute of Physics
Azerbaijan National Academy of Sciences
Department of Physical, Mathematical and Technical Sciences

Published from 1995
Ministry of Press and Information
of Azerbaijan Republic,
Registration number 514, 20.02.1995

ISSN 1028-8546
vol. XXVII, Number 02, 2021
Series: En

Azerbaijan Journal of Physics

FIZIKA

*Institute of Physics
Azerbaijan National Academy of Sciences
Department of Physical, Mathematical and Technical Sciences*

HONORARY EDITORS

Arif PASHAYEV

EDITORS-IN-CHIEF

Arif HASHIMOV

Chingiz QAJAR

SENIOR EDITOR

Talat MEHDIYEV

INTERNATIONAL REVIEW BOARD

Ivan Scherbakov, Russia
Kerim Allahverdiyev, Azerbaijan
Mehmet Öndr Yetiş, Turkey
Gennadii Jablonskii, Belarus
Rafael Imamov, Russia
Vladimir Man'ko, Russia
Eldar Salayev, Azerbaijan
Dieter Hochheimer, USA
Victor L'vov, Israel

Vyacheslav Tuzlukov, South Korea
Majid Ebrahim-Zadeh, Spain
Anatoly Boreysho, Russia
Mikhail Khalin, Russia
Hasan Bidadi, Tebriz, Iran
Natiq Atakishiyev, Mexico
Arif Hashimov, Azerbaijan
Javad Abdinov, Azerbaijan

Tayar Djafarov, Azerbaijan
Salima Mehdiyeva, Azerbaijan
Talat Mehdiyev, Azerbaijan
Ayaz Bayramov, Azerbaijan
Tofiq Mammadov, Azerbaijan
Shakir Nagiyev, Azerbaijan
Rauf Guseynov, Azerbaijan
Yusif Asadov, Azerbaijan

TECHNICAL EDITORIAL BOARD

Senior secretary: Elmira Akhundova; Nazli Huseynova, Gulnura Jafarova
Nigar Akhundova, Elshana Aleskerova, Rena Nayimbayeva

PUBLISHING OFFICE

131, H. Javid ave., AZ-1143, Baku
ANAS, Institute of Physics

Tel.: (99412) 539-51-63, 539-32-23
Fax: (99412) 537-22-92
E-mail: jophphysics@gmail.com
Internet: www.physics.gov.az
<https://jophphysics.wixsite.com/ajpphysics>

Published at " _____ "
_____ str., Baku

Sent for printing on: _____. _____. 201_
Printing approved on: _____. _____. 201_
Physical binding: _____
Number of copies: _____ 200
Order: _____

It is authorized for printing:

SPECTRUM OF LASER PULSES IN THE FIRST ORDER DISPERSION THEORY**Sh.Sh. AMIROV***Faculty of Physics, Baku State University, 23 Z. Khalilov str., Az-1148, Baku, Azerbaijan
Department of Medical and Biological Physics, Azerbaijan Medical University**167 S.Vurgun str., Az-1022, Baku, Azerbaijan**Department of Physics and Electronics, Khazar University, 41 Mahsati str., Az 1096,
Baku, Azerbaijan**E-mail: phys_med@mail.ru*

Analytic expression for the spectral density of ultra short laser pulses in metamaterials (NIM) in the first order dispersion theory was obtained. Effects of group velocity delay (GVD), the phase detuning as well as the phase modulation on the spectral density of signal wave are theoretically studied. Narrowing of the spectrum of signal wave and shift of its maxima toward smaller values of frequency with increase in the GVD are observed. At characteristic lengths differ from zero maxima of spectral density are obtained not at zero values of frequency but at its different values. It is shown, that an increase in phase detuning leads to decrease in the maxima of spectral density as well as to their shift toward larger values of frequency modulation parameter, but increase in group velocity delay leads to increase in the maxima and shift toward smaller values of frequency modulation parameter for the same phase detuning.

Keywords: Metamaterials, first order dispersion, group velocity delay, phase modulated pulse.

PACS:78.67.Pt; 42.65-k; 42.62.Hk; 42.70-a

1. INTRODUCTION

Amplification of weak signals and extension the radiation frequency range of laser requires the development of optical parametric amplifiers. An interest to development of powerful sources of light pulses of femtosecond duration is related to the analysis of nonstationary interaction of ultra short pulses. First theoretical investigations on the parametric amplifiers have been carried out by S.A. Akhmanov and R.V. Khokhlov [1]. The character of interaction of modulated waves significantly depends on the dispersion properties of medium. The frequency conversion for the ultra short pulses with running wave was considered in [2].

The negative index materials (NIM) are attractive due to specifics of their interaction with electromagnetic waves. Different signs of refractive index correspond to different frequency intervals of the interacting waves. Therefore the energy fluxes of the waves with a positive sign of refractive index will propagate in opposite direction to those with frequencies corresponding to a negative sign of refractive index. The dynamics of three wave interaction in NIM was considered for the case of second harmonic generation in [3]. Results obtained in [4,5] are being used for the developments the metamaterials in the near IR and visible ranges of the spectrum. Earlier we have analyzed the efficiency of energy conversions between two direct waves with respect to the energy of the backward signal wave for the case of signal-wave amplification in metamaterials [6] in the constant intensity approximation (CIA) [7], taking into account the reverse reaction of excited wave on the exciting one. By employing the CIA we have studied the parametric interaction of optical waves in metamaterials under low-frequency pumping in the case of a negative index at a signal wave frequency [8].

The transition processes in the first order dispersion theory in the medium with quadratic nonlinearity have been analyzed by authors [9,10,11,12]. Earlier we have employed CIA to study the optical parametric amplification in stationary case [13] in the Fabri-Perrot cavity. Character of interaction of modulated wave significantly depends on the dispersion properties of a medium upon reduction of the pulse duration. The frequency conversion for the ultra-short pulses with running wave was analyzed in [14]. Earlier in [15] we were studied influence of group velocity delay (GVD) as well as group velocity dispersion (GVD) to the generation of sum frequency of ultra-short pulses in an external cavity under the phase matching and absence of linear losses. Latest times investigation of the four-wave interaction in metamaterials became actual. Analysis carried out in the CIA showed that in the metamaterial where the four-wave interaction occurs the optimum thickness of medium depends not only on the phase detuning and intensity of the pump wave but also on the intensity of a weak wave as well as the medium losses [16]. Efficiency of interaction between ultra short waves depends on the dispersion properties of the medium. Since metamaterials possess negative refractive index phase velocities are in the same direction distinctly from the group velocities. In the dispersive medium difference between velocities of frequency components leads to the distortion of the pulse shape. This becomes more pronounced for the pulses with femtosecond duration. Analysis of the frequency transformation of laser pulses in metamaterials was carried out by us in the second order dispersion theory [17]. To study frequency transformation in metamaterials the CIA method was employed in [18-21]. Four wave parametrical interaction of waves in metamaterials was studied in [21].

To study the three –wave parametric interaction in metamaterials in the first order dispersion theory is the goal of this paper.

2. THEORY AND DISCUSSIONS

It is assumed that waves interact in nonlinear medium when two pump and weak waves advance in the positive direction of z-axis ($z = 0$) and the signal wave propagates in the opposite direction of the axis from ($z = l$) input surface. During this interaction the

energy exchange between occurs between pump ($A_2(t, z)$), weak ($A_3(t, z)$) and signal ($A_1(t, z)$) waves and this wave is parametrically amplified. Dielectric permittivity and magnetic permeability of the medium at the frequency of signal wave are negative but those are positive at frequencies ω_2 and ω_3 for the pump and weak waves respectively.

Three-wave interaction of waves in the second order dispersion theory is described by the following set of truncated equations [1].

$$\begin{aligned} \left(\frac{\partial(z, t)}{\partial z} + \frac{1}{u_1} \frac{\partial}{\partial t} - i \frac{g_1}{2} \frac{\partial^2}{\partial t^2} + \delta_1 \right) A_1 &= i\gamma_1 A_3 A_2^* e^{i\Delta z} \\ \left(\frac{\partial}{\partial z} + \frac{1}{u_2} \frac{\partial}{\partial t} - i \frac{g_2}{2} \frac{\partial^2}{\partial t^2} + \delta_2 \right) A_2 &= -i\gamma_2 A_3 A_1^* e^{i\Delta z} \\ \left(\frac{\partial}{\partial z} + \frac{1}{u_3} \frac{\partial}{\partial t} - i \frac{g_3}{2} \frac{\partial^2}{\partial t^2} + \delta_1 \right) A_3 &= -i\gamma_3 A_1 A_2 e^{-i\Delta z} \end{aligned} \quad (1)$$

Here A_j ($j=1-3$) are the complex amplitudes of a signal, pump and idler waves respectively, δ_j – are the absorption coefficients of the medium at frequencies ω_j ($j=1-3$), u_j – are the group velocities of the interacting waves, $\Delta = k_1 - k_2 - k_3$ is the phase mismatch between the interacting waves, $g_j = \partial^2 k_j / \partial \omega_j^2$ is the dispersion of group velocities and

$\gamma_1, \gamma_2, \gamma_3$, are the coefficients of nonlinear coupling. Since we study the problem in the first order dispersion theory the second order derivatives will disappear in above equations. In addition if consider the amplitude of pump wave to be fixed ($A_2 = A_{20} = const.$) then we can rewrite:

$$\begin{aligned} \left(\frac{\partial(z, t)}{\partial z} + \frac{1}{u_1} \frac{\partial(z, t)}{\partial t} + \delta_1 \right) A_1 &= i\gamma_1 A_3 A_2^* e^{i\Delta z} \\ \left(\frac{\partial(z, t)}{\partial z} + \frac{1}{u_3} \frac{\partial(z, t)}{\partial t} + \delta_3 \right) A_3 &= -i\gamma_3 A_1 A_2 e^{-i\Delta z} \end{aligned} \quad (2)$$

If we introduce new variables $\eta = t - \frac{z}{u_1}$, $v = 1/u_3 - 1/u_1$ (is a group velocity delay) we get following system with respect to z and η .

$$\begin{aligned} \left(\frac{\partial(z, \eta)}{\partial z} - \delta_1 \right) A_1(z, \eta) &= i\gamma_1 A_3(z, \eta) A_2^* e^{i\Delta z} \\ \left(\frac{\partial(z, \eta)}{\partial z} - v \frac{\partial(z, \eta)}{\partial \eta} + \delta_3 \right) A_3(z, \eta) &= -i\gamma_3 A_1(z, \eta) A_2 e^{-i\Delta z} \end{aligned} \quad (3)$$

Employment the Fourier transformation $A_{1,2}(z, \eta) = \int_{-\infty}^{+\infty} A_{1,2}(z, \omega) e^{-i\omega\eta} d\omega$ to the system yields

$$\begin{aligned} \left(\frac{\partial(z, \omega)}{\partial z} - \delta_1 \right) A_1(z, \omega) &= i\gamma_1 A_3(z, \omega) A_2^* e^{i\Delta z} \\ \left(\frac{\partial(z, \omega)}{\partial z} + i\omega v + \delta_3 \right) A_3(z, \omega) &= -i\gamma_3 A_1(z, \omega) A_2 e^{-i\Delta z} \end{aligned} \quad (4)$$

Solving the system (4) according to the problem boundary conditions $A_1(z = l) = 0$ and $A_{2,3}(z = 0) = A_{20} A_{30}$ yields for the complex amplitude of signal wave $A_1(z, \omega)$ ($\delta_i = 0$)

$$A_1(\omega, z) = \frac{i\gamma_1 A_{20} A_{30}}{\lambda - h \tan \lambda l} (\sin \lambda z - \tan \lambda l \cdot \cos \lambda z) e^{-hz} \quad (5)$$

where $\lambda^2 = \Gamma_3^2 + \frac{1}{4}(\omega v - \Delta)^2$, $h = i(\omega v - \Delta)$, $\Gamma_3 = l_{nl}^{-1}$

We consider the idler wave to be Gaussian with second order of phase modulation in the temporary domain.

$$A_{30}(t) = A_0 \exp\left[-\left(\frac{1}{2\tau^2} + i\frac{\gamma}{2}\right)t^2\right] \quad (6)$$

By employment the inverse Fourier transformation we obtain spectral density of idler wave in the frequency domain

$$A_3(\omega) = \frac{A_{20}\tau^2}{2\pi} \frac{1}{\sqrt{1+p}} e^{-\frac{\mu^2}{1+p}} \quad (7)$$

where $\mu = \omega\tau$ and $p = \gamma^2\tau^4$ are the frequency and phase modulation parameters respectively. Substitution expression (7) into (5) for the spectral density ($S_1(\omega, z) = A_1(\omega, z) \cdot A_1^*(\omega, z)$) of signal wave yields

$$S_1(\omega, z) = K \frac{e^{-\frac{\mu^2}{1+p}} (\sin\lambda z - \tan\lambda l \cos\lambda z)^2}{(\lambda z)^2 + (hz)^2 \tan^2 \lambda l} \quad (8)$$

where $K = \frac{cn\gamma_1^2 I_{30} I_{20} \tau^2 z^2}{16\pi}$, where $\lambda = l_{nl}^{-1} \left[\frac{1}{4} \left(\frac{l_{nl}}{l_v} \omega v - \frac{\Delta}{\Gamma_3} \right)^2 - 1 \right]^{1/2}$,
 $h = l_{nl}^{-1} \left[i \left(\frac{l_{nl}}{l_v} \omega v - \frac{\Delta}{\Gamma_3} \right) \right]$

From (8) it follows that the shape of a spectrum of a amplified signal wave is determined not only by the values of z , l_{nl} , and l_v but also with their ratios as the z/l_{nl} , and l_{nl}/l_v . In Fig. 1 the dependences of a reduced spectral density $\tilde{S}_1(\omega, z)$ on the parameter $\omega\tau$ are illustrated at different values of l_{nl}/l_v .

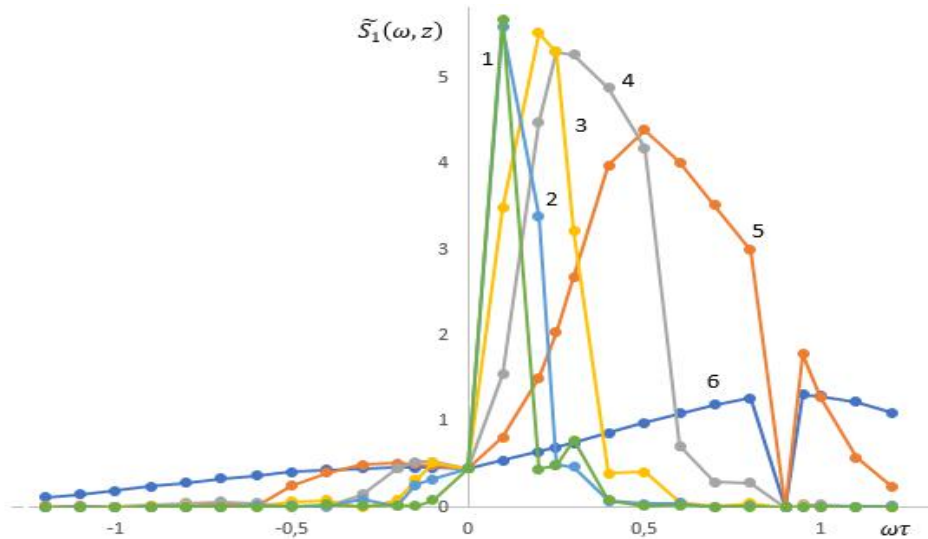


Fig. 1. Dependence of reduced spectral density $\tilde{S}_1(\omega, z) = S_1(\omega, z)/K$ of a signal wave on the parameter $\omega\tau$ for $p = 0$, $z/l_{nl} = 0,5$, $\frac{\Delta l_{nl}}{2} = 1$, $\delta_i = 0$ and various values of l_{nl}/l_v : 1 - $l_{nl}/l_v = 20$; 2 - $l_{nl}/l_v = 15$; 3 - $l_{nl}/l_v = 10$; 4 - $l_{nl}/l_v = 6$; 5 - $l_{nl}/l_v = 3$; 6 - $l_{nl}/l_v = 1$

As can be seen, the shape of a spectrum varies with variation in this ratio. Comparison of plots demonstrates that spectrum of signal wave becomes narrowed and its maxima shift toward smaller values of parameter $\omega\tau$ with increase in the group velocity mismatch. However this behavior is not observed for larger values of l_{nl}/l_v (Fig.1.plots 1 and 2)

Fig.2 illustrates plots of reduced spectral density as a function of parameter $\omega\tau$ for various values of ratio z/l_{nl} .

As can be seen maxima of spectral density decrease with increase in z/l_{nl} . An increase in phase modulation also leads to decrease in the maximum of spectral density (plots 1 and 3).

Dependences of reduced spectral density versus parameter $\omega\tau$ for different values of phase detuning ($\frac{\Delta l_{nl}}{2}$) are presented in Fig.3. It is seen that when there is no phase detuning plot of spectrum becomes symmetric with respect to frequency modulation parameter $\omega\tau$. An increase in phase detuning leads to decrease in the maxima as well as to shift the maxima toward larger values of $\omega\tau$. Also can be seen that increase l_{nl}/l_v leads to increase in the maxima and shift toward smaller values of $\omega\tau$ for the same phase detuning (plots 2 and 3). Positive value of phase detuning parameter promote higher value of spectral density with respect to the same negative value (plots 2 and 5).

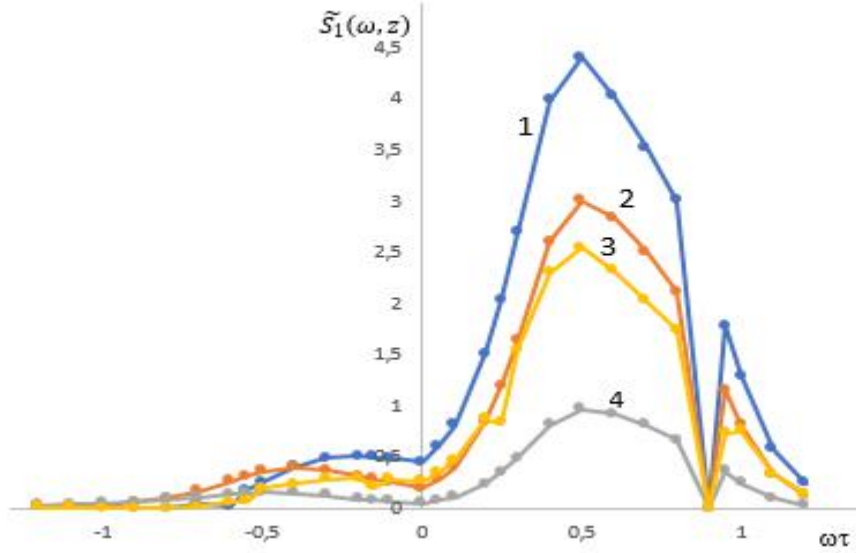


Fig. 2. The reduced spectral density $\tilde{S}_1(\omega, z) = S_1(\omega, z)/K$ of a signal wave as a function of parameter $\omega\tau$ for $p = 0$ (curves 1, 2 and 4), $p = 3$ (curve 3), $l_{nl}/l_v = 3$, $\frac{\Delta l_{nl}}{2} = 1$, $\delta_i = 0$ and various values of z/l_{nl} : $1 - z/l_{nl} = 0,5$; $2 - z/l_{nl} = 1$; $3 - z/l_{nl} = 0,5$; $4 - z/l_{nl} = 1,5$

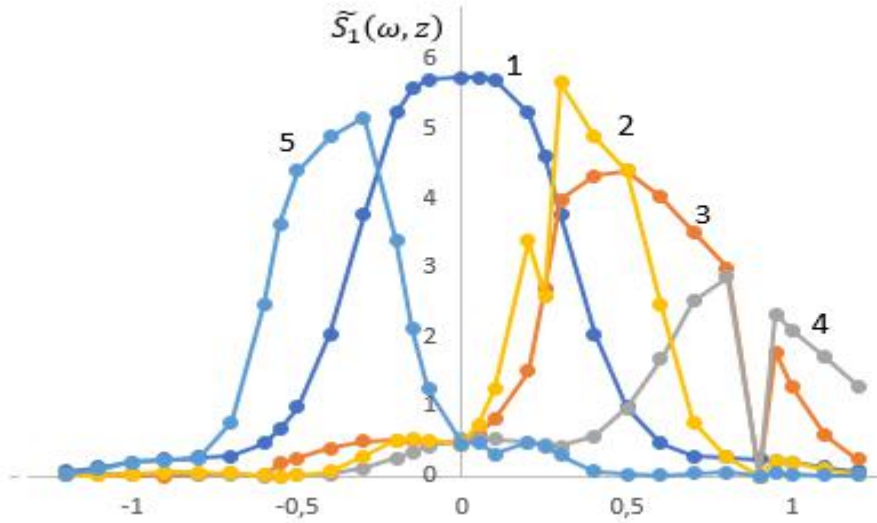


Fig. 3. Dependence of the reduced spectral density $\tilde{S}_1(\omega, z) = \frac{S_1(\omega, z)}{K}$ of a signal wave versus parameter $\omega\tau$ for $p = 0$, $\frac{l_{nl}}{l_v} = 3$ (plots 1, 3, 4), $\frac{l_{nl}}{l_v} = 5$ (plots 2 and 5) $\delta_i = 0$, $z/l_{nl} = 0,5$ and various values of parameter $\frac{\Delta l_{nl}}{2}$: $1 - \frac{\Delta l_{nl}}{2} = 0$; $2 - \frac{\Delta l_{nl}}{2} = 1$; $3 - \frac{\Delta l_{nl}}{2} = 1$; $4 - \frac{\Delta l_{nl}}{2} = 1,5$; $5 - \frac{\Delta l_{nl}}{2} = -1$

3. CONCLUSIONS

From above mentioned one can conclude that parametric amplification of ultra-short pulses in metamaterial in the first order dispersion theory is affected by the group velocity mismatch as well as the phase detuning between interacting waves. We showed that the spectral density of ultra-short pulse wave is affected by the ratios of characteristic lengths. When there is phase matching, the shape of a graph of the spectral density becomes symmetric relatively negative

and positive values of frequency modulation parameter. For the ratios of characteristic lengths l_{nl}/l_v differ from zero maxima of spectral density are obtained not at zero values of frequency but at its different values. Spectrum of signal wave becomes narrowed and its maxima shift toward smaller values of frequency with increase in the group velocity mismatch. This behavior promotes development of generators with narrow frequency band. An increase in phase modulation leads to decrease in the maximum of spectral density. An increase in phase detuning leads to decrease in the

maxima as well as to shift the maxima toward larger values of frequency modulation. An increase in group velocity mismatch leads to increase in the maxima and shift toward smaller values of frequency modulation for

the same phase detuning. Positive value of phase detuning parameter increases spectral density with respect to the same negative value .

-
- [1] *S.A. Akhmanov and R.V. Khokhlov. Eksp. Teor. Fiz.* 43, 351, 1962, [Sov. Phys. JETP 16, 252, 1963].
- [2] *S.A. Akhmanov, V.A. Visloukh, A.S. Chirkin. UFN* 1986 , v. 149, issue 3, p. 449-509.
- [3] *A.I. Maimistov, I.R. Gabitov and E.V. Kazantseva. Opt. Spectrosk.*, 2007, 102, p. 99. [Opt. Spectros. (Eng. Transl.), 102, p.90].
- [4] *S. Zhang et al. Phys. Rev. Lett.*, 2005, 95.
- [5] *W. Cai, V.M. Shalaev. Optical Metamaterials, Fundamentals and Applications* (New York, Springer, 2010).
- [6] *R.J. Kasumova, Z.H. Tagiev, Sh.Sh. Amirov, Sh.A. Shamilova and G.A. Safarova. Journal of Russian Laser Research*, Vol. 38, No. 4, p. 211-218.
- [7] *Z.H. Tagiev, A.S. Chirkin. Sov. Phys. JETP*, 46, 669, 1977. [Zh. Eksp. Teor. Fiz. 73, 1271, 1977].
- [8] *R.J. Kasumova, Sh.Sh. Amirov, Sh.A. Shamilova. Quantum Electronics* 47 (7), 2017, p.655-660.
- [9] *V.V. Slabco, A.K. Popov, C.A. Myslivets, E.V. Rasskazova, V.A. Tkachenko. Kvantovaya Elektronika* 45, 2015, No 12 p.1151-1152.
- [10] *A.K. Popov, V.M. Shalaev. Appl. Phys. B*, 2006, 84 131.
- [11] *M.I. Shalaev, S.A. Myslivets et al. Opt. Lett.*, 36, 2011, 3861.
- [12] *I.V. Shadrirov, A.A. Zharov, Y.S. Kivshar. J. Opt. Soc. Am., B*, 2006, 23, 529.
- [13] *Z.A. Tagiev, Sh.Sh. Amirov. Sov. J. Quantum Electron.* 1989 (11) p.1442-1445.
- [14] *S.A. Akhmanov, V.A. Visloukh, A.S. Chirkin. UFN* 1986 , v. 149, issue 3, p.449-509.
- [15] *Sh.Sh. Amirov, Z.A. Tagiev. Optika i Spektroskopiya* 1990, V.69, issue 3, p.678-683.
- [16] *R.J. Kasumova, Sh.Sh. Amirov, G.A. Safarova. Russian Physics Journal* 2018, N 9, p.10-17.
- [17] *Sh.Sh. Amirov, Z.H. Tagiyev, G.N. Akhmedov. AJP "Fizika"* v. XXIV, 2018, N 4 p.7-10.
- [18] *Sh.Sh. Amirov, R.J. Kasumova, Z.H. Tagiev. Proceedings of International conference "Modern Trends in Physics"* 2019, p.205-210.
- [19] *R.J. Kasumova, Sh.Sh. Amirov. Superlattices and microstructures* Vol.126 (2019), p.49-56.
- [20] *Sh.Sh. Amirov, R.J. Kasumova, Z.H. Tagiev. Proceedings of the VIII International scientific-practical conference "Science and practice: implementation to modern society"*, Manchester, Great Britain December 26-28, 2020, Scientific Collection "Interconf" N 3 (39) 2020, p.1212-1214.
- [21] *Sh.Sh. Amirov. AJP "Fizika"* Vol. XXVII , N 1, 2021, p.8-12.

Received: 01.03.2021

PHOTOLUMINESCENCE PROPERTIES OF ZnIn_2Se_4

I.A. MAMEDOVA

*Institute of Physics NAS Azerbaijan, ave. G.Javid, 131, AZ1143, Baku, Azerbaijan**e-mail: irada_mamedova@yahoo.com*

The photoluminescence properties of ZnIn_2Se_4 were studied at 300K by use of confocal laser microspectrometry. For the first time, edge luminescence with a maximum at 674 nm was observed. Nonlinear intensity dependence of the photoluminescence on the excitation light is found.

Keywords: ZnIn_2Se_4 , edge luminescence, antistructural defects.

PACS: 63.20.dk, 74.25.Kc

INTRODUCTION

Compounds $A^2B^3C^6_4$ ($A - \text{Zn, Cd}$; $B - \text{In, Ga}$; $C - \text{S, Se, Te}$) crystallizing in the space group S^2_4 , attract the attention of researchers in connection with the possibility of their use in semiconductor instrument making. ZnIn_2Se_4 belongs to this defect chalcopyrite family. It also attracts attention of many researchers due to its potential application in various fields such as solar cells [1], memory devices [2], etc.

The photoelectric and optical properties of ZnIn_2Se_4 were studied in [3-8]. From optical measurements, the absorption edge was determined as 1.82 eV for direct transitions and 1.7 eV for indirect transitions [3]. In [5], the optical absorption of Co doped and undoped ZnIn_2Se_4 single crystals were studied. The bandgap values of undoped samples determined from the spectra were 1.774 eV for direct and 1.662 eV for indirect transitions at 300 K, and for doped samples, these values were determined as 1.413 eV and 1.277 eV, respectively. Photosensitive properties were studied in [4]. Photosensitive structures based on In / n- ZnIn_2Se_4 have been obtained. In this work, the bandgaps of n- ZnIn_2Se_4 for direct and indirect transitions were determined as $E_{\text{dir}} = 2.1$ eV and $E_{\text{ind}} = 1.62$ eV, respectively. The photoelectric memory effect was discovered in [2], where this effect is explained by the authors by the presence of double-charged acceptor levels and makes it possible for practical application as electro-optical memory devices. The authors assume that ZnIn_2Se_4 is a direct-gap semiconductor with a band gap of 1.9 eV. The optical properties of ZnIn_2Se_4 films were studied in [9]. The band gap for direct allowed optical transitions is determined as 2.065 eV and for indirect transitions as 1.69 eV. The calculated value of the band gap is 1.85 eV (DC) and 1.72 eV (DF) for ZnIn_2Se_4 [10], for the ZnIn_2Se_4 film from optical absorption spectra, the band gap is determined as 2.21 eV [11].

Very little is known at present about the luminescence of ZnIn_2Se_4 . To our knowledge, the luminescence properties were studied only in [12, 13] in the temperature range 55-200 K. The authors attributed the broad luminescence band at 1.28 eV to the energy levels formed by complexes I and V_{Zn} or antisite defects of the A_B, B_A type.

We have previously investigated the radiative properties and energy levels in the band gap of ZnIn_2Se_4 in a wide temperature range of 10–300K [14]. The optical transmission of ZnIn_2Se_4 have been studied by us in [15]. The optical band gap at 293 K is defined as 1.72 eV. The transmission spectrum is also characterized by the presence of an absorption band at 850 nm.

In this work, in order to obtain additional information about the luminescence properties of ZnIn_2Se_4 , we investigated photoluminescence at 300K using a confocal laser microspectrometer.

EXPERIMENTAL TECHNIQUES

ZnIn_2Se_4 crystals were synthesized by direct fusion of the initial highly pure components Zn, In, and Se in a stoichiometric quantities in graphitized quartz ampoules silica tubes in a vacuum of about 10^{-4} mm Hg. pillar. X-ray diffraction measurements were carried out on a Bruker D8 device. X-ray analysis of the powder showed that ZnIn_2Se_4 crystallizes in a tetragonal structure with the space group S^2_4 and with lattice parameters $a = 5.709$ Å, $c = 11.449$ Å, $\delta = 1 - c / 2a \approx -0.0027$. As can be seen, in contrast to [16, 17], a slight tetragonal stretching of the lattice was found, which is rarely found in crystals of ternary compounds with tetrahedral coordination of atoms and structures such as chalcopyrite and thiogallate. Such a stretching of the ZnIn_2Se_4 lattice was also found in [4, 11, 18]. Figure 1 shows the X-ray diffraction pattern of ZnIn_2Se_4 .

The photoluminescence spectra were recorded on a Nanofinder30 confocal laser microspectrometer (Tokyo Instr., Japan). Nd: YAG laser with the wavelength of $\lambda_{\text{ex}} = 532$ nm and a maximum power of 10 mW was used as an excitation source. The radiation detector was CCD camera (1024 x 128 pixels), cooled by thermoelectric method to -100°C , operating in the photon counting mode. The experiments were carried out at room temperature.

DISCUSSION OF THE RESULTS

Fig. 2 shows the spectrum of Raman scattering of light in ZnIn_2Se_4 . The spectrum consists of eight lines at 68, 87, 100, 133, 168, 193, 204, 240 cm^{-1} . These values of the frequencies of vibrational modes

PHOTOLUMINESCENCE PROPERTIES OF ZnIn₂Se₄

coincide with the frequencies determined from the spectra of IR reflection and Raman scattering of light

from [19-21]. For comparison, Table 1 presents the values of the frequencies of the vibrational modes.

Table 1.

Frequency values (in cm⁻¹) of vibrational modes of ZnIn₂Se₄

Mode symmetry	This work	[19]		[20]	[21]
	ω_R	ω_R	ω_{IR}	ω_{IR}	ω_R
E	68	-	67/68	68	67
E	87	86	85/85	87	86
B ₂	100	100	101/104	102	99
A ₁	133	135	-	-	132
E	168	165	164/165	-	167
E, B ₂	193	-	196/203	-	193/199
E, B ₂	204	204	-	202	-
E, B ₂	240	242	213/242	221	212/242

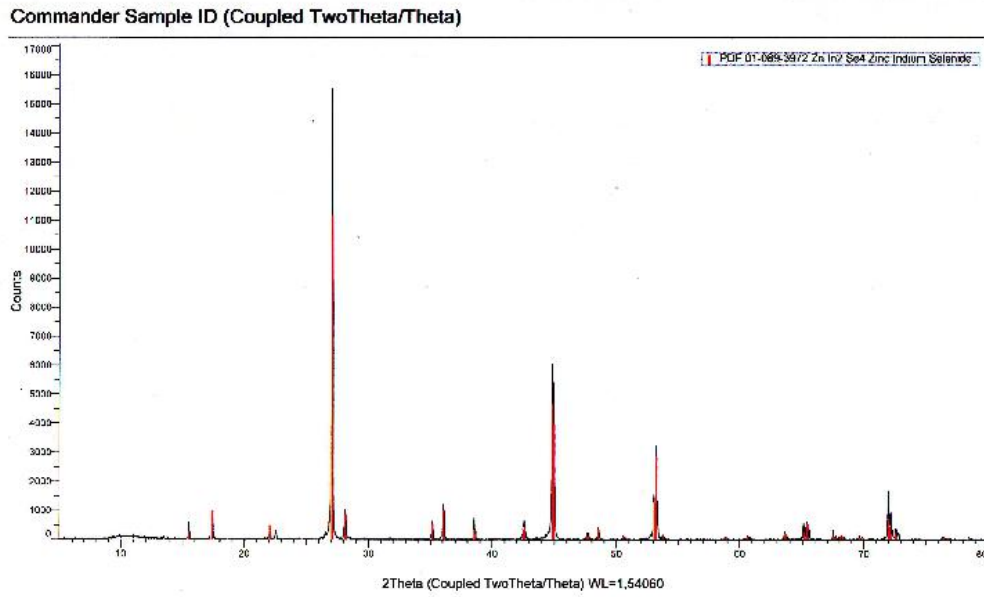


Fig. 1. X-ray diffraction pattern of ZnIn₂Se₄

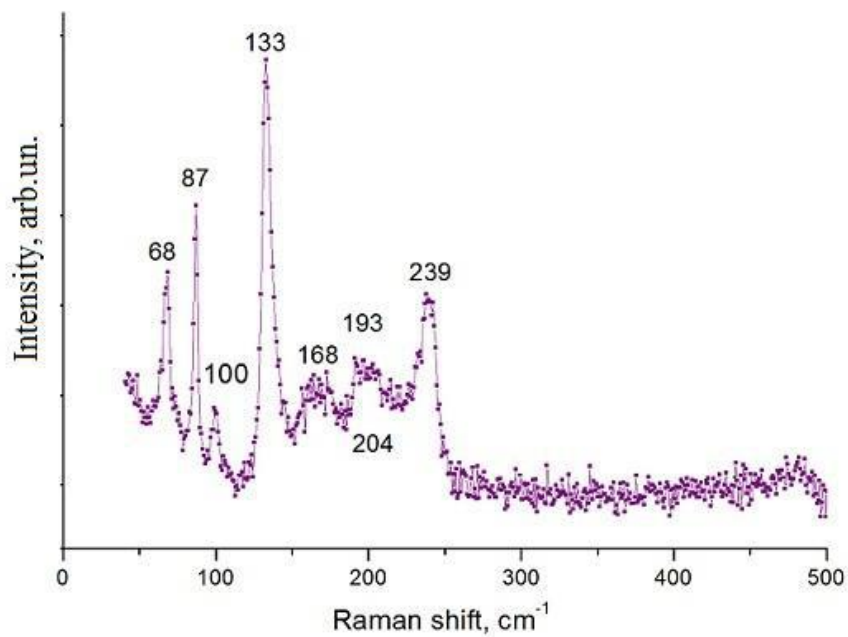


Fig. 2. Raman spectrum of ZnIn₂Se₄

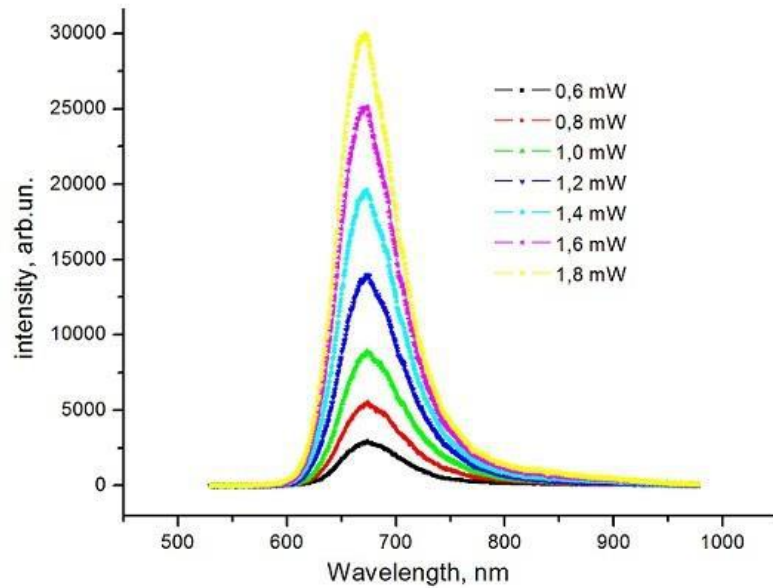


Fig. 3. Photoluminescence spectrum of ZnIn₂Se₄

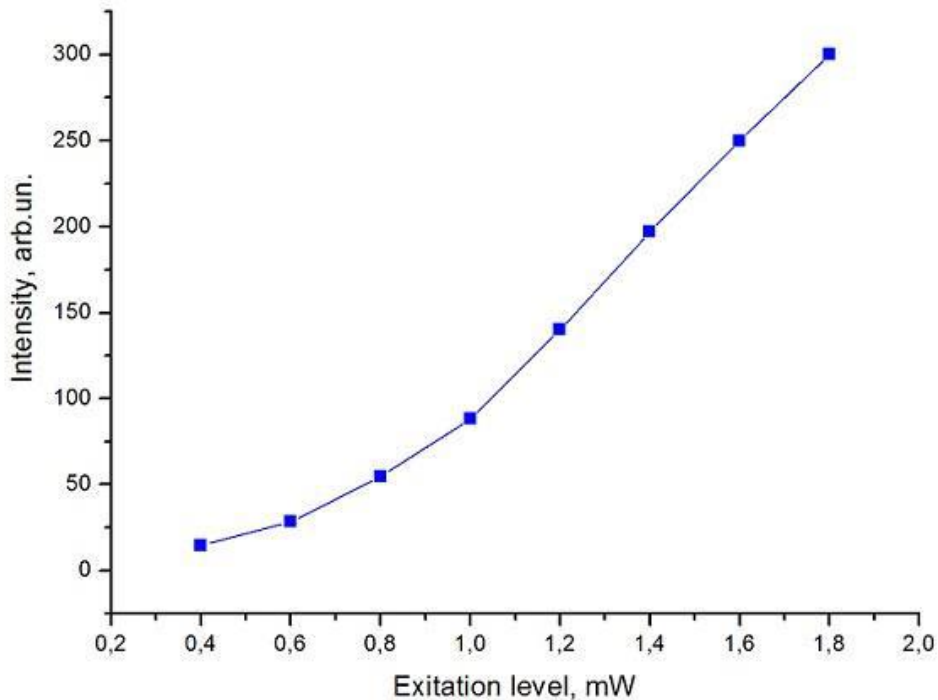


Fig. 4. Dependence of the photoluminescence intensity on the intensity of the exciting light in ZnIn₂Se₄

Figure 3 shows the photoluminescence spectra at different intensities of the exciting light. As can be seen from the figure, the spectrum consists of a band at 674 nm (~ 1.84 eV) with a half-width of ~ 60 nm, the half-width and position of which does not change with the intensity of the exciting light. A sharp rise of the band from the short-wavelength region and the position of the maximum suggest that this is edge luminescence. The stretched shape of the long-wavelength part of the spectrum indicates the presence of an impurity band in ZnIn₂Se₄ in the 850-900 nm region. The band at 850-900 nm is associated with impurity levels caused by antisite defects, which are characteristic for crystals of the A²B₂C₄⁶ class [22].

The temperature dependence of this impurity luminescence band was investigated by us in [14]. This emission band, in terms of the position of the maximum, slightly differs from the broad luminescence band observed in [12, 13] at 1.28 eV. In [12], the dependence of the intensity of this emission band on the excitation level was also investigated, and it was revealed that the dependence is characterized by superlinearity; $I_{PL} \sim I_{ex}^{1.4}$, at high temperatures (200K), and at low temperatures (90K), this dependence turned out to be linear ($I_{PL} \sim I_{ex}^{1.05}$).

Figure 4 shows the dependence of the photoluminescence intensity on the intensity of the exciting light. As can be seen from the figure, the

dependence has a nonlinear character $I_{PL} \sim I_{ex}^2$. It can be assumed that the emission band is associated with an interband radiative transition.

CONCLUSION

By using confocal laser microspectrometer, edge luminescence in ZnIn₂Se₄ with the maximum at 674 nm (1.84 eV) at 300 K has been detected for the first time. A quadratic character of the dependence of the luminescence intensity on the intensity of the exciting

light has been established. This study of the emission properties shows that ZnIn₂Se₄ is promising material for use in optoelectronics.

ACKNOWLEDGMENT

This work was supported by the Science Development Foundation under the President of the Republic of Azerbaijan – Grant № EIF-BGM-3-BRFTF-2+/2017-15/02/1

-
- [1] *F.J. Garcia and M.S. Tomar.* n-CdS/p- ZnIn₂Se₄ thin film solar cell. *Thin Solid Films*, 1980 v. 69, 137-139.
- [2] *J. Filipowicz, N. Romeo and L. Tarricone.* Photoelectrical memory effect in ZnIn₂Se₄. *Solid State Communications* 1980, v. 38, 619-623.
- [3] *J.A. Beun, R. Nitsche and M. Lichtensteiger.* Optical and electrical properties of ternary chalcogenides. *Physica*, 1961, v. 27, 448-456.
- [4] *A.A. Vaipolin, Yu.A. Nikolaev, V.Yu. Rud, Yu.V. Rud, E.I. Terukov.* Photosensitive structures on ZnIn₂Se₄ single crystals. *Fizika i texnika poluprovodnikov*, 2003, v.33, N4, 432-434.
- [5] *Sung-Hyu Choe.* Optical energy gaps of undoped and Co-doped ZnIn₂Se₄ single crystals, *Elsevier, Current Applied Physics*, 2009, v.9, 1–3.
- [6] *E. Fortin and F. Raga.* Low temperature photoconductivity of ZnIn₂Se₄ and CdIn₂Se₄, *Solid State Communication*, 1974, v.14, 847-850.
- [7] *P. Manca, F. Raga, and A. Spiga.* Photoconductivity of ZnIn₂Se₄ and ZnIn₂Te₄, *Short notes, phys. stat. sol. (a)*, 1973 v.16, K105.
- [8] *P. Manca, F. Raga, and A. Spiga.* Trap distribution and photoconductivity in ZnIn₂Se₄ and ZnIn₂Te₄, *Nuovo Cimento*, 1974, V.19 B, N1, 15-28.
- [9] *M.M. El-Nahass, A. Gusti, B. Dakhel and H.S. Soliman.* Growth and optical properties of ZnIn₂Se₄ films, *Optica Pura Y Aplicada*, 1991, V.24, 117-125.
- [10] *S. Reguieg, R. Baghdad, A. Abdiche, M.A. Bezzerrouk, B. Benyoucef, R. Khenata, and S. Bin-Omran.* First-Principles Study of Structural, Optical, and Thermodynamic Properties of ZnIn₂X₄ (X = Se, Te) compounds with DC or DF Structure. *Journal of Electronic materials*, DOI: 10.1007/s11664-016-4831-8_2016. The Minerals, Metals & Materials Society.
- [11] *M.M. El-Nahass, A.A. Attia, G.F. Salem, H.A.M.Ali, M.I. Ismail.* Effect of vacuum annealing and substrate temperature on structural and optical properties of ZnIn₂Se₄ thin films, *Physica B*, 2013, 425, 23–30.
- [12] *E. Grilli, M. Guzzi, and R. Molteni,* Luminescence of ZnIn₂Se₄ crystals. *Phys. stat. sol. (a)*, 1976, 37, 399-406.
- [13] *M. Guzzi and E. Grilli.* Localized levels and luminescence of AB₂X₄ semiconducting compounds, *Materials Chemistry and Physics*, 1984, v.11, 295-304.
- [14] *H. Hahn, G. Frank, W. Klinger.* *Z. Anorg. Allgem. Chem.*, 1955, v.279, 241.
- [15] *R. Trykozko, J. Filipowicz.* *Japan. J. Appl. Phys. (Suppl. 19-3)*, 1980, v. 19, p.153-156.
- [16] *T.G. Kerimova, I.A. Mamedova, Z. Kadiroglu, N.A. Abdullayev, M. Feldman.* Temperature dependence of photoluminescence of ZnIn₂Se₄, *AJP_Fizika (MTCMP-2018, Baku) 2018, v.XXIV, N2, 33-36.*
- [17] *T.G. Kerimova, S.G. Asadullayeva, A.G. Sultanova, I.A. Mamedova.* *AJF, Fizika*, 2007, v. XIII, 4, 126-127.
- [18] *H.P. Trah and V. Kramer.* Crystal structure of zinc indium selenide, ZnIn₂Se₄ *Z. Kristallogr.*, 1985, 173, 199.
- [19] *V. Riede, H. Neumann, H. Schwerv, V. Kramer, I. Gregora, V. Vorlicek.* Infrared and Raman Spectra of ZnIn₂Se₄, *Cryst. Res. Technol*, 1993, v.28, N5, 641 – 645.
- [20] *H. Haeusele.* FIR und Ramanspektren von ternären Chalkogeniden des Galliums und Indiums mit Zink, Cadmium und Quecksilber, *Journal of Solid State Chemistry*, 1978, v.26, 367-376.
- [21] *G. Attolini, S. Bini, P. P. Lottici, C. Razzetti.* Effects of Group III Cation Substitution in the Raman Spectra of Some Defective Chalcopyrites, *Cryst. Res. Technol.* 1992, v.27, N5, 685-690.
- [22] *A.N. Georgobiani, S.I. Radautsan, I.M. Tiginyanu.* Wide-Gap II-III₂-VI₄ semiconductors: optical and photoelectric properties and potential applications, *Fizika i texnika poluprovodnikov*, 1985, v.19, 193-212.

Received: 30.03.2021

FREE STANDING AAO NANOPOROUS MEMBRANES FOR LIQUID FILTRATION

Sh.O. EMINOV, A.Kh. KARIMOVA, E.A. IBRAHIMOVA, J.A. GULIYEV

*Institute of Physics NAS Azerbaijan, H.Javid ave., 131 Baku, Azerbaijan**e-mail: ayselkerimova00@mail.ru*

The method for creation of membranes of alumina (AAO) films for water filtration by anodization of aluminum foils in oxalic acid was described. The obtained foils were characterized by SEM and optical microscopes. The permeability measurements of the membranes have shown that the membranes are suitable for precision separation of liquid and gaseous mixtures in laboratory conditions.

Keywords: Membranes, anodic oxidized aluminum, AAO, liquid filtration.

PACS: 61.46.Km

INTRODUCTION

Quasi-one dimensional nanostructures such as nanowires and nanotubes have attracted the attention from researchers due to their properties of the two dimensions being in the nanoscale and one dimension being in the microscale. Fabrication of ordered arrays of nanostructures is required in catalysis, sensing, electronics, energy harvesting and storage, and applications of materials with tailored magnetic and optical properties.

Membrane methods for the separation of liquid and gaseous mixtures refer to low-cost environmentally friendly technologies for the separation of substances and the treatment of various wastes. Owing their effectiveness in removing contaminants with sizes less than 1 μm nanoporous filtering membranes have been used for drinking water purification. Another quite important task in terms of the practical application of membranes is separation of organic macromolecules and proteins for hemodialysis and hemofiltration in biomedicine.

One of the promising materials for creating nanoscale membranes is nanoporous anodic aluminum oxide (AAO, alumina) [1-3]. This material has a precise, self-assembled honeycomb structure composed of parallel nanopores with no lateral crossovers between individual pores. AAO can be easily fabricated by simple anodization of aluminum in an acidic electrolyte. Different anodization regimes can be applied in the fabrication process, leading to different pore diameters in the range of 10-450 nm. AAO is a very suitable template for immobilization of the biological molecules, due to the adjustable pore size and interpore distance. Furthermore, nanoporous AAO is optically transparent, electrically insulating, chemically stable, bioinert, and biocompatible. These outstanding properties are beneficial for various applications of AAO membranes in biotechnology and medicine ranging from biofiltration membranes, lipid bilayer support structures biosensing devices, and implant coatings to drug delivery systems with AAO capsules and scaffolds for tissue engineering. Furthermore, AAO also serve as widely used template for other biocompatible nanostructures such as gold and platinum nanopillars. For that reason over the past years, the development of novel biomedical

applications has benefited immensely from the unique properties of AAO membranes. Despite the proven utility of those nanofabrication methods, there is still a lack for simpler and cheaper procedures to expand the usage of this nanotemplate.

High-quality AAO (anodic aluminum oxide) films provide ordered straight channels, with a diameter of 10–500 nm, pore density of 10^7 – 10^{11} pore/cm², and thickness of 1–300 μm [1,2]. With large surface areas, high mechanical strength, and flexibility, AAO can be used in medical or energy applications, such as drug delivery and detection [3,4]. The large AAO surfaces can be utilized to absorb the bio-indicators or drugs, and the releasing behavior can also be controlled based on the heat sensitivity. AAO has also found applications in energy conversion between carbon dioxide (CO₂) and methanol (CH₄) [5,6]. By loading photocatalyst particles on the AAO surface, such photocatalytic systems can be used to recycle carbon dioxide into organic compounds. Based on the features of larger surface areas and nanochannels for mass delivery and gas diffusion, three-dimensional (3D) structure of AAO films have practical advantages over two-dimensional (2D) AAO films for medical and energy applications. AAO has a lower melting point than pure alumina because of the inclusions in the porous AAO structure. Spooner [7] presented the following compositions of alumina film anodized using sulfuric acid as electrolyte: Al₂O₃ (78.9 wt. %), Al₂O₃·H₂O (0.5 wt. %), Al₂(SO₄)₃, and H₂O (0.4 wt.%). According to Akahori's work [8], the melting point of AAO is near 1200 °C, and AAO template retains stable, at around 1000 °C [9], which is lower than that of bulk alumina (2017 °C for Al₂O₃(γ)). The AAO structure maintaining temperature of 1000 °C is stable enough to be a template for CaO-CaCO₃ reaction at 894 °C. In the past, tubular AAO has attracted attention. Several methods were proposed for the fabrication and applications of tubular AAO films. According to Altuntas's report [10], the large area (50 cm²) free-standing AAO membranes was obtained by sputtering carbon onto AAO surface for conductive AAO biosensor applications, especially tubular AAO for filtering. Belwalkar [11] showed that AAO tubular membranes were fabricated from aluminum alloy tubes in sulfuric and oxalic acid electrolytes, the pore sizes were ranging from 14 to 24 nm, and the wall

thicknesses was as high as 76 μm , which increased the mechanical strengths for handing. The pore density can be calculated by determining the number of pores according to the area fraction: $P = A_p / [(\pi/4) D^2]$, where P is the number of pores, A_p is the area fraction of pores, and D is the average pore diameter. Gong [12] presented that AAO membrane was prepared in 0.2 M oxalic acid electrolyte under 25 to 40 V applied for 11 to 18 h; additionally, the control in drug delivery by using nanoporous alumina tube capsules with pores of

25 to 55 nm was demonstrated. Kasi1 [13] further reported that the purity of Al is also a matter of great concern for AAO fabrication. Some applications, such as nano-templates for semiconductor industry, require a regular pore arrangement with a honeycomb structure, which cannot be achieved from low grade Al. Moreover, AAO membrane in tubular form can further satisfy the demand in both diffusive and convective filtration of hemodialysis.

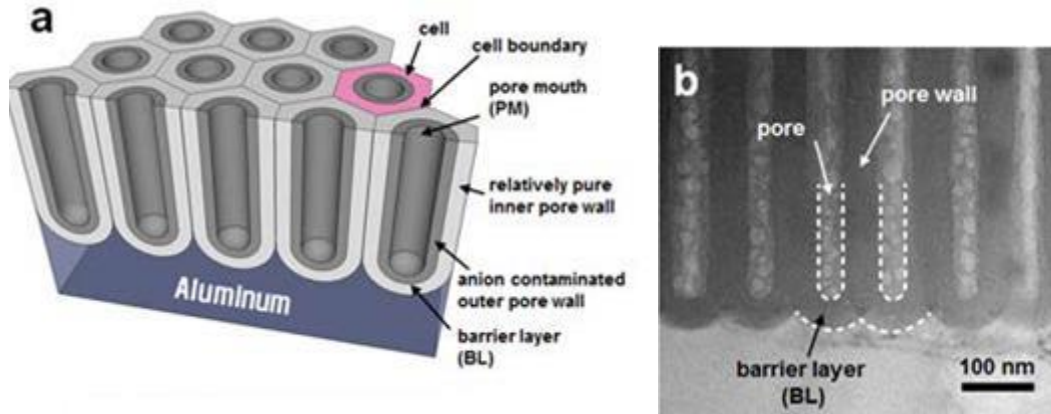


Fig. 1. (a) Schematic showing an idealized structure of porous anodic aluminum oxide (AAO) with a self-organized array of hexagon cells and convex-shaped geometry of barrier layer (BL) at the base of pores. The two different regions of anion contaminated (dark gray) and relatively pure oxide (light gray) are also presented. (b) Cross-section TEM image of bottom part of porous AAO.

1. EXPERIMENT TECHNIQUE

In this work, we present the development and optimization of low cost AAO membranes by galvanostatic anodization of commercial Al foils (99.5% purity), and their application as membrane filters in the UF process of drinking water.

The stages of AAO processing are shown in the Fig.1. Pure aluminum (99.95%) foil with a thickness of 100 μm was used as a starting substrate for anodization. In order to promote long-range ordering in aluminum by limiting the number grain boundaries the foil was annealed at 500 $^{\circ}\text{C}$ in air for 3 hours. Then the annealed foil was cut into approximately 3.0 cm by 3.0 cm rectangles and ultrasonically degreased in acetone and ethanol for 5 minutes on an each. The native oxide layer of the Al foil was removed in 1 M NaOH solution and rinsed in distilled water (Stage A).

The anodization was carried out in a home made two-electrode cell using ice-bath for keeping temperature of solution in the range of 0-5 $^{\circ}\text{C}$ during anodization. Before anodization the area of the foil intended for the membrane has been delaminated (Stage B). Then the foil (anode) was mounted to an electrolytic cell via an O-ring and on copper plate which was connected to the power supply by a conducting wire. (Stage C). The plate was continuously cooled by means of ice water bath. The counter electrode (cathode) was a piece of platinum (Pt) sheet. The distance between the two electrodes was approximately 2 cm.

The AAO were prepared by two-step anodization experiments. The defective microstructure of the Al

metal surface prior to anodization affects the ordering of the subsequent oxide film. For that reason in accordance with the ‘‘Masuda method’’; the first oxide film (called the sacrificial layer) is selectively dissolved. As proposed in the literature this step removes the non-ordered pores and lets a dimple array to the second anodization stage. Thus second oxidated film has a much more regular structure due to the pre-patterning of the substrate by the first anodization.

The first anodization step was carried out for 1 h under galvanostatic conditions ($U = 40 \text{ V}$, $T = 5^{\circ}\text{C}$) in 4% water solution of oxalic acid ($\text{C}_2\text{H}_2\text{O}_4$). During this operation, the layer with non-ordered pores structure was created. Then this layer was completely stripped away from the Al substrate by dissolution i.e. wet chemical etching in a solution containing 6 wt% phosphoric acid and 1.8 wt% chromic acid ($\text{H}_2\text{Cr}_2\text{O}_7$) at 60 $^{\circ}\text{C}$ for 1h under stirring (Stage D).

The second anodization step (Stage E) was carried out under condition similar with the Stage C for 3h. After this step the aluminum back side of the electrode was chemically etched in 0.1 M solution of CuCl_2 in 20% HCl to reveal the AAO barrier oxide layer (Stage G). To provide stable mechanical support to the AAO membrane, was performed in a reduced area compared with the anodized side of the Al foil (stage E). The barrier layer was removed in 5% H_3PO_4 water solution at temperature 45-50 $^{\circ}\text{C}$ during 15 min over the barrier layer, which was then rinsed with deionized water, and then dried with Nitrogen gun under ambient conditions (stage H).

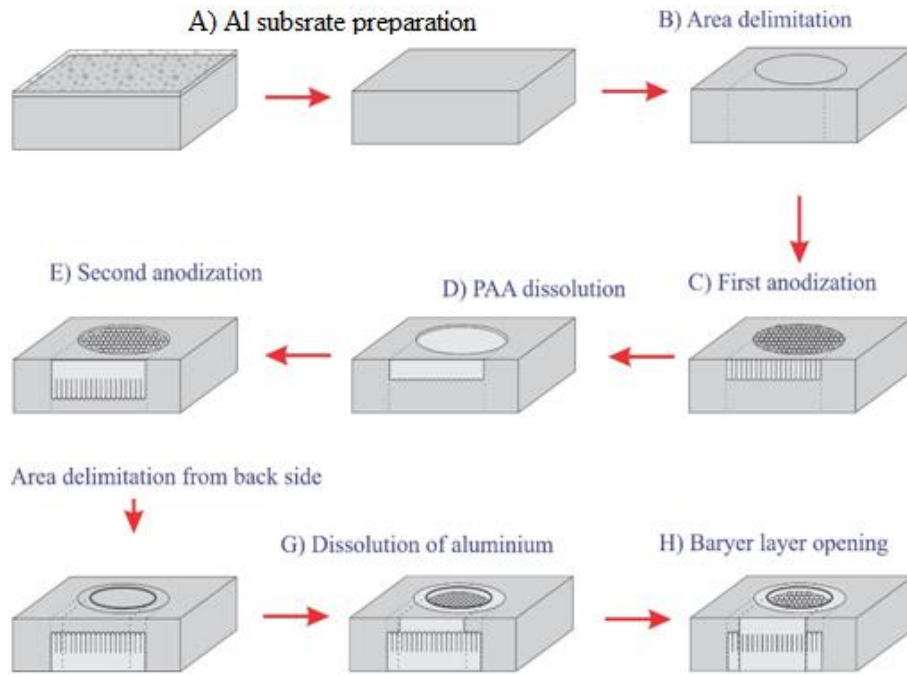


Fig. 2. The stages of AAO processing a) Preparation of the foil, irregular AAO film after 1st anodisation, stage C; b) simple array on Al surface stage D; c) homogeneous porous film after 2nd step anodization, Stage G;

2. RESULTS AND THEIR DISCUSSION

The optical photographs of the AAO film taken by microscope MBS-22 (x 54) after first anodisation is shown in Fig.2.



Fig. 3. View of the AAO film under optical microscope MBS-22 (x 54), photographs after first anodization.

SEM images of AAO (Fig.4) confirmed the creation of an array of highly ordered hexagonal cell structures with pores about 40-60 nm in diameter.

EDAX Spectrum of obtained film shown on figure 5. In this figure shows major elements such as Al and O is a main part of film. Ni sputtered on the sample

used as a contact for measure of film and minor elements such as P and Si which were due to contamination.

Digital photographs of the membrane taken before and after removing barrier layer are showing correspondently on left and right sides of the figure 6. To guarantee the mechanical stability, as well as to inhibit solution leakage during the filtration, metallic aluminum on our membrane was maintained at the edge of AAO samples. The partially transparent region at the center of the image corresponds to the PAA membrane itself and the white ring is the supported membrane on the Al base.

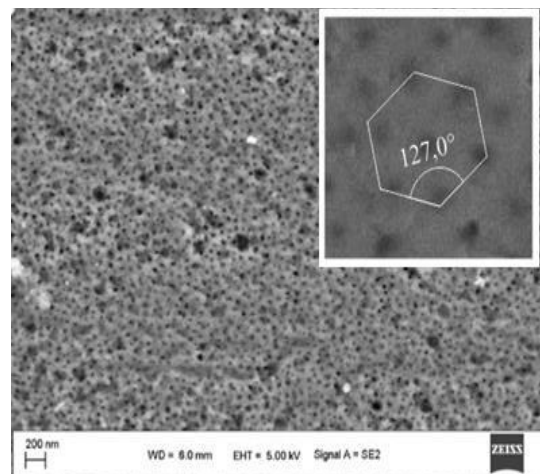


Fig. 4. The SEM image of the AAO film (left) and its an enlarged fragment (right).

FREE STANDING AAO NANOPOROUS MEMBRANES FOR LIQUID FILTRATION

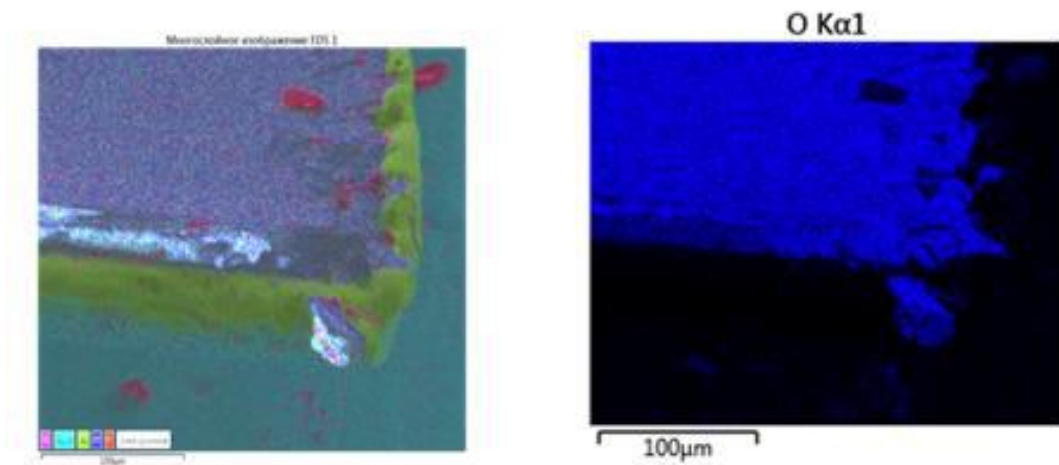
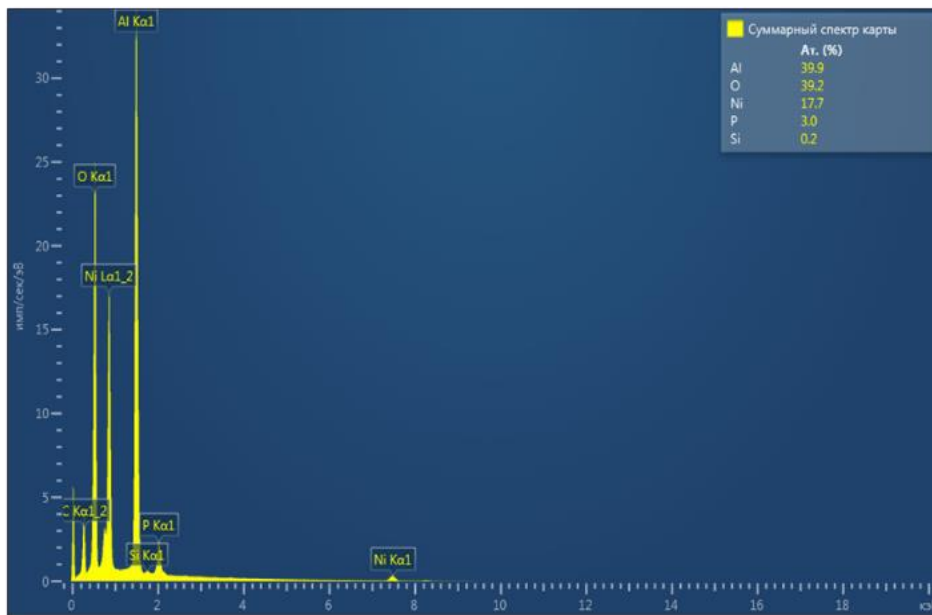


Fig. 5. EDAX spectrum and elemental maps of film.

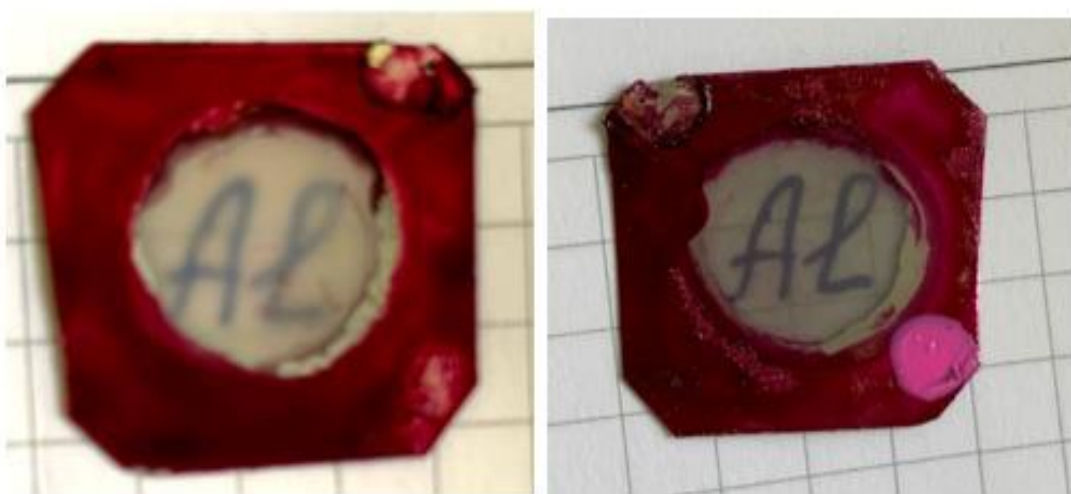


Fig. 6. Digital photographs of the membrane before (left) and after (right) removing barrier.



Fig.7. Device for liquid permeance measurements.

The liquid permeance measurements membranes were performed using a home made device based on a large medical plastic syringe at a temperature of 25 ± 2 °C. The device used for these studies is shown in the Figure 7.

The permeability was calculated from the pressure difference measured by pressure transducers and the mass of accumulated permeate. These studies have shown that the membranes are suitable for precision water purification in laboratory conditions.

-
- [1] *M. Galizia, W.S. Chi, Z.P. Smith, T.Ce. Merkel et al.* 50th Anniversary perspective: Polymers and mixed matrix membranes for gas and vapor separation: A review and prospective opportunities. *Macromolecules*, 2017, 50, 7809–7843.
- [2] *Dmitrii I. Petukhov, Dmitrii A. Buldakov, Alexey A. Tishkin, Alexey V. Lukashin and Andrei A. Eliseev.* Liquid permeation and chemical stability of anodic alumina membranes Beilstein J. Nanotechnol. 2017, 8, 561–570.
- [3] *Alexsandro Mendes Zimer, Maria Manuela P. Machado1 et al.* Optimized porous anodic alumina membranes for water ultrafiltration of pathogenic bacteria (E. coli) *Journal of Nanoscience and Nanotechnology* Vol. 15, 1–9, 2015.

Received: 12.04.2021

THE HUMAN PERCEPTION AND UNCERTAINTY IN QUANTUM PHYSICS

E.A. ISSAEVA

*Institute of Physics of National Academy of Sciences of Azerbaijan,
131, H. Javid ave., Baku, AZ1143, e-mail: elmira@physics.ab.az, el_max63@yahoo.com*

The uncertainty of world is being considered by human perception point of view. So the knowledge is shared on usual, unusual, transcendent and transcendental. It depends on what kind of world (macro or micro) and in which position the observer exists (in or out system), i.e. system is open or closed. For the analysis of this problem the “Schrödinger cat” experiment has been considered.

Keywords: Entanglement, decoherence, open and close system, “Schrödinger cat” experiment, consciousness of observer.
PACS: 03.65.-w

1. INTRODUCTION

Objects are the sources of the information and it is clear that the quantity of the information depends on number of objects perceived by man. The macrocosm is perceived directly, and a microcosm through the device. However, through the device it will be very smaller number of objects and consequently the information will be much less. Therefore, the perception of an invisible microcosm is not complete. Perhaps, real reason of Heisenberg Uncertainties is in it.

Let's N_k and N_q are the numbers of perceived objects in a macrocosm (the classical world) and a microcosm (the quantum world), accordingly. It is clear that uncertainty is inversely to the number of perceived objects, and we can enter unit of uncertainty

that will be $\Delta\alpha_k = \frac{A}{N_k}$ and $\Delta\alpha_q = \frac{A}{N_q}$ in a macro

and microcosms, respectively, where A is a constant connected with human ability of perception. Due to $N_k \gg N_q$, a microcosm is more uncertain than a macrocosm. We assume that N_k and N_q are constant.

Making observation (aim-directed perception), we perceive not all objects but only those that have been selected. Let's mark them n_k and n_q . It is clear that total uncertainty α is proportional to the number of objects which stay out of our perception, i.e. $(N_k - n_k)$ and $(N_q - n_q)$, respectively. Therefore

$$\alpha_k = (N_k - n_k)\Delta\alpha_k = (N_k - n_k)\frac{A}{N_k} \quad \text{and}$$

$$\alpha_q = (N_q - n_q)\Delta\alpha_q = (N_q - n_q)\frac{A}{N_q} \quad \text{in macro}$$

and microcosms, respectively.

Let's consider a case, when in both worlds the uncertainty is the same, i.e. $\alpha_k = \alpha_q$. In the only measuring process this case can take place because there is no border between macro- and micro worlds and a man acts in “macrocosm + microcosm” system. His consciousness can be either included (closed system) or not included into this system (open system). When the system is opened, the microcosm's uncertainty is decreased and becomes equal to the

uncertainty of a macrocosm. When system is closed the closed system, on the contrary, the uncertainty of a macrocosm is increasing and becomes equal to uncertainty of a microcosm. So, from $\alpha_k = \alpha_q$, we

obtain $n_q = \frac{N_q}{N_k}n_k$. One can see that the increasing

of number of observed objects in micro world lead to the increasing of this that in macrocosm. It means that the some other macroscopic device, becoming already observed objects, can give us additional information about quantum world. Let's try to see this correlation in the well known Einstein - Podolsky – Rosen (EPR) paradox [1]. In this paradox, two particles that interact with each other sometime are considered. They appear in entangled, or it is better to tell in connected because by the measurement of an impulse of only one of particles it is possible to predict an impulse of other particle. But it means the number of the observed objects in quantum world is increasing. Without doing special supervision or measurement, we nevertheless receive the additional information. Bohr has explained this paradox by a certain configuration of devices [2]. Namely the configuration of devices gives increasing the number of observed in macro world (this is that device becoming observed object) in a result of which we receive the additional information about a microcosm. As Bohr writes that in each experimental installation it is necessary to establish the border between those parts of physical system that we consider as measuring devices and as objects of researching. It depends from us. Bohr himself chooses this border such way as he writes: «the choice of a place for this border is possible only within that area where the quantum-mechanical description of the given process in essence is equivalent to the classical description». So Bohr can avoid this paradox. Thus, in quantum physics all depends on the choice of border. The choice of this border will be made by the observer who should not be included in the “macrocosm + microcosm” system. Such system is opened. But what will occur, if the observer will be included in this system? In this case the “macrocosm + microcosm + observer's consciousness” system, which is already closed, takes place. It is clear that already nobody will be busy by the choice of the border and consequently the question

about border loses meaning.

Thus, at a certain configuration of devices, the abovementioned observer not included in system could receive the additional information about microcosm; therefore the uncertainty of the quantum world was decreased. In this case, the microcosm becomes such uncertain (i.e. less), as a macrocosm. But if the observer will be included in system then all will be another. For such observer the macrocosm becomes such uncertain (i.e. more), as a microcosm. In two cases $\alpha_k = \alpha_q$. They differ from each other by the decreasing α in first case (opened system) and the increasing α in second case (closed system). Thus, both Einstein and Bohr are right. They both say about the measurement ($\alpha_k = \alpha_q$), but different cases are considered by them. Bohr sees in EPR paradox the decreasing uncertainty, which allow us to describe the microcosm by classical method, by theory of probabilities. But Einstein, opposite, sees in EPR paradox the increasing uncertainty and therefore, he say about the latent parameters of sub quantum world. For the deep understanding of all aforesaid the idea of «Schrödinger cat» can be very useful [3]. In this experiment the unusual state of atom, simultaneously being decayed and not being decayed, becomes connected not with atom, as in EPR paradox, but with macroscopic object, a cat in the invisible camera. There is an interaction of these two objects from the different worlds (atom - micro, cat - macro). As result, the paradox – entanglement or joining states of atom and cat with each other takes place. The logic of quantum physics demands us to think that cat is simultaneously both alive and dead. In open system this paradox is resolved by opening camera by observer. He sees that, for example, the cat is alive. This phenomenon is the decoherence. When the camera is closed Bohr's border can pass only in front of the camera. There is no information about states of both cat and atom. But in the case when the camera is being opened this border can already pass inside the camera been occupying the cat. We receive the information about state of the cat (alive or dead). According to its state (cat becomes the device for us) we get information about state of the atom (decay or not decay). Let's note for this atom we don't make additional measurement. Someone can say us that this is different things - two atoms in EPR paradox and atom and cat in Shrodinger's paradox. Hypothetically, it is possible another scenario too. The camera is being opened and the Bohr's border is already occupied atom instead of cat. Atom becomes as device for us and we get information about cat. The atom becomes here as object of macrocosm but cat, as atom in EPR paradox, become object of microcosm. In any case, if camera is being opened the uncertainty of microcosm is decreasing and can becomes equal to the uncertainty of macrocosm, i.e. $\alpha_k = \alpha_q$. Then we can by state our macroscopic cat-device we can judge about atom. In fact, in only this case Bohr was right to use the classical knowledge. All these - opening the camera, looking on it and choosing border - will be done by observer, i.e. his

consciousness that is outside "macrocosm + microcosm" system, i.e. in open system.

In the closed system already, absolutely other picture takes place. There is nobody to open the camera and make decision about Bohr's border. Consequently, there is no decoherence. The Schrödinger's cat becomes as object of a microcosm. Therefore the uncertainty in a macrocosm is increasing and can becomes equal to the uncertainty of a microcosm, i.e. again $\alpha_k = \alpha_q$. In this case already Einstein will be right.

2. DEPENDENCE OF PHYSICAL EXPERIMENT ON STATE OF CONSCIOUSNESS

The knowledge is the product of human brain. The consciousness is property of brain and therefore it participates in origin of knowledge. Clearly, that this participation may be either active, i.e. influencing on origin of knowledge, or passive. Really, in the philosophy there are different kinds and levels of consciousness and scientific knowledge which due to various forms and levels of reflection of objective characteristics of the reality in consciousness of the human. Clearly, that the consciousness is passive, if it is not included in system, system in this case is open. And the consciousness can be active if it is included in system, system in this case closed. Activity or passivity of consciousness is expressed in its ability of influence on reflection of reality, i.e. on knowledge. Having written the active consciousness may influence on reflection of reality it is possible to imply this influence can be directed on reality itself too. Whether so it actually we can not say. But we know the fact that the closed system should differ from open. This difference it is expressed in activity of consciousness which influences reflection and on knowledge. But what reality is being reflected in human consciousness - macro or micro world? It is clear due to percept the reflection of macro world (complete) is one-valued, but the reflection of microcosm (incomplete) - multiple-valued one. Thus in open macro world, i.e. consciousness is a passive, the reflection is an one-valued, the knowledge is an usual - this is the classical physics. In open micro world, i.e. consciousness is a passive, but the reflection is a multi-valued, the knowledge is an unusual - this is the quantum physics. But what will it be in closed system? In close macro world, i.e. consciousness is an active, the reflection is an one-valued, the knowledge is an transcendental - this is the more full scientific knowledge will be getting by us by epistemological analyses. In closed micro world, i.e. consciousness is an active, the reflection is multi-valued, the knowledge is an transiently - this is Kant's theoretical knowledge that by his definition never can be get by us [8]. It concerns to Einstein sub quantum world with its latent parameters too. The physical realities for these cases are known in philosophy as usual, ontological and active [9].

Let's imagine an usual mirror. It is the consciousness of human. The mirror is passive,

because reflection of subjects in it does not depend on itself. Similarly the consciousness is passive, if reflection of reality in it do not depend on itself. Clearly, this passive consciousness is the consciousness in open system, because only in this case the consciousness is similar to a mirror can be counter posed to the being. If around of a mirror there is bright light, for example the sunlight, the reflection of subjects in it will be unequivocal. Clearly, the perception of these subjects will be complete. This case of bright light around of a mirror corresponds to a case of a macrocosm. Really, the macrocosm is the visible world for us. But now we shall imagine, that the mirror is in darkness. Clearly, any image is absent in a mirror This case of full darkness around of a mirror corresponds to a case of a microcosm. Really, the microcosm is the invisible world for us. But we want to receive though any image in a mirror. For this purpose, we artificially illuminate a subject by lamp. This action corresponds to how we investigate a microcosm with the help of devices. Artificial illumination will not be very bright; therefore reflection of subjects in a mirror will not be precise but will be multi - valued. Similarly, the human perception can not be complete in this case. As a result the knowledge can not give us unequivocal precise picture of world. Really, Heisenberg Uncertainties of a microcosm are the proof. The knowledge from these uncertainties is multiple-valued because it is impossible to tell exactly about localization and speed of a micro particle. So, the usual mirror corresponds to passive consciousness. But what mirror will correspond to active consciousness? In this case system is closed and the mirror should be unusual. Such mirror is the false mirror, the reflection of subjects in it depends on itself. To receive false mirror the person makes the act - alters a usual mirror. For this action he should be included in system. Similarly to this action of the person, the consciousness, included in system, can change consciousness, and reflection in it of a reality will depend on it. Therefore the knowledge, being this reflection, will depend on the consciousness. In this case, the consciousness influences on process of an origin of knowledge. As imagines it by phenomenology, reflection of the objective reality will be already actually a stream of consciousness.

3. THE PARADOX OF “ SCHRÖDINGER’S CAT”

It is known, in a macrocosm the some body can be only in one state. Clearly, this knowledge is the usual. In a microcosm the elementary particle can be simultaneously in both states. Of course, such knowledge is the unusual.

The cat's paradox was needed for Schrödinger to show us that unusual phenomena of micro world can transit to macro world due to effect of increasing. Therefore in a macrocosm there is a unusual knowledge too. The Schrödinger's cat paradox, both alive and dead at the same, is being resolved if man looks at inside of the camera, i.e. it depends on

consciousness of the observer. Thus, the consciousness becomes object of quantum physics. Thus on the question: «Where border between macrocosm and microcosm?» it is possible to answer that this border depends on the perception (consciousness) of man. Though we speak about macro object - about a cat - but, it is connected to a microcosm, it is a microcosm until the person doesn't open the camera. The state of Schrödinger cat of simultaneously both alive and dead corresponds to open microcosm. As soon as man look at cat the state of a cat become at once determined, for example alive cat. Such state of a cat corresponds to an open macrocosm - to the world that we see, in which we live. One and the same Shrodinger's cat, but two kind of knowledge about its state – usual and unusual. Unusual knowledge, simultaneously both alive and dead cat, concerns to the entangled state.

In open system the paradox of Schrödinger cat is solved by the decoherence phenomenon [4], i.e. open the camera and find out, that the cat, for example, is alive. Schrodinger magic cat becomes normal cat. As it is explained by Menskii [3] there are some degrees of freedom, including also a brain, i.e. consciousness of the observer that at our measurements gives us the information, for example about Schrodinger cat. Having already statistical ensemble of normal cats, we can use probability theory and do the statistical forecast.

But what is happen with the Schrödinger cat in the closed system? Nobody open camera to look at cat. Is there theory to help us to resolve this paradox? The most interesting theory is the many-world interpretation of quantum mechanics by Everett-Wheeler [5] The closed system is all world, including the observer too. Everyone of a component of superposition describes the whole world, and any of them has not advantage. The question here is not: “What result of measurement will take place?” The question here is: “In what world from many worlds does the observer appear?” In the Everett-Wheeler's theory it depends on consciousness of the observer. Wheeler calls such consciousness “active”. The knowledge in this case is knowledge of active consciousness and it is either an transcendental (such name for this knowledge was given by Kant due to possibilities to reach it) in open system or an trancient (that due to not any possibilities to reach it) in close system.

Let's remember Einstein's quote: «God doesn't play bones with the universe». Menskii M.B. writes in his article [6]: «Yes, the God does not play bones. He equally accepts all opportunities. In a bone plays consciousness of each observer». The author means, that the consciousness of the person, his mind builds the future forecasts, basing on concepts of probability theory. Let us agree, that the world about which speaks Einstein in which the God does not play a bone is the real world. The world in which the human consciousness plays bones is our sensual world. Nevertheless, as wrote Plank [6] besides these two worlds there is also the third world - the world of a physical science or the physical picture of world. This

world is the bridge for us with its help we learn worlds. This world show us the physical reality. Display of the real and sensual worlds in itis the quantum and classical worlds, accordingly.

In physics the classical world is often interpreted, as the objective world but the quantum world exists, as some mathematical image - a vector of a state, i.e. the wave function. Therefore it is not objectively existing world. Such interpretation as says Plank [7], can result in opinion that there is only sensual world and this mistaken opinion cannot be denied by logic way. Because logic itself can not pull out someone from his own sensual world. Plank notes, that besides logic exists also common sense from point of view of which, the interpretation of mutual relation of the worlds will be absolutely another. Namely, the quantum world is the objective world; the classical world is the illusion. However, it is possible to extend this interpretation of the worlds and look on it in anew. As we saw above, in the Schrodinger cat experiment the border between quantum and classical worlds is erased. Therefore, the real world is both objective quantum world and objective classical world. The sensual world is both an illusion of the quantum world and illusion of the classical world. Thus, both quantum and classical worlds consist of components - objective one and illusory. However, can an objective classical world and illusion of the quantum world exist for our perception? The classical world is the world of macroscopic objects and our consciousness sees, perceives this world. This world for us must be sensual world. Illusion of the classical world satisfies to this condition. The quantum world is the world of microscopic objects. This world invisible to us can not be the sensual world. The objective

quantum world satisfies to this condition. Thus, though there are both an objective classical world and illusion of the quantum world, but for us they are outside of a field of our consciousness. One can understand why classical and quantum physics differ from each other. The classical physics is the science studying physical picture of illusion of the classical world. Quantum physics - the science studying physical picture of the objective quantum world.

So, our consciousness has deal the objective quantum world. Menskii M.B.[3] has symbolically represented it as some complex volumetric figure. One of its projections is illusion of the classical world. One can say this complex volumetric figure is a simplex. This simplex is the physical picture of world for us.

4. SIMPLEX INTERPRETATION OF QUANTUM PHYSICS

As it is well known from the functional analysis [10] that one point is 0-dimensional simplex, a line segment is 1-, an triangle is 2-, a tetrahedron is 3-dimensional simplexes. The 3- simplex - the tetrahedron - has four 2-simplex (triangles), six 1-simplex (line segments or edges) and four 0-dimensional simplex (points). The sum of all sides equals to 14. It is impossible to imagine a four-dimensional simplex in perceived by us three-dimensional space. The parallelepiped or cube are not a simplex because for this purpose it is necessary that all 8 points were in six-measured space. Thus, simplex formed by more than four points is already complex volumetric figure.

How can one use simplex for our aim? For example, the tetrahedron (fig.1).

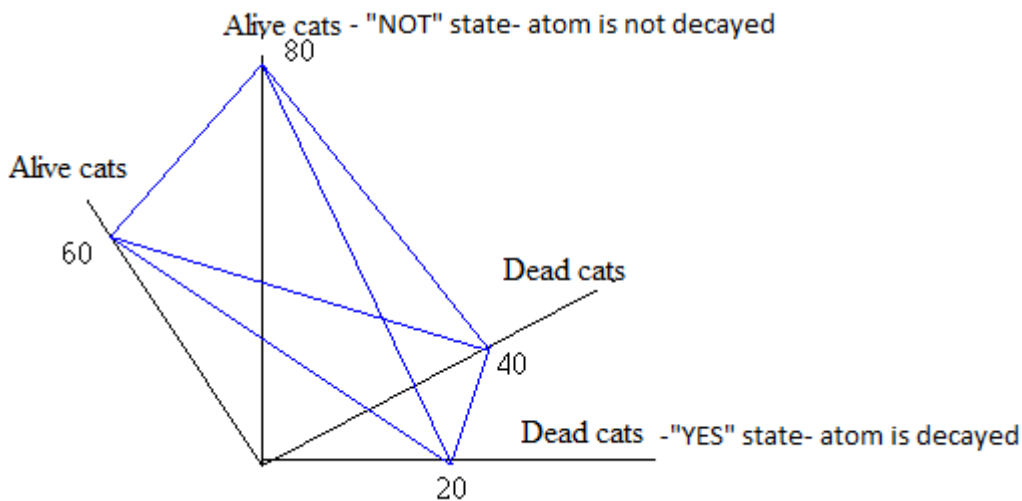


Fig.1. Tetrahedron.

Let's assume its tops are the "events". For example, from 100 schrödinger cats, 80 cats are alive and 20 are dead. Points 20 and 80 are two tops of a simplex. In another case from 100 cats 60 are alive and 40 are dead. These two points are other tops of a simplex. The edges of our tetrahedron indicate to

various probabilities. The edge (80 alive and 20 dead cats) point out the probability of live is equal $80/100=0,8$, the edge (60 alive and 20 dead cats) shows the probability equals to $60/80=0,75$ and etc. The edge linking the points of 20 dead and 40 dead cats and the rib linking the points of 80 alive and 60

alive cats point out probability that is equal 1. Let's consider the faces of our tetrahedron. On one of them the probability changes from $2/3$ to $0,8$; on another face – from $0,75$ to $0,6$; on third - from $2/3$ up to $0,6$; on fourth – from $3/4$ to $0,8$ etc. As to points of a tetrahedron, they specify determinism of event. For example, the point of 80 alive cats specifies that in fact all 80 cats are alive. Thus, the hierarchy of uncertainties is lining up as determinism in event (point of simplex), probability in events (edge of simplex) and fuzziness in events (face of simplex). Here it is appear the conception of fuzziness of event. Lutfi Zadeh's theory of fuzzy sets gives us possibility to consider events with more degree uncertainties. It can suitable for us because foundation of quantum physics itself deals with Heizenberg's Uncertainties. If one "probabilistic" edge of simplex - line segment in tetrahedron - give us only one state of cat, then one "fuzzy" face of simplex - triangle in tetrahedron - give us sets states of cat in one and the same moment of time. Does not it look like on Heizenberg's Uncertainties? Its $\Delta E \Delta t > h$ demands us to consider the sets of energy states instead of one state as it being made in classical mechanics. In classical mechanics, one state is either one scalar or one vector, in quantum physics that is matrix of those.

We were able to construct this simplex with various deterministic points, probabilistic line segments and fuzzy faces because we were observers from outside of. Only such way we can build a physical picture of the real world. The physical picture of the sensual world is not be already as 3 - simplex tetrahedron but it is only point or line segment because we can sensually perceive only projection of simplex - both points and line segments. The point give determined event. For line segment we use the classical probability. In future, although we use probability for triangle face, but only 0- and 1-simplexes deal with the sensual world. But they are illusion because they are not unique, there are set of the worlds alternative points and segments simplex as one whole. Simplex is one whole, we have not able to perceive its whole. In order to perceive simplex as whole it is necessary to change our perception of time. In sensual world the time is perceived by us as moments our life. But in quantum world is the time be as ours and in generally speaking, does quantum world need conception of time?

It is clear, in the physical picture of the real world the Bohr's probabilistic interpretation of the quantum mechanics is true. Although it is called probabilistic interpretation, but it deals with fuzzy faces of simplex. However, will it be right in real world itself? May be Einstein was right when he said «the God does not play bones with universe». Really, for simplex in whole Einstein is right, he is right in the real and sensual worlds. However, in physical picture of real world, for projection of simplex as triangle Bohr was right to apply conception of probability well as we apply probability for projection of simplex as points and line segments, i.e. in a physical picture of sensual world. Having a physical picture of the world, we can even count number of all parallel

worlds. As our world is three-dimensional and our consciousness exists in it we can count only sides of a three-dimensional simplex - a tetrahedron. As it has been shown above, these sides are only 14.

Usually «game in a bone» we mean only the act of throwing of a bone. However game in bones consists of acts of before (we forecast) and after (realization of one forecast). This situation can be identified to a situation on court; there is a hearing an affair, a verdict and process after a verdict. In the physical picture of a real world, game in a bone by consciousness is a game up to the act of throwing of a bone. Our consciousness can only imagine all sides of a three-dimensional simplex, i.e. all alternative results. But the choice of one of them depends on "active" consciousness. In our sensual world, in the act of throwing of a bone, we shall see this choice. In the physical picture of the sensual world, game in a bone by consciousness is a game after the act of throwing of a bone. Having these outcomes allow giving us the statistical forecast.

Thus, uncertainty of the real world qualitatively differs from uncertainty of the sensual world. It is possible to tell, that uncertainty of the sensual world is not present and as a matter of fact, the finding of probability of some casual event has no affair with uncertainty. Perhaps Laplace's demon would say that in the world there is not probabilities, in the world all things are deterministic. The reasons lead to consequences. Here, the probabilities exist for human due to unknowingness. May be he would add that it takes place in your world - in visible and perceived - illusion and sensual one. However, in the real world there is uncertainty and it is principally. Its source is not your unknowingness. Its source is indeterminism itself. It becomes clear, why the quantum statistics essentially differs from classical.

This simplex with various probabilistic ribs and sides we could construct with the help of the epistemological analysis. The knowledge which was analyzed in this case is knowledge of active consciousness. In the case, when the simplex from a volumetric figure is converted into one of its projection, we see only one of its sides (a point, a piece, a triangle). The knowledge appropriate to this case is the knowledge of passive consciousness. In a simplex the pieces (80,20) and (60,40) where a points 80, 60 are alive, and 20,40 are dead cats, correspond to usual knowledge. In this case we use classical statistics (after we have looked in the camera, Schrödinger cats became simple cats, and we already have data, that, for example, from 100 cats in one case 80 alive, and in the other case - 60 and et cetera) With help of this data we find an average and dispersion of a random variable.

But now the ensemble consists not of simple cats, but Schrödinger cats, i.e. we want to tell, that we deal with a microcosm, with the world, the perception of which, as we spoke, is multiple-valued. In this case, for example, the point 80 is fixed already simultaneously and with a point 20, and with a point 40. Therefore the triangle (20,80,40) is examined. Precisely also the triangle (40,60,20) is considered.

These triangles correspond to *unusual* knowledge. In this case we can not apply classical statistics any more. Therefore we use quantum statistics.

There is a question: «But what in a simplex will correspond to transcendental and transiently knowledges?» It is possible to tell, the transcendental knowledge - the knowledge of active consciousness in case of a macrocosm - corresponds all simplex. If transcendental knowledge can be received by us a priori (because we could construct the simplex), but for transiently knowledge it is not possible. As we spoke above, the knowledge of active consciousness appropriate to transition from a microcosm in macrocosm, i.e. to our world will be transcendental, and from a microcosm in a microcosm it will be transient. Really, there is no sharp border between macroworld and microcosms, but in fact there is sharp border between knowledge about them.

5. THE SENSE OF α AND ITS CONNECTION WITH WAVE NUMBER k

In [16] it has been established the connection this α with the wave function in quantum physics. It has been non-uniform differential equation, uniform of which is well-known Shrodinger equation. Really But now it is interesting to understand deeper sence of α . So, the unit of uncertainty α related with the unusual, transcendental and transient knowledge are $\Delta\alpha_k = \frac{A}{N_k}$ and $\Delta\alpha_q = \frac{A}{N_q}$, where A is constant connected with the physiology ability of man to perceive the world around. Because of $N_k \gg N_q$, the quantum world is more uncertain than classical world. Schematically it can be presented as number of lines

in fig.2. The more N, the more number of states which presented by lines or rays. In [9] Svinger images cells instead of our rays.

Perhaps, we can say that considered by us perception and uncertainty α is connected with the Heisenberg Uncertainties. As Wigner has written that the Plank constant is connected with our perception of world. We have said that A is the constant connected with the physiology ability of man to perceive the world around. As it is known the inequality $\Delta k \Delta x \geq 2\pi$ is the result of Heisenberg Uncertainties. Considering minimum number of oscillations, i.e. oscillations of only one kind we account that it is single unit in a phase space (k,x), i.e. $1 = \frac{\Delta k \Delta x}{2\pi}$. It is clear in the

quantum world due to the uncertainty of this world the oscillations must be many kinds and therefore $\Delta k \Delta x \geq 2\pi$. As well similarly this inequality if we consider the number of non observed objects $\Delta n = N_k - n$ equaled to 1, i.e. $1 = \frac{\alpha}{\Delta\alpha} = \frac{\alpha N}{A}$. So, $\alpha N = A$. It

is clear that in the quantum world the number of non observed is more than 1. Therefore,

$$\alpha N \geq A \text{ in quantum world and}$$

$$\alpha N \leq A \text{ in classical world.}$$

These inequalities say us about limited possibility of human perception. In quantum world there is no exact knowledge or information because if $\Delta\alpha=0$ then $N \rightarrow \infty$ what is not correspond to quantum world. It is not possible the measurement of only one state of system.

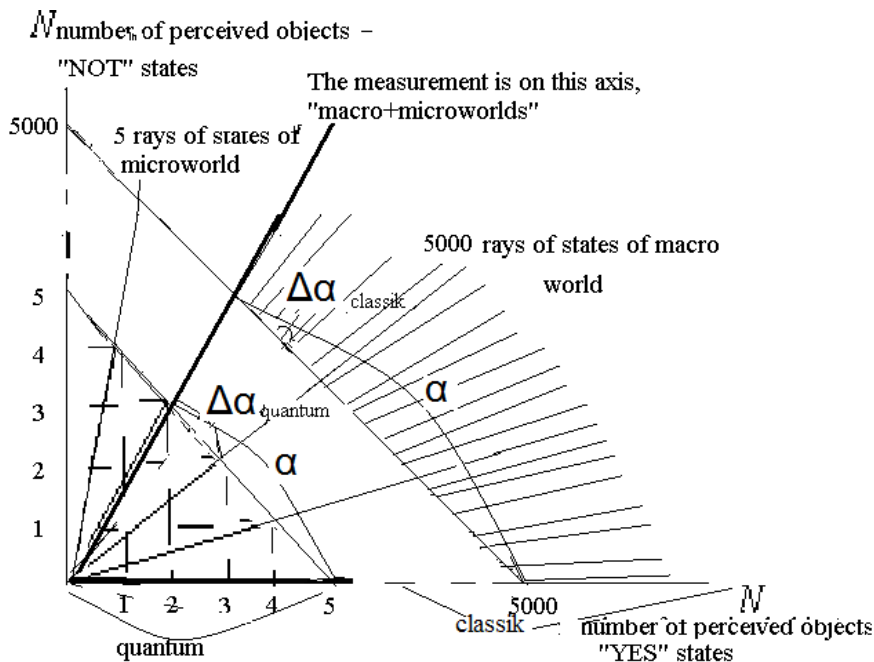


Fig.2. The dependence of the unit of uncertainty $\Delta\alpha$ on the number of perceived objects N, for example N=5 for micro-, N=5000 for macroworlds.

Swinger [5] thinks that fact of measurement is a result selection of event u from set of other possible realization of the physical magnitude U . There is a diaphragm D closing number of state accessible for registration by analyzer A . Analyzer A is connected with the constant connected with the physiology ability of man, i.e. with our A . The diaphragm D is the field between lines in our figure. Obviously, the more N the smaller field between lines. Therefore, here it is not necessary to include the diaphragm D . The transition from microworld to macroworld is a diaphragm. If $N \rightarrow \infty$ then, as Swinger think, all cells are overlapped by diaphragm. On our figure there is no field between lines and, in a results, only one line remains. Therefore, one exact measurement of physical magnitude takes place. Swinger designates such measurement by symbol 0 and he call it by extremely selective measurement. Then the symbol 1 means the extremely nonselective measurements.

Having these two symbols of measurements Swinger introduces operations of sum and multiplication that have algebraic properties, i.e. $1 \times 1 = 1$, $0 \times 0 = 0$, $1 \times 0 = 0 \times 1 = 0$, $1 + 0 = 1$. In these operations one can see that first operations 1×1 is the operation in microcosm and the second operation 0×0 is the operations in the macrocosm. In usual computer the operation 0×0 can take place. Namely third and fourth operations, $1 \times 0 = 0 \times 1$ and $1 + 0$ are operations in the micro world well as macro world. Only these two last operations can take place at creating the quantum computer.

As we can see/from this figure 2, the measurement of same state of objects being in the classical quantum worlds is thin black line of "micro+macroworlds". Many lines near this line in only macro world point on not discret in our measurements in differ from quantum world, where these lines absent and our measurements already is discret.

-
- [1] A. Einstein, B. Podolsky, N. Rosen. Phys. Rev., 47, (1935), 777.
- [2] N. Bohr. Phys. Rev., 48, (1935), 696.
- [3] M.B. Menski. Uspekhi - Physics, 43, (2000), 585-600.
- [4] M.B. Menskii. Uspekhi - Physics, 41, (1998), 923-940.
- [5] H. Everett. Quantum Theory and Measurements. Eds. J.A. Wheeler, W.H. Zurek, Princeton University Press, 1983, 168 p.
- [6] M.B. Menskii. Uspekhi - Physics, 44, 2001, 438-442 (2001).
- [7] Maks Plank. The picture of the world in modern physics. (Uspekhi-Physics), 1929, v.9, №. 4, p. 407-436 (in Russian).
- [8] Kant Immanuel. Critique of Pure Reason, Penguin Classics, 784p.
- [9] Simon Blackburn. Oxford Dictionary of philosophy, 2008, p. 800.
- [10] A.N. Kolmogorov, S.V. Fomin. Elements of the theory of functions and functional analysis, Press. "Nauka", Moscow, 1968, p. 375, (in Russian).
- [11] L.A. Zadeh. Fuzzy Sets, Information and Control, 1965, v.8, p.338-353.
- [12] L.A. Zadeh. Probability Measures of Fuzzy Events, Journal of Mathematical Analysis and Applications, 1968, v.10, p. 421-427.
- [13] L.A. Zadeh. Outline of a New Approach to the Analysis of Complex Systems and Decision Processes, IEEE Transactions on Systems, Man and Cybernetics, 1973, v. SMC-3, p. 28-44.
- [14] L.A. Zadeh. Fuzzy Sets as a Basis for a Theory of Possibility, Fuzzy Sets and Systems, 1978, v.1, p. 3-28.
- [15] B.B. Kadomsev. Dynamics and Information, UFN-Press, Moscow, 1999, p. 400. (in Russian).
- [16] E.A. Issaeva. Physics of Particles and Nuclei Letter, 2007, vol. 4, No. 2, pp. 184 – 188.
- [17] P.E. Wigner. Symmetries and reflections, Indiana University Press, Bloomington-London, 1970, 303p.

Received: 16.04.2021

INFLUENCE OF SINGLE-WALLED CARBON NANOTUBES ON DIELECTRIC AND CONDUCTIVITY PROPERTIES OF SMECTIC A LIQUID CRYSTAL WITH NEGATIVE DIELECTRIC ANISOTROPY

T.D. IBRAGIMOV, A.R. IMAMALIYEV, G.F. GANIZADE, O.A. ALIYEV

Institute of Physics, Azerbaijan National Academy of Sciences,

131 H.Javid Avenue, Baku, AZ1143, Azerbaijan

e-mail:tdibragimov@mail.ru

It was experimentally obtained that the presence of single-walled carbon nanotubes with concentration of 0.5% in the smectic liquid crystal with negative dielectric anisotropy reduces the transition temperature from the smectic to isotropic state. Both the longitudinal and transverse components of dielectric permittivity and the dielectric anisotropy are shown to increase in the presence of nanotubes. At the same time, the resulting percolation effect contributes to the increase in conductivity.

Keywords: liquid crystal, single-walled carbon nanotubes, dielectric relaxation, electric conductivity, threshold voltage.

PACS: 64.70.mj;64.70.pv;77.84.Nh;82.70.Dd.

1. INTRODUCTION

Single-walled carbon nanotubes (SWCNTs) have a diameter comparable to cross-section of elongated liquid crystal (LC) molecules. Rod-like particles of SWCNTs in nematic LC cause the effective orientational coupling with LC molecules [1]. The charges transfer from LC molecules to the particles and they are distributed asymmetrically on the SWCNTs inducing a permanent dipole moment on them [2, 3]. As a result, SWCNTs are oriented parallel to the LC director enhancing the orientation order and consequently, the display parameters of composite systems improved [3-5]. Moreover, liquid crystals provide a medium for controlling the alignment of carbon nanotubes [6].

It was shown in [7-9] that the inclusion of SWCNTs in the nematic matrix with positive dielectric anisotropy increases the nematic-isotropic transition temperature. In this case, the dielectric anisotropy increases and the threshold voltage decreases at tiny amount (0.01-0.02 wt. %) of SWCNTs [7-9]. In the works [10-11], SWCNTs were dispersed in nematic liquid crystal 4-pentyl-4'-cyanobiphenyl at the concentration of 0.02 and 0.05 wt%. Differential scanning calorimetry and temperature-dependent dielectric studies suggest decrease in clearing temperature of the composite materials as compared to the pure material. Ionic conductivity increases by two orders of magnitude due to the dispersion of such a low concentration (0.05 wt%) of SWCNTs. Dielectric studies also show that the presence of the SWCNTs decreases the effective longitudinal as well as transverse components of the dielectric permittivity. From frequency-dependent dielectric studies, important dielectric parameters such as relaxation frequency, dielectric strength and distribution parameters have been determined. Electro-optical experiments show that the threshold voltage decreases and the steepness of the transmission voltage curve improves due to the dispersion of SWCNTs. Presence of SWCNTs increases the relaxation frequency corresponding to flip-flop motion of molecules around

their short axes. A significant enhancement in the dielectric anisotropy and conductivity of SWCNTs doped p-ethoxybenzylidene *p*-butylaniline nematic LC at concentration of 0.01 and 0.02 wt.% was observed in the work [12].

The photoresponsive electro-optical composites based on the cholesteric liquid crystal with optically controlled chirality and a minute amount of SWCNTs are studied in [13]. It is found that this composite demonstrates dual-mode operation with optical switching between reversible and memory mode. Authors of the work [14] studied the conductivity and dielectric anisotropy change in cholesteric LC system doped with SWCNTs. The results lead to the conclusion that the enhancement of the electrical conductivity and the change of the dielectric anisotropy in the SWCNT doped cell is mainly caused by the aligning effect of cholesteric liquid crystal system. It was shown in [15] that the inclusion of SCNTs significantly affect on the dielectric parameters in the chiral smectic *C* phase with an inversion of the effect near the transition to, and in, the chiral smectic *A* phase. It is demonstrated in [16] that even a small amount of chiral SWCNTs affects greatly on the performance of ferroelectric liquid crystal cells. Particularly, the spontaneous polarization, the Goldstone mode dielectric strength and the rise time are decreased in doped cells. Under high electric field, highly concentrated SWCNT doped ferroelectric LC shows enormously large values of dielectric loss [17]. This is due to the high conductivity of SWCNT at higher electric field. Influence of SWCNTs on the re-entrant phenomenon in LCs has been studied in [18]. Here a small concentration (0.5 wt. %) of SWCNTs doped to a nematic material not only induces the layered smectic *A* mesophase but also leads to the nematic-smectic-nematic re-entrant sequence.

It is known that continuous network of SWCNTs is formed in the LC colloid at a certain concentration. The structural percolation transition takes place for LC doped with SWCNTs at concentrations between 0.02 and 0.2 wt % [19].

The aim of this work is to study the effect of

SWCNTs at concentration of 0.5wt.% on the dielectric and conductivity properties of smectic A liquid crystal 4-hexyloxyphenyl ether of 4'-hexyloxy-3'-nitrobenzoic acid.

EXPERIMENTAL

We used smectic A liquid crystal 4-hexyloxyphenyl ether of 4'-hexyloxy-3'-nitrobenzoic acid with negative dielectric anisotropy as a matrix.

The temperature range of smectic phase is located between 30°C and 71°C. A presence of nitrophenyl dipole group -C-NO₂ of this LC is the reason of the large negative dielectric anisotropy.

The single-walled carbon nanotubes (US, Research Nanomaterials, In.) were added into the liquid crystal with concentration of 0.5 wt.%. Then obtained mixture was shaken in a vortex mixer for 1 hour at temperature 80°C, followed by sonication with dispergator Ultrasonic Cleaner NATO CD-4800 (China) for 4 hours.

The cell had a sandwich structure and consisted of two plane-parallel glass plates whose inner surfaces were coated with thin transparent and conductive indium-tin-oxide (ITO) layer. Planar orientation of molecules was attained by coating the inner substrate surfaces with rubbed polyimide layers. For obtaining of homeotropic orientation of LC molecules, we used the surfactant (polysiloxane). The cell thickness was fixed with calibrated 20 μm polymer spacers for measurements. Both the colloid and the pure LC were injected into the empty cell by capillary action at the isotropic state. To increase the dispersion, the cells with the colloid were placed at electric field of 40 V to achieve turbulence and were kept for 2 days. In this case, no aggregation of particles was observed. The stuffed cell was kept in the special heater with temperature regulator GL-100 (China). The copper-constantan thermocouple was used for temperature control. An accuracy of temperature determination was 0.1°C.

Dielectric and conductivity measurements were carried out by the Precision LCR Meter 1920 (IET Labs. Inc., USA) in the frequency range of 20 Hz – 1MHz. In this case, applied voltage was 0.5 V for both LC molecular orientations.

2. RESULTS AND DISCUSION

Observation of the change in texture under a polarizing microscope shows that the appearance of dark areas in the liquid crystal and the colloid is observed at temperatures of 70.9°C to 68.3°C, respectively. It indicates that the clearing points for the pure liquid crystal and the colloid occur at the indicated temperatures.

Fig. 1 shows the dependences of real ε' and imaginary ε'' parts of dielectric permittivity of the pure liquid crystal and the colloid at planar configuration at temperature 32°C. As seen, ε' of the pure LC decreases

from the value of 14.02 at 40 Hz to 13.20 at 2 kHz, then it decreases sharply after 30 kHz. Values of ε' for the colloid are greater than for the pure LC at all frequencies. It varies from 15.52 at 40 Hz to 15.33 at 2kHz, then its value also decreases sharply after 30 kHz. The presence of nanotubes increases the values of ε''. In this case, the dielectric absorption maximum shifts to the low-frequency region from 200 kHz to 130 kHz.

It is known that the relaxation time of LC molecules which is characterized by their overturn from one to the opposite direction, is determined by the ratio

$$\tau = \frac{1}{2\pi f} \tag{1}$$

where f is the frequency of the applied electric field. The additive of nanotubes increases the relaxation time from 8.0·10⁻⁷s to 1.22·10⁻⁶s at 32°C. The increase in the relaxation time indicates that the single-walled carbon nanotubes in the liquid crystal prevent the flip-flop motion of the molecules. It promotes to an increase in rotational viscosity for the colloid.

The frequency dependences of the real and imaginary parts of dielectric permittivity for the pure LC and the colloid at homeotropic configuration and temperature 32°C are presented in fig. 2. As can be seen, ε' of the pure LC is equal to 4.25 at 40 Hz, then there is a dispersion near 500 Hz and its value remains almost unchanged and equal to 3.91 up to 100 kHz then decreases sharply. The additive of nanotubes increases value of ε' to 4.90 at 40 Hz and 4.78 at 2 kHz. Here the dispersion is also observed near the frequency of 1 kHz. The dielectric absorption maximum of the pure LC and the colloid is observed around 500 Hz. Obviously, this dispersion is connected with dipole fragment -C-NO₂, which is not strictly perpendicular to the long axis of the molecules, but has a component parallel to its long axis. It should be noted that the dielectric anisotropy of the pure LC is -9.75 at the frequency of 40 Hz while this value is -10.23 for the colloid. Note also that the dielectric anisotropy of liquid crystal is -9.29 at 2 kHz while it is -10.55 for the colloid. That is, the dielectric anisotropy increases with the additive of particles.

It is known that the gap between the layers of smectic LC have a width greater than the transverse dimension of nanotubes. Therefore, a part of nanotubes is located between layers. An another part of nanotubes is located along the predominant direction of LC molecules. Exactly this part of nanotubes interacts with LC molecules. This interaction is dipole-dipole, as asymmetric molecules of the liquid crystal induce asymmetric arrangement of charges on nanotubes turning them into dipoles. In the same time, the ordered arrangement of the LC molecules is improved. In this case, the dipole of the LC molecule directed at an angle of 60° to the long axis of the molecule, plays a special role. In this connection, it is not possible to judge the change in the order parameter.

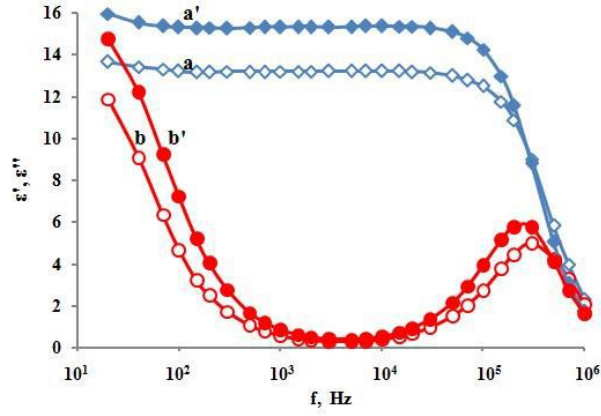


Fig.1. Frequency dependences of real ε' and imaginary ε'' components of dielectric permittivity at planar configuration (temperature 32°C): (a) ε' of the pure liquid crystal, (a') ε' of colloid, (b) ε'' of the pure liquid crystal, (b') ε'' of the colloid.

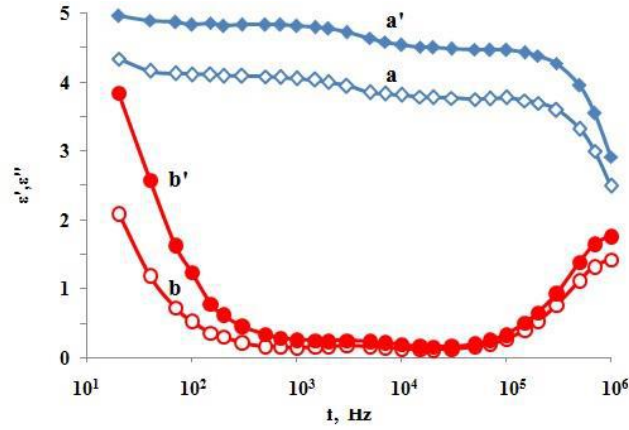


Fig.2. Frequency dependences of real ε' and imaginary ε'' components of dielectric permittivity at homeotropic configuration and 0.5% concentration (temperature 32°C): (a) ε' of the pure liquid crystal, (a') ε' of the colloid, (b) ε'' of the pure liquid crystal, (b') ε'' of the colloid.

In rough approximation, the Maier-Meier theory can be used to analyze the results of dielectric measurements of the smectic LC, although this theory

was developed for nematic liquid crystals. According to this theory, the dielectric permittivity components are defined as [20]:

$$\varepsilon'_{\parallel} = 1 + \frac{NHF}{\varepsilon_0} \left\{ \gamma_{av} + \frac{2}{3} S \Delta\gamma + F \frac{p_e^2}{3k_B T} \left[1 - (1 - 3\cos^2 \beta) S \right] \right\} \quad (2)$$

$$\varepsilon'_{\perp} = 1 + \frac{NHF}{\varepsilon_0} \left\{ \gamma_{av} - \frac{1}{3} S \Delta\gamma + F \frac{p_e^2}{3k_B T} \left[1 + \frac{1}{2} (1 - 3\cos^2 \beta) S \right] \right\} \quad (3)$$

and the dielectric anisotropy is given by:

$$\Delta\varepsilon' = \frac{NHF}{\varepsilon_0} \left[\Delta\gamma - F \frac{p_e^2}{2k_B T} (1 - 3\cos^2 \beta) \right] S \quad (4)$$

where F is reaction field factor, H is the cavity form factor, $\gamma_{av} = (\gamma_{\parallel} + 2\gamma_{\perp})/3$ is the average value of polarizability of LC molecules, $\Delta\gamma = \gamma_{\parallel} - \gamma_{\perp}$ is the anisotropy of polarizability, N is the number of LC molecules per unit volume, S is the order parameter, β is the angle between the point molecular dipole p_e and the axis of maximum molecular polarizability, ε_0 is

dielectric permittivity of vacuum, k_B is Boltzmann constant, T is Kelvin temperature.

Since the dipole moment of this LC is directed at an angle of 60° to its long axis, respectively, to the direction of maximum polarizability, that is, angle $\beta=60^\circ$, $\cos\beta=1/2$ and $1-3\cos^2\beta=1/4$. Then the Maier-Meier equations can be represented in the form:

$$\varepsilon'_{\parallel} = 1 + \frac{NHF}{\varepsilon_0} \left\{ \gamma_{av} + \frac{2}{3} S \Delta\gamma + F \frac{p_e^2}{3k_B T} \left[1 - \frac{1}{4} S \right] \right\} \quad (5)$$

$$\varepsilon'_{\perp} = 1 + \frac{NHF}{\varepsilon_0} \left\{ \gamma_{av} - \frac{1}{3} S \Delta\gamma + F \frac{p_e^2}{3k_B T} \left[1 + \frac{1}{8} S \right] \right\} \quad (6)$$

Using (5-6) we obtain:

$$\Delta \varepsilon' = \frac{NHF}{\varepsilon_0} \left[\Delta \gamma - F \frac{p_e^2}{8k_B T} \right] S \quad (7)$$

Let us denote by $\Delta S = S - S_0$, where S is the order parameter of the liquid crystal doped with nanotubes, S_0 is the order parameter of the pure LC; $\Delta \varepsilon'_{||}$ is the difference between the longitudinal component of the real part of the dielectric permittivity after doping and before doping of the liquid crystal; $\Delta \varepsilon'_{\perp}$ is the difference between the transverse component of the real part of the dielectric permittivity after and before doping of the liquid crystal; $\Delta(\Delta \varepsilon')$ is the difference between the dielectric anisotropy after and before doping the liquid crystal. Then you can write:

$$\varepsilon'_{||} = \frac{2NHF}{3\varepsilon_0} \left\{ \Delta \gamma - F \frac{p_e^2}{8k_B T} \right\} \Delta S \quad (8)$$

$$\varepsilon'_{\perp} = -\frac{NHF}{3\varepsilon_0} \left\{ \Delta \gamma - F \frac{p_e^2}{8k_B T} \right\} \Delta S \quad (9)$$

Their difference gives the change in dielectric anisotropy:

$$\Delta(\Delta \varepsilon') = \frac{NHF}{\varepsilon_0} \left[\Delta \gamma - F \frac{p_e^2}{8k_B T} \right] \Delta S \quad (10)$$

The experiment shows that the longitudinal and transverse components of the dielectric permittivity increase with the additive of SWCNs: $\Delta \varepsilon'_{||} > 0$ and $\Delta \varepsilon'_{\perp} > 0$. In addition, the dielectric anisotropy difference also increases, that is, $\Delta(\Delta \varepsilon') > 0$, although it decreases in absolute value. Obviously, the simultaneous implementation of conditions (8), (9) and (10) is impossible with these experimental results. Consequently, automatic use of the Maier-Meier theory for the analysis of the experimental results for the smectic LC with large dielectric anisotropy cannot be made. In addition, the possibility of interaction of the emerging dipole moments of nanotubes with the dipole moments of the liquid crystal, the direction of which has a certain angle with the long axis of the molecule, plays a certain role.

Frequency dependences of specific conductance of the pure LC and the colloid are shown in fig. 3. As can be seen, the dispersion associated with the $-C-NO_2$ dipole fragment is also observed here. In this case, the additive of particles slightly increases the specific conductance up to this dispersion then it decreases. In particular, the longitudinal component increases from $1.72 \cdot 10^{-5}$ S/m to $2.45 \cdot 10^{-5}$ S/m and the transverse component changes from $9.92 \cdot 10^{-7}$ S/m to $1.80 \cdot 10^{-6}$ S/m at the frequency of 100 Hz. That is, the ratio $\sigma_{||}/\sigma_{\perp}$ is 17.3 for the pure LC while it becomes 13.6 for the colloid. The longitudinal component increases from $1.90 \cdot 10^{-1}$ S/m to $2.32 \cdot 10^{-1}$ S/m and the transverse component almost does not change and is equal to $1.42 \cdot 10^{-2}$ S/m at the frequency of 300 kHz. That is, the ratio $\sigma_{||}/\sigma_{\perp}$ in pure liquid crystal was 13.4 for the pure LC and becomes 16.3 when nanotubes are added.

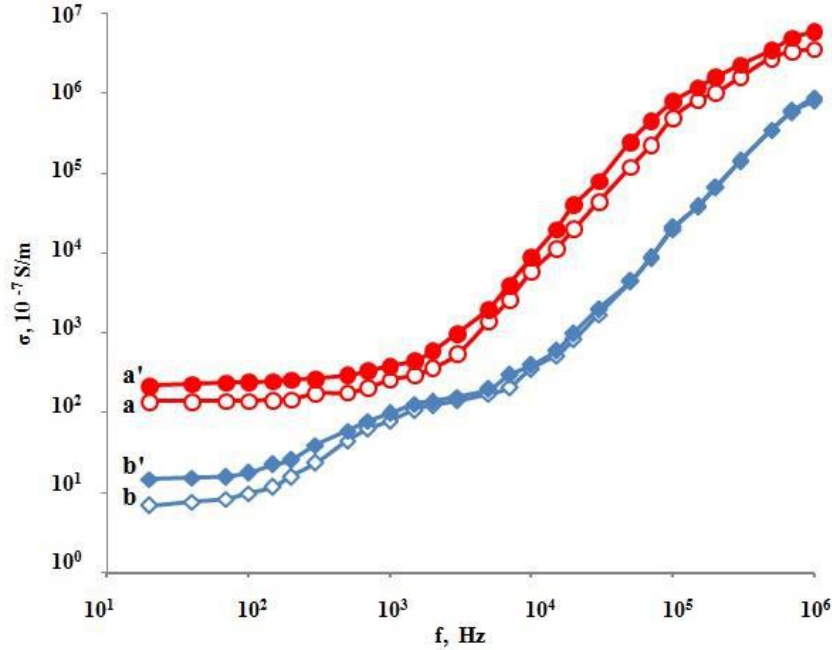


Fig.3. Frequency dependence of specific conductance components at 32°C: (a) $\sigma_{||}$ of the pure LC, (a') $\sigma_{||}$ of the colloid, (b) σ_{\perp} of the pure LC, (b') σ_{\perp} of the colloid.

The increase in electric conductivity at low and medium frequencies is due to the percolation effect when nanotubes are added into the liquid crystal. A

space set of conducting nanotubes is formed. In this case, there is predominance of electronic hopping conductivity over ionic conductivity. At high

frequencies, the molecules of the liquid crystal do not keep up with the changes in the direction of the electric field. Therefore, there is a sharp increase of conductivity at high frequencies. At the same time, the reversal of molecules in the colloid at application of

electric field along the long axis of the molecules is hindered because of the increase of rotational viscosity relative to the pure LC. It is consistent with the increase in dielectric relaxation time.

-
- [1] *S.V. Burylov, Yu.L. Raikher*. Phys. Rev. E 1994, 50, 358-367.
- [2] *N.R. Jber, A.A. Rashad, M.S. Shihab*. J. of Molecular Structure 2013, 1043, 28–36.
- [3] *D. Singh, U. Bahadur, S.M. Bhushan, R.Dabrowski, R. Dhar*. Materials Letters. 2018, 216, 5-7.
- [4] *M.D. Lynch, D.L. Patrick*. Nano Lett., 2002, 2(11), 1197–1201.
- [5] *K.A. Park, S.M. Lee, S.H. Lee, Y.H. Lee*. J. Phys. Chem. C 2007, 111, 1620-1624.
- [6] *S.P. Yadav, S. Singh*. Progress in Materials Science 2016, 80, 38-76.
- [7] *L. Dolgov, S. Tomylo, O. Koval'chuk, N. Lebovka, O. Yaroshchuk*. Liquid Crystal Dispersions of Carbon Nanotubes: Dielectric, Electro-Optical and Structural Peculiarities. In Carbon Nanotubes; Marulanda, J.M., Ed.; Intech: Rijeka, Croatia, 2010; pp. 451-484.
- [8] *D. Singh, U.B. Singh, M.B. Pandey, R.Dabrowski, R. Dhar*. Optical Materials 2018, 84, 16-21.
- [9] *D. Singh, U.B. Singh, M.B. Pandey, R. Dhar*. Dielectric and Electro-Optic Behaviour of Nematic-SWCNT Nanocomposites under Applied Bias Field. Liquid Crystals 2019, 46, 1389-1395.
- [10] *R. Verma, M. Mishra, R. Dhar, R.Dabrowski*. Enhancement of Electrical Conductivity, Director Relaxation Frequency and Slope of Electro-Optical Characteristics in the Composites of Single-Walled Carbon Nanotubes and a Strongly Polar Nematic Liquid Crystal. Liquid Crystals 2017, 44, 544-556.
- [11] *R. Verma, M. Mishra, R. Dhar, R.Dabrowski*. Single Walled Carbon Nanotubes Persuaded Optimization of the Display Parameters of a Room Temperature Liquid Crystal 4-pentyl-4'-cyanobiphenyl. Journal of Molecular Liquids 2016, 221, 190-196.
- [12] *T. Vimal, S. Pandey, S.K. Gupta, D.P. Singh, R. Manohar*. Journal of Molecular Liquids 2015, 204, 21-26.
- [13] *R. Yamaguchi*. Cholesteric Liquid Crystal–Carbon Nanotube composites with Photo-Settable Reversible and Memory Electro-Optic Modes. Applied Optics 2013, 52, E53-E59.
- [14] *O. Köysal*. Conductivity and Dielectric Properties of Cholesteric Liquid Crystal Doped with Single Wall Carbon Nanotube. Synthetic Metals 2010, 160, 1097-1100.
- [15] *N. Sood, S. Khosla, D. Singh, S.S. Bawa*. Dielectric Investigations of Pure and Carbon Nanotube-Doped Deformed Helix Ferroelectric Liquid Crystals 2012, 39, 1169-1174.
- [16] *F.V. Podgornov, A.M. Suworova, A.V. Lapanik, W. Haase*. Chem. Phys. Lett. 2009, 479, 206-210.
- [17] *S.K. Kumar, A.K. Srivastava, R. Manohar, R. Modification* in Dielectric Properties of SWCNT Doped Ferroelectric Liquid Crystals. J. of Non-Crystalline Solids 2011, 357, 1822-1826.
- [18] *G.V. Varshini, D.S. Shankar Rao, P.K. Mukherjee, S.K. Prasad*. Nanophase Segregation of Nanostructures: Induction of Smectic A and Re-Entrance in a Carbon Nanotube/Nematic Liquid Crystal Composite. J. Phys. Chem. B 2018, 122, 10774-10781.
- [19] *V.V. Ponevchinsky, A.I. Goncharuk, V.I. Vasil'ev, N.I. Lebovka, M.S. Soskin*. Cluster Self-Organization of Nanotubes in a Nematic Phase: the Percolation Behavior and Appearance of Optical Singularities. JETP Letters 2010, 91, 239–242.
- [20] *W. Maier, G. Meier*. Eine Einfache Theorie der Dielektrischen Eigenschaften Homogen Orientierter Kristallinflüssiger Phasen des Nematischen Typs. J. Z. Naturforsch A, 1961, 16, 262–267.

Received: 06.05.2021

SPATIAL STRUCTURE OF N¹H AND N³H TAUTOMERS OF CARNOSINE IN ZWITTERION FORM

G.A. AKVERDIEVA, I.N. ALIEVA, Z.I. HAJIYEV, S.D. DEMUKHAMEDOVA

Institute for Physical Problems, Baku State University

Z. Khalilov st.23, AZ-1148, Baku, Azerbaijan

e-mail: gulnaraakverdieva@bsu.edu.az; svetlanademukhamedova@bsu.edu.az

Conformational profiles of N¹H and N³H tautomers of carnosine in zwitterion form are investigated within framework of molecular mechanics. It is found that the stability of the spatial structure of this sequence is determined by the relative positions of its functional groups. Thus, the most stable conformations for both carnosine tautomers are characterized by close arrangement of α -amino group, C-terminal carboxyl group and imidazole ring of *L*-histidine in space. The salt bridges between nitrogen atom of α -amino group and oxygen atoms of deprotonated carboxyl group are revealed in these structures. The effects of intramolecular hydrogen bonding on geometry of molecule are observed in the investigated tautomers of carnosine.

Keywords: molecular mechanics; spatial structure; conformation; carnosine

PACS: 36.20.Ey; 36.20.Fz; 36.20.Hb

1. INTRODUCTION

Carnosine (β -alanyl-*L*-histidine, β -Ala-*L*-His) has antioxidant properties, therefore it is successful used at the treatment of various inflammatory processes that occur against the background of cell membrane damage; it has also ability to recognize dangerous molecules and neutralize them by chemical binding [1-3]. The zwitterion form of this dipeptide takes part in complex formation with ion metals and shows the important pharmacological activity. Many works are devoted to spectroscopic and structural characterization of carnosine [4-7]. However, in these studies the systematic conformational analysis was not carried out. To understand the mechanism of activity of the drug under investigation it is necessary to explore its conformational possibilities and determine bioactive conformation. The aim of this work is to investigate the conformational behavior of N¹H and N³H tautomers of carnosine in zwitterion form by molecular mechanics to provide an improved description of the structure-functional interrelation to enable the designing of products for new medical applications. The geometry and energy parameters of the most stable conformations of both tautomers of carnosine are calculated.

2. COMPUTATIONAL METHODS

The conformational profiles of carnosine molecule in zwitterion form are investigated within framework of molecular mechanics as it is described in [8]. The conformational potential energy of this molecule is given as the sum of the independent contributions of nonvalent (E_m), electrostatic (E_{el}), torsional (E_{tor}) interactions and hydrogen bonds energy (E_{hb}). The energy of nonvalent interactions was described by the Lennard-Jones 6-12 potential with the parameters proposed by Scott and Sheraga [9]. The contribution of electrostatic interactions was taken into account in a monopole approximation corresponding to Coulomb's law with partial charges

of atoms suggested by Scott and Sheraga [9]. The effective dielectric constant \mathcal{E} was taken to be equal to ten described by Lipkind et al. [10]. A torsion energy was calculated using the value of internal rotation barriers given by Momany et al. [11]. Hydrogen bonding energy was calculated based on Morse potential and dissociation energy of the hydrogen bond was taken to be 1.5 kcal/mol. A rigid valence scheme of the molecule was assumed, namely, the searches were made only on torsion angles. Conformational energy calculations were made with an IBM computer using a program in FORTRAN [12,13]. The program was developed from the matrix method principle of Hermans and Ferro [14]. The accepted nomenclature and conventions are recommended by IUPAC-IUB [15]. The computer modelling of the calculation results was carried out using the demonstration version of software package HyperChem (<http://www.hyper.com>).

3. RESULTS AND DISCUSSION

The conformational state of this molecule is characterized by dihedral angles of backbone and side chains (τ_1 , τ_2 , τ_3 , ω , φ , χ_1 , χ_2 , ψ) (Fig.1). The term "conformation" or "conformation state", used in the analysis of calculation results, will always imply exact quantitative characteristics of the geometry of this dipeptide. The calculated carnosine conformations were compiled on the basis of low-energy states of its amino-acid residues. β -alanyl is a non-standard amino-acid residue, because in it the C ^{β} atom is bound to the carbon of the subsequent carbonyl group. For this reason, we designated its dihedral angles by τ_1 , τ_2 , τ_3 .

In order to determine the possible values of the dihedral angles that correspond to the low-energy states of β -alanyl the conformational maps of the potential surfaces over the τ_1 - τ_2 , τ_2 - τ_3 , τ_1 - τ_3 angles were constructed. Thus, the dihedral angles around N - C ^{α} , C ^{α} - C ^{β} , C ^{β} - C' bonds of the peptide chain of this residue were varied and their optimal values were

determined. The conformational maps given in the Fig.2-4 were constructed by step of 30° and by step of 5° in the low-energy regions. The values of the dihedral angles corresponding to the optimal energy

are marked by crosses, and the relative energy on equipotential lines is given in kcal/mol.

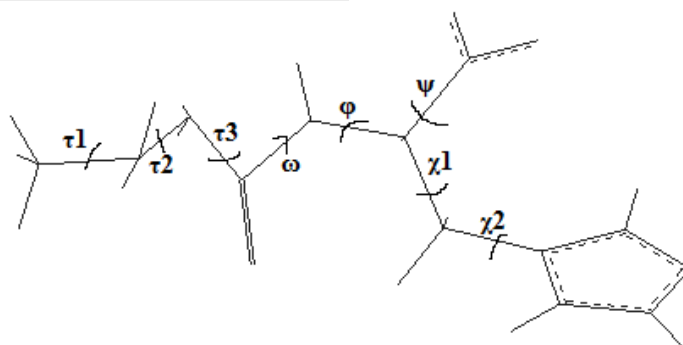


Fig.1 Calculated model of carnosine molecule.

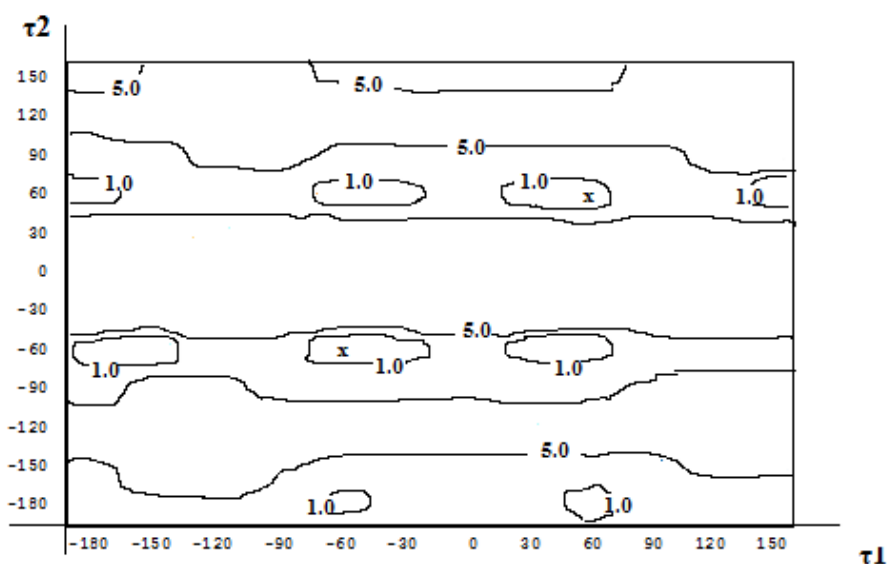


Fig.2. Conformational energy map over τ_1 - τ_2 angles of β -alanyl amino-acid residue.

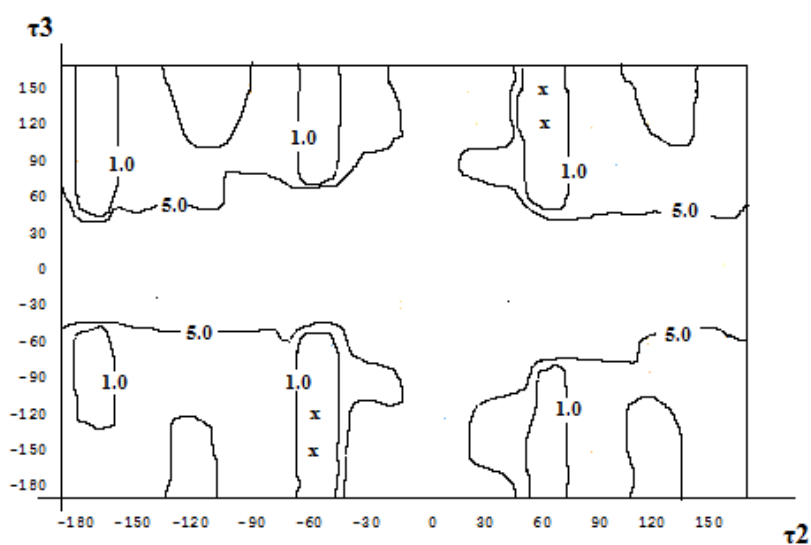
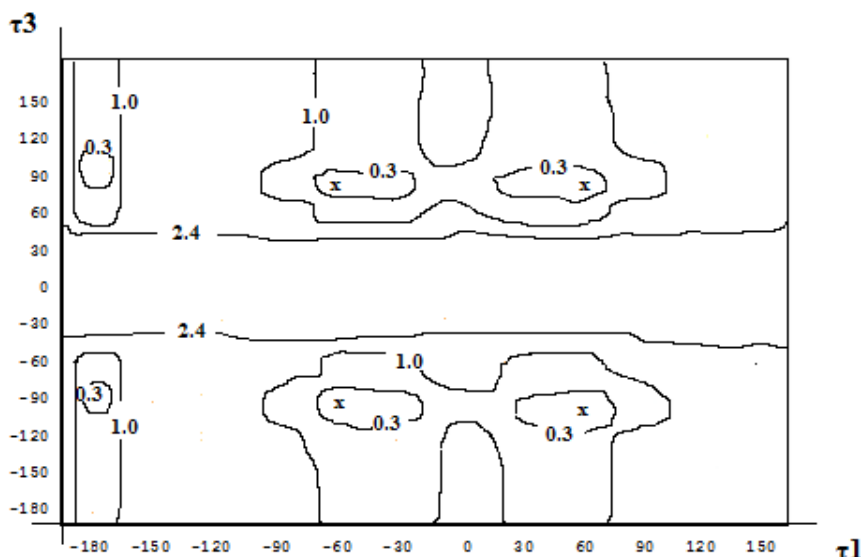


Fig.3. Conformational energy map over τ_2 - τ_3 angles of β -alanyl amino-acid residue.


 Fig.4. Conformational energy map over τ_1 - τ_3 angles of β -alanyl amino-acid residue

For calculation of carnosine molecule, the values of dihedral angles defining 8 forms of the backbone of β -alanyl residue marked by symbols A1-A8 are selected from the conformational maps and are represented in Table 1. Note that conformations A1, A2, A3, A4 are the same as A7, A8, A5, A6,

respectively, since they differ only on angle τ_1 , which determines the isoenergetic position of three hydrogen atoms relative to the rest part of the molecule. This fact was taken into account in the subsequent analysis of the characteristic conformations of carnosine.

Table 1.

The dihedral angles (in degree) of the low-energy states A1-A8 of β -alanyl amino-acid residue

Angles	A1	A2	A3	A4	A5	A6	A7	A8
τ_1	-60	-60	-60	-60	60	60	60	60
τ_2	-60	-60	60	60	60	60	-60	-60
τ_3	90	-90	90	-90	90	-90	90	-90

For stable conformations of L-histidine the ϕ and ψ dihedral angles of backbone chain are located in the low energy regions R ($\phi, \psi = -180^\circ - 0^\circ$), B ($\phi = -180^\circ - 0^\circ$, $\psi = 0^\circ - 180^\circ$), L ($\phi, \psi = 0^\circ - 180^\circ$) of the Ramachandran's map. Therefore the conformational state of this residue is conveniently described by X_{ij} , where X is the backbone form of a residue (R, B, L), and $ij = 11, 13, 21, 23, 31, 33$ specify the positions of a side chain (χ_1, χ_2), the index '1' corresponds to the angle χ in the range from 0° to 120° , '2' corresponds to the angle range from 120° to -120° and '3' from -120° to 0° .

The possible stable conformational states of the histidine side chain corresponding to torsion minima: to three values $60^\circ, 180^\circ, -60^\circ$ of the dihedral angle χ_1 and two values 90° and -90° of the dihedral angle χ_2 , orienting the aromatic ring, were considered. The initial values of dihedral angles of low-energy conformations of L-histidine using for calculation of carnosine molecule are given in Table 2. Based on the foregoing, 288 conformations were calculated for two tautomers of this dipeptide.

Table 2.

The initial values of dihedral angles (in degree) corresponding to the low-energy states of L-histidine amino-acid residue

Backbone form	ϕ	ψ	χ_1	χ_2
R	-100	-40	60	90, -90
	-120	-60	180	90, -90
	-120	-60	-60	90, -90
B	-120	160	60	90, -90
	-120	140	180	90, -90
	-140	140	-60	90, -90
L	60	80	60	90, -90
	60	100	180	90, -90
	60	60	-60	90, -90

The massiveness of the side chain of histidine amino-acid residue and also existence of the N- and C-terminal opposite charged groups of atoms are important factors, which form the stabilizing forces: dispersion contacts of L-histidine amino-acid residue and electrostatic interactions of the protonated α -amino group and the partially protonated imidazole side chain with deprotonated C-terminal carboxyl group of this molecule. Therefore, the energy of dipeptide is very sensitive to the positions of the mentioned parts of this molecule. The observed differentiation of the calculated conformations on energy is determined both nonvalent and electrostatic interactions. The energy parameters of the favorable conformations for tautomers of this dipeptide are given in Tables 3 and 4. The calculation results reveal that 10% of the examined conformations of this dipeptide have the relative energy up to 3 kcal/mol. It is shown that β -alanyl fragment is more mobile than other segment of this molecule, therefore it may bend α -amino group (H_3N^+) towards C-terminal carboxyl group (COO^-) or L-histidine imidazole ring. The spatial structure of both tautomers of carnosine molecule may be characterized by three types of

conformations (I, II, III), which are determined by different arrangement of mentioned functional groups. In the conformations of I type group H_3N^+ , group COO^- and imidazole ring of L-histidine are closely spaced; in the conformations of II type groups H_3N^+ and COO^- are closely spaced, but imidazole ring of L-histidine is turned away; in the conformations of III type group H_3N^+ and imidazole ring of L-histidine are closely spaced, but group COO^- is turned away. For both tautomers the conformations of I, II, III types are characterized by R, L, B forms of His backbone respectively. As it is seen from the represented results in the conformations of I type the dispersion, electrostatic and torsion interactions are the best balanced, so they are most stable for both tautomers. The conformations of II type are inferior in energy to torsion interactions on 1 - 1.6 kcal/mol. The best representatives of II type are inferior in total energy on 1.3 kcal/mol. Only the conformations of III type proved to have high energy; the best representatives of these conformational type for both carnosine tautomers are inferior in energy on 4 - 5 kcal/mol to global conformation.

Table 3.

Energy parameters (in kcal/mol) of the favorable conformations for N^1H tautomer of carnosine

Type	Conformation of molecule	Energy interaction of β -Ala and L-His	$E_{nonval.}$	$E_{elst.}$	$E_{tors.}$	$E_{tot.}$
I	A4-R ₁₁	-14.61	-6.87	-4.96	2.14	-9.69
	A4-R ₂₁	-14.29	-6.01	-5.13	2.42	-8.72
	A4-R ₃₁	-14.60	-6.09	-4.97	1.95	-9.11
	A6-R ₁₁	-14.99	-6.78	-5.14	2.57	-9.35
	A6-R ₂₁	-14.41	-6.09	-5.10	2.73	-8.46
	A6-R ₃₁	-10.16	-4.93	-3.37	1.08	-7.23
	A8-R ₁₁	-14.86	-6.30	-5.15	2.28	-9.17
	A2-R ₁₃	-15.57	-6.46	-5.37	2.79	-9.04
	A4-R ₁₃	-14.46	-6.71	-4.84	2.11	-9.43
	A4-R ₃₃	-14.43	-6.03	-5.11	2.22	-8.91
	A6-R ₁₃	-15.53	-6.82	-5.21	2.73	-9.30
	A6-R ₂₃	-14.19	-6.24	-5.09	2.73	-8.60
	A6-R ₃₃	-14.92	-6.22	-5.21	2.65	-8.78
II	A1-L ₂₁	-13.53	-6.12	-4.86	3.72	-7.26
	A1-L ₃₁	-14.34	-6.81	-4.98	3.66	-8.13
	A3-L ₂₁	-13.73	-6.09	-5.12	3.68	-7.53
	A3-L ₃₁	-14.18	-6.60	-4.98	3.18	-8.40
	A5-L ₂₁	-13.42	-5.60	-5.05	3.29	-7.36
	A5-L ₃₁	-14.20	-6.51	-5.03	3.35	-8.19
	A7-L ₂₁	-13.76	-6.44	-5.02	3.98	-7.48
	A7-L ₃₁	-14.52	-7.12	-5.05	3.75	-8.41
	A1-L ₃₃	-14.21	-6.61	-4.99	3.65	-7.96
	A3-L ₂₃	-13.76	-6.01	-5.20	3.58	-7.63
	A3-L ₃₃	-14.14	-6.42	-5.05	3.21	-8.26
	A5-L ₂₃	-13.47	-5.82	-5.05	3.49	-7.39
	A5-L ₃₃	-18.08	-6.50	-5.20	3.62	-8.08
A7-L ₂₃	-13.67	-6.36	-5.01	3.79	-7.59	
A7-L ₃₃	-14.43	-6.90	-5.06	3.73	-8.24	
III	A3-B ₃₃	-7.19	-5.78	-0.96	0.97	-5.78
	A7-B ₁₁	-6.06	-5.07	-0.52	.84	-4.75

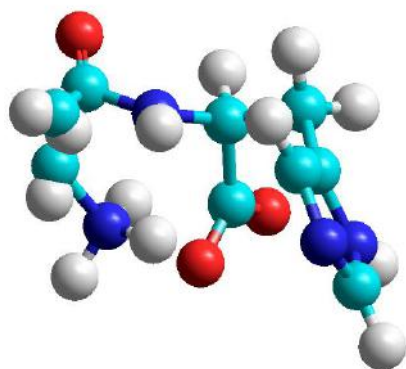
Table 4.

Energy parameters (in kcal/mol) of the favorable conformations for N³H tautomer of carnosine

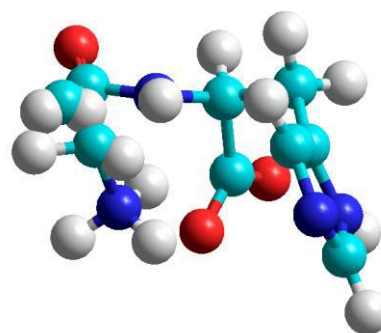
Type	Conformation of molecule	Energy interaction of β -Ala and L-His	E _{nonval.}	E _{elst.}	E _{tors.}	E _{tot.}
I	A2-R ₁₁	-15.15	-5.92	-5.09	2.60	-8.41
	A4-R ₁₁	-14.60	-6.48	-4.77	2.27	-8.99
	A4-R ₂₁	-14.05	-5.74	-5.05	2.34	-8.46
	A4-R ₃₁	-14.87	-5.74	-5.22	2.23	-8.74
	A6-R ₁₁	-15.04	-6.30	-5.05	2.77	-8.58
	A6-R ₃₁	-14.91	-5.89	-5.19	2.58	-8.50
	A8-R ₁₁	-14.94	-6.09	-4.85	2.35	-8.59
	A2-R ₁₃	-15.07	-5.95	-5.30	2.49	-8.76
	A4-R ₁₃	-14.70	-6.45	-5.12	2.26	-9.32
	A4-R ₂₃	-14.61	-5.61	-5.01	2.15	-8.47
	A6-R ₁₃	-15.28	-6.44	-5.29	2.61	-9.13
	A6-R ₂₃	-14.60	-5.73	-5.05	2.69	-8.09
	A6-R ₃₃	-14.94	-6.06	-5.16	2.67	-8.54
	A8-R ₁₃	-15.00	-6.00	-5.31	2.52	-8.80
II	A1-L ₃₁	-14.22	-6.29	-4.88	3.60	-7.57
	A3-L ₂₁	-13.79	-5.88	-5.16	3.70	-7.33
	A3-L ₃₁	-14.15	-6.10	-4.96	3.19	-7.88
	A5-L ₃₁	-14.35	-6.22	-5.09	3.63	-7.68
	A7-L ₂₁	-13.88	-6.08	-5.13	3.84	-7.38
	A7-L ₃₁	-14.44	-6.52	-5.05	3.70	-7.87
	A1-L ₃₃	-14.22	-6.40	-4.94	3.64	-7.71
	A3-L ₂₃	-13.81	-5.83	-5.13	3.70	-7.26
	A3-L ₃₃	-14.05	-6.19	-4.93	3.12	-8.00
	A5-L ₂₃	-13.77	-5.48	-5.19	3.56	-7.11
	A5-L ₃₃	-14.56	-6.27	-5.26	3.71	-7.82
	A7-L ₂₃	-13.88	-6.13	-5.05	3.97	-7.21
	A7-L ₃₃	-14.42	-6.67	-5.02	3.69	-7.99
III	A3-B ₃₁	-7.13	-5.65	-0.65	0.98	-5.32
	A1-B ₁₃	-6.83	-4.80	-0.86	.72	-4.93

Each conformational type for both tautomers of carnosine includes two characteristic conformations which are defined by the same arrangement of the functional groups in space, but differ from each other only by the geometry of β -alanyl fragment (Fig.5 and

6). The dihedral angles of these conformations for N¹H and N³H tautomers of carnosine are represented in the Tables 5 and 6, respectively.



Conformation A4-R₁₁



Conformation A8-R₁₁

(a)

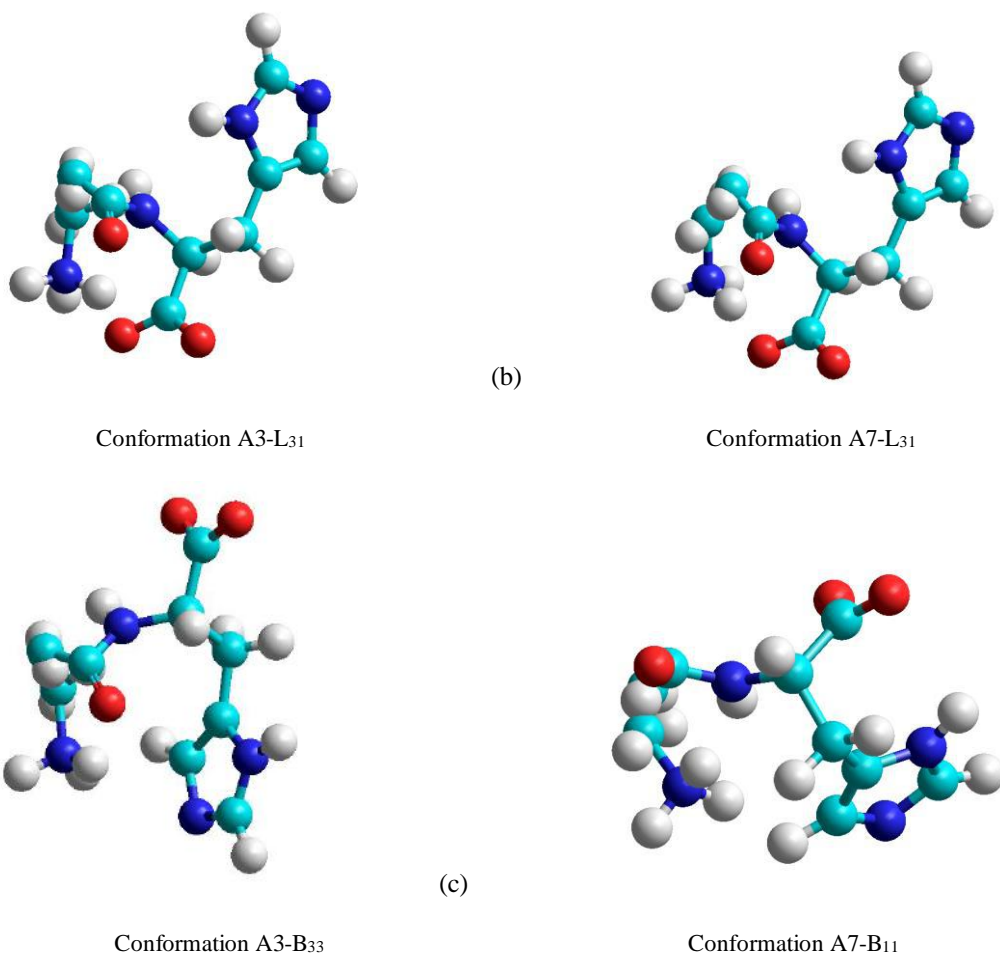
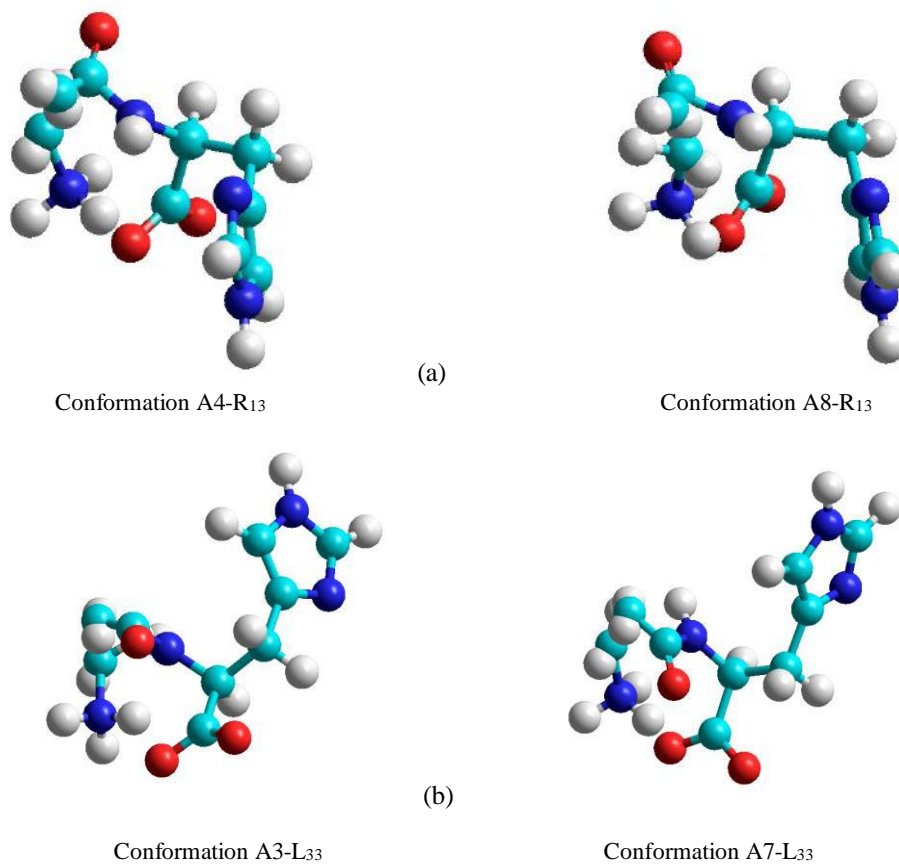


Fig.5. The characteristic conformations of I type (a), II type (b) and III type (c) for N¹H tautomer of carnosine.



SPATIAL STRUCTURE OF N¹H AND N³H TAUTOMERS OF CARNOSINE IN ZWITTERION FORM

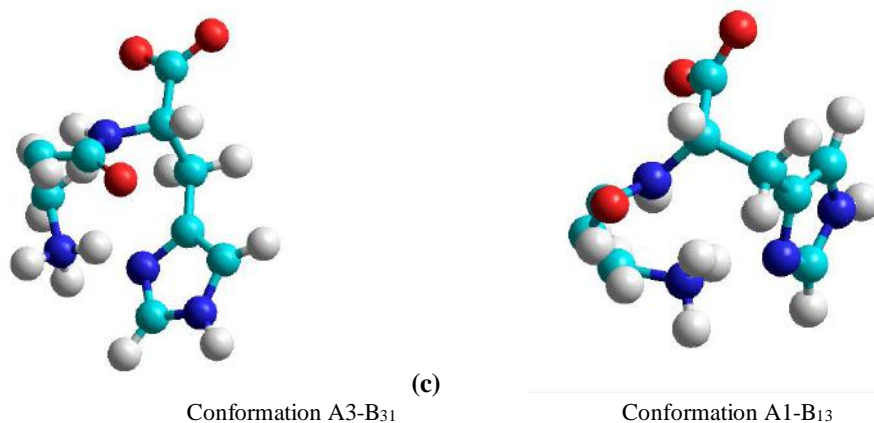


Fig.6. The characteristic conformations of I type (a), II type (b) and III type (c) for N³H tautomer of carnosine.

Table 5.
The geometry parameters (in degrees) of the characteristic conformations for N¹H tautomer of carnosine

Amino-acid residue	Dihedral angles	Conformations					
		I type		II type		III type	
		A4-R ₁₁	A8-R ₁₁	A3-L ₃₁	A7-L ₃₁	A3-B ₃₃	A7-B ₁₁
β-Ala	τ ₁	-64.9	64.3	61.9	-61.7	-56.7	62.7
	τ ₂	56.6	-45.8	-50.1	44.7	61.4	-57.7
	τ ₃	-83.0	-50.6	92.4	60.0	93.1	92.1
	ω	167.0	169.6	-161.0	-164.0	179.8	-176.9
L-His	φ	-88.2	-75.9	50.5	48.4	-136.1	-118.6
	χ ₁	62.6	61.9	-51.7	-54.9	-58.0	64.0
	χ ₂	84.8	81.0	88.6	85.2	-86.6	85.4
	ψ	-27.8	-25.4	51.3	47.4	141.9	165.2

Table 6.
The geometry parameters (in degrees) of the characteristic conformations for N³H tautomer of carnosine

Amino-acid residue	Dihedral angles	Conformations					
		I type		II type		III type	
		A4-R ₁₃	A8-R ₁₃	A3-L ₃₃	A7-L ₃₃	A3-B ₃₁	A1-B ₁₃
β-Ala	τ ₁	-64.1	64.8	-61.7	62.0	-55.9	-46.7
	τ ₂	56.6	-45.6	45.1	-49.0	61.3	-60.8
	τ ₃	-82.3	-51.1	59.9	92.1	93.6	88.7
	ω	166.1	168.1	-164.3	-161.3	-177.9	-177.7
L-His	φ	-91.0	-78.1	48.6	49.8	-135.3	-130.0
	χ ₁	63.3	65.2	-55.3	-52.4	-58.0	60.4
	χ ₂	-96.2	-101.6	-95.0	-91.5	92.4	-92.8
	ψ	-26.4	-25.3	46.9	51.0	142.2	166.0

The effects of intramolecular hydrogen bonding on geometry of molecule were observed in the investigated carnosine tautomers. In dependence on the arrangement of the functional groups the following hydrogen bonds appear in the stable conformations of the molecule. Since the conformations of I type for both carnosine tautomers are characterized by close positions of COO⁻ group, H₃N⁺ group and imidazole ring of L-His in space, therefore two types of the hydrogen bond form in the most stable conformations A4-R₁₁ for N¹H tautomer and A4-R₁₃ for N³H tautomer: 1) between the nearest oxygen and hydrogen atoms of the N- and C-terminal charged groups, 2) between the hydrogen atom of amid group of backbone of L-His and oxygen atoms of COO⁻ group.

In other characteristic conformations of I type only first type of hydrogen bond forms for both tautomers. In the conformations of II type groups COO⁻ and H₃N⁺ are closely spaced, but the imidazole ring of L-His is turned away for both carnosine tautomers. Therefore the most stable conformation A3-L₃₁ of II type for N¹H tautomer is characterized by formation of two types of the hydrogen bond: 1) between the nearest oxygen and hydrogen atoms of N- and C-terminal charged groups, 2) between the oxygen atom of the carbonyl group of β-Ala backbone and H atom, attached to N¹ atom of the imidazole ring of L-His. But in the characteristic conformation A7-L₃₁ of II type for N¹H tautomer and in the characteristic conformations A3-L₃₃ and A7-L₃₃ of II type for N³H

tautomer only first type of the hydrogen bond forms. Since in the conformations of III type H_3N^+ group and imidazole ring of L-His are closely spaced, but COO^- group is turned away for both carnosine tautomers, therefore the characteristic conformations A3-B₃₃ for N¹H tautomer and A3-B₃₁ for N³H tautomer of mentioned type are characterized by formation only one type hydrogen bond between the hydrogen atom

of H_3N^+ group and oxygen atom of the carbonyl group of β -Ala backbone. There are no hydrogen bonds in other characteristic conformations of III type for both tautomers. The energy and geometry parameters of the hydrogen bonds in the characteristic conformations for N¹H and N³H tautomers of carnosine are given in Tables 7 and 8, respectively.

Table 7.

The length (in Å) and energy (shown in brackets, in kcal/mol) of the hydrogen bonds in the characteristic conformations for N¹H tautomer of carnosine

H-bond	I type		II type		III type	
	A4-R ₁₁	A8-R ₁₁	A3-L ₃₁	A7-L ₃₁	A3-B ₃₃	A7-B ₁₁
NH ₃ ⁺ ... OOC	1.95 (-1.30)	1.89 (-1.41)	1.90 (-1.41)	1.92 (-1.36)		
L-His NH... OOC	2.90 (-0.11)					
β -Ala CO...HN ¹ L-His			2.90 (-0.11)			
NH ₃ ⁺ ...OC β -Ala					2.58 (-0.28)	

Table 8.

The length (in Å) and energy (shown in brackets, in kcal/mol) of the hydrogen bonds in the characteristic conformations for N³H tautomer of carnosine

H-bond	I type		II type		III type	
	A4-R ₁₃	A8-R ₁₃	A3-L ₃₃	A7-L ₃₃	A3-B ₃₁	A1-B ₁₃
NH ₃ ⁺ ... OOC	1.92 (-1.36)	1.86 (-1.46)	1.93 (-1.34)	1.89 (-1.41)		
L-His NH... OOC	2.86 (-0.12)					
NH ₃ ⁺ ...OC β -Ala					2.56 (-0.29)	

The interatomic distances between the nitrogen atom of α -amino group and oxygen atoms of deprotonated carboxyl group is 2.9Å in the most stable conformations of I and II type for both carnosine tautomers, that confirms the formation of the salt bridge in them. In the characteristic conformations of III type the value of this distance varies in the interval 6.4–7.2Å.

The obtained results allow us to better describe the structure-functional interrelation of carnosine.

4. CONCLUSION

The energy and geometry parameters characterizing the stable states for N¹H and N³H

tautomers of carnosine in zwitterion form are obtained by method of molecular mechanics. The effects of intramolecular hydrogen bond on geometry of carnosine molecule are observed in the investigated carnosine tautomers. As seen from the obtained results the angles involved in β -alanyl fragment are more mobile than in the other segment of the molecule, therefore it may bend α -amino group toward deprotonated carboxyl group or imidazole ring of L-histidine. It was shown that the most stable conformations for both tautomers of carnosine are characterized by close positions of the functional groups of molecule in space.

- [1] A.A. Boldyrev, G. Aldini, and W. Derave. Physiology and pathophysiology of carnosine, *Physiol.Rev.*, 93(2013)1803-1845. PMID: 24137022, doi:10.1152/physrev.00039.2012.
- [2] P. Nioche, V. Berka, J. Vipond, N. Minton, A.L.Tsai, C.S.Raman. Femtomolar sensitivity of a NO sensor from *Clostridium botulinum*, *Science*, 306 (2004)1550-1553. PMID: 15472039, doi: 10.1126/science.1103596.
- [3] E.J. Baran. Metal complexes of carnosine. *Biochemistry (Mosc)*, 65(2000)789-797. <https://pubmed.ncbi.nlm.nih.gov/10951097/>
- [4] A. Torreggiani, A. Trincherro, M. Tamba, G. Fini. Vibrational characterization and biological activity of carnosine and its metal complexes. *Ital J.Biochem.*, 52(2003)87-97. <https://pubmed.ncbi.nlm.nih.gov/14677425/>
- [5] I. Georgieva, N. Trendafilova, G. Bauer. Spectroscopic and theoretical study of Cu(II), Zn(II), Ni(II), Co(II) and Cd(II) complexes of glyoxilic acid oxime. *Spectrochim Acta A Mol Biomol Spectrosc.*, 63(2006) 403-415. PMID: 15982923, doi: 10.1016/j.saa.2005.05.027.
- [6] S.A. Klyuev. Carnosine conformers. *Biophysics*, 51(2006) 599-602. <https://doi.org/10.1134/S0006350906040130>

- [7] *J. Neu, C.A. Schmuttenmaer.* Terahertz spectroscopy and density functional theory investigation of the dipeptide L-carnosine. *J Infrared Milli Terahz Waves*, 41 (2020) 1366–1377 <https://doi.org/10.1007/s10762-019-00636-7>
- [8] *N.M. Godjajev, S. Akyuz, G.A. Akverdieva.* A molecular mechanics conformational study of peptide T, *J.Mol.Structure*, 403 (1997) 95-110. [https://doi.org/10.1016/S0022-2860\(96\)09410-0](https://doi.org/10.1016/S0022-2860(96)09410-0)
- [9] *R.A. Scott and H.A. Sheraga.* Conformational Analysis of Macromolecules. III. Helical Structures of Polyglycine and Poly-L-Alanine, *J.Chem.Phys.* 45 (1966) 2091. <https://doi.org/10.1063/1.1727894>
- [10] *G.M. Lipkind, S.F. Archipova, E.M. Popov.* Theoretical investigation of the conformations of N-acetyl-L-alanine methylamide in various media, *J.Struct.Chem.*, 11 (1970) 106-110. <https://doi.org/10.1007/BF00743915>
- [11] *F. Momany, R. Mcguire, A. Burgess and H.A. Sheraga.* Energy parameters in polypeptides. VII. Geometric parameters, partial atomic charges, nonbonded interactions, hydrogen bond interactions, and intrinsic torsional potentials for the naturally occurring amino-acids, *J.Phys.Chem.*,79(1975)2361-2381. <https://doi.org/10.1021/j100589a006>
- [12] *N.M. Godjajev, I.S. Maksumov, L.I. Ismailova.* Program of semiempirical calculations of conformations of molecular complexes, *Zh.strukt.khim*, 4(1983) 147-148 (in Russian)
- [13] *G.A. Akverdieva, N.M. Godjajev.* Improvement of program of calculation of molecular conformation, *J. Modern Technology & Engineering*, 2(2017)140-145. <http://jomardpublishing.com/UploadFiles/Files/journals/JTME/V2N2/HakverdiyevaG.pdf>
- [14] *J. Hermans and D. Ferro.* Representation of a protein molecule as a tree and application to modular computer programs which calculate and modify atomic coordinates, *Biopolymers*, 10(1971)1121-1129. <https://doi.org/10.1002/bip.360100704>
- [15] IUPAC-IUB. Quantities, Units and Symbols in Physical Chemistry, Blackwell Scientific, Oxford (1993)168. https://old.iupac.org/publications/books/gbook/green_book_2ed.pdf

Received: 04.05.2021

SURFACE PLASMON POLARITON OBSERVATION AT NARROW-GAP SEMICONDUCTOR Bi_2Se_3 AND Sb_2Te_3

ELVIN HUSENAGA ALIZADE

Institute of Physics, of Azerbaijan NAS

131, H. Javid ave., Baku, AZ 1143,

E-mail: alizadeelv@gmail.com

The application of the surface plasmon resonance (SPR) in the mid IR spectrum is able to recognize a wide range of compounds based on selective binding and vibration modes. This paper presents the results of investigation of the bulk or volume plasmon polariton (VPP) and surface plasmon polaritons (SPP) in the IR spectrum on the well-known layered compounds Bi_2Se_3 and Sb_2Te_3 . The plasmon in the mid-IR spectrum was studied at IR spectroscopic ellipsometry. The dispersion of the plasmon polariton was calculated in case of ambient air medium. Also, the dispersion of the plasmon polariton was calculated in 3 different mediums – KRS-5, ZnSe and Si. Furthermore, the spectral dependence of the plasmon propagation length were calculated.

Keywords: plasmon, surface plasmon resonance, spectroscopic ellipsometry, plasmon dispersion.

PACS: 71.45.Gm

1. INTRODUCTION

For several years, the SPR effect in the noble metals has been actively applied for sensing compound [1] [2] [3] [4]. SPR is the result of collective oscillations of free carriers at the metal-dielectric interface. SPR is a promising tool to perform rapid tests for a wide range of applications to monitor environmental changes and chemical composition. Increasing the sensitivity and expanding the possible application has become a necessity, thus, the task of finding new materials in addition to noble metals has become extremely important. Narrow-gap degenerate semiconductors with a high concentration of free carriers are very interesting for plasmonic applications in the IR spectrum.

Most of the work on the observation and application of the plasmon phenomenon was done in the visible region. The several methods were used for plasmon coupling. The most common method of coupling is with a prism, so called Kretschmann configuration. The projection onto the surface of the wavenumber in a cylindrical prism takes the form $k_x = \frac{\omega}{c} \sqrt{\varepsilon_a} \sin(\theta)$ [4]. The necessary condition to excite the plasmon is when $k_x = k_{spp}$, where k_{spp} –the real part of SPP wavenumber. The choice of material in the visible region of the spectrum is limited, for example quartz should have $\varepsilon_a = 3.4$. There are wide range of materials for the IR spectrum, while ε_m for these materials is greater than ε_m for quartz. This makes it possible to operate plasmon in a wide range of the spectrum. In this work, we used the KRS-5 ($\varepsilon_m = 5,66$), ZnSe ($\varepsilon_m = 5,91$) and Si ($\varepsilon_m = 11$) prism to calculate behavior of SPP. It is essential to evaluate the shifts of the plasmon resonance energy in different ambient for further application.

In this paper, for the first time, it is proposed to consider the application of the SPR in the IR spectrum, investigating in Bi_2Se_3 and Sb_2Te_3 . Plasmons in these compounds were previously reported [5] [6], but their use in SPR devices was not proposed.

2. THEORETICAL DETAILS

The model of the interface between the ambient air and plasmonic material is selected for calculation of the dispersion (Fig. 1.).

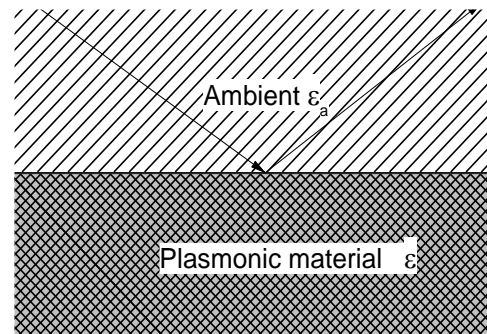


Fig. 1. Schematic representation of the model for calculation.

The calculation was carried out using the data of the dielectric function obtained by spectroscopic ellipsometry according to the equation [3]:

$$k = k_1 + ik_2 = \left[\frac{\omega}{c} \left(\frac{\varepsilon_1 \varepsilon_m}{\varepsilon_1 + \varepsilon_m} \right)^{1/2} \right] + i \left[\frac{\omega}{c} \left(\frac{\varepsilon_1 \varepsilon_m}{\varepsilon_1 + \varepsilon_m} \right)^{3/2} \frac{\varepsilon_2}{2(\varepsilon_1)^2} \right]$$

where k_1 and k_2 –real and imaginary parts of the wave vector, respectively, ω –photon frequency, c –speed of light, ε_1 and ε_2 –real and imaginary parts of the dielectric function, respectively, and ε_m –dielectric function of the medium. The SPP loses energy as it propagates along the surface. This important property of the plasmon characterizes the imaginary part of the wave vector. The distance along the propagation of the SPP at which it decays by $1/e$ is called the propagation length. The propagation length is calculated by the following equation:

$$L_{SPP} = \frac{1}{2k_2}$$

The parameter of the skin-layer thickness is used to assess the penetration depth of the SPP into the depth of the metal. This thickness characterizes the attenuation of the SPP $1/e$ when the SPP penetrates deeply into the metal. Skin thickness is obtained from the equation:

$$\Delta = \sqrt{\frac{2}{\sigma\mu\omega}}$$

Propagation length and skin layer thickness are important parameters in the future study of localized SPP and for plasmon coupling.

3. EXPERIMENTAL DETAILS

This work is a continuation of the study of plasmons in Bi_2Se_3 and Sb_2Te_3 by using spectroscopic ellipsometry, which were reported earlier [5] [6]. The dependence of the dielectric function of the photon energy is extracted by the spectroellipsometric method with the help of the J.A. Woollam IR-Vase ellipsometer. Data on the sample preparation, structure of the samples, some transport properties and spectroscopic ellipsometry experimental results are given in [5]. These data were used in our current calculations.

4. RESULTS AND DISCUSSION

Figures 2a and 2b show the calculation of the plasmon dispersion in air and various prism materials.

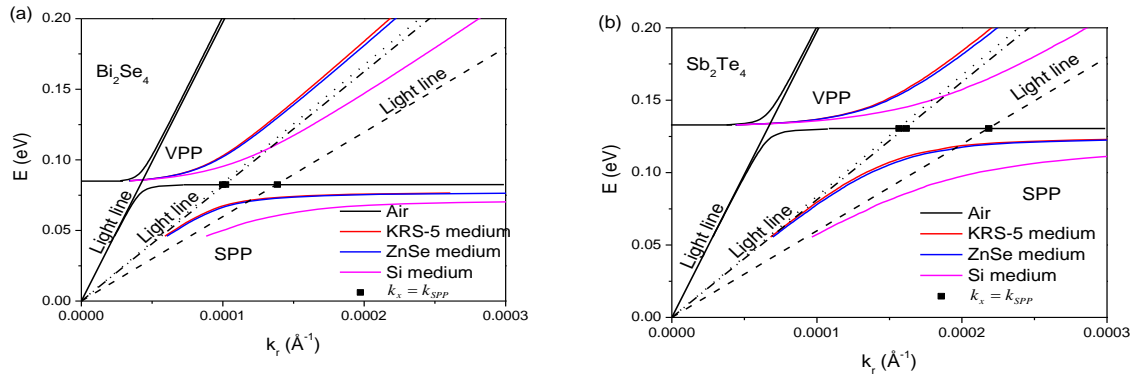


Fig. 2. Plasmon dispersion for Bi_2Se_3 (a) and Sb_2Te_3 (b). Solid line is light line in air case, dotted line in KRS-5 prism case, dash-dot line in ZnSe prism case and dashed line in Si prism case

In the air, the SPR is excited at the photon energy of 0.083 eV for Bi_2Se_3 ; by selecting a prism, it is possible to tune the SPR excitation energy. Thus, in a KRS-5 and ZnSe medium, it will be possible to excite an SPR at a photon energy of 0.075 eV, and in a Si medium at the photon energy of 0.067 eV. Similarly, for Sb_2Te_3 due to the external environment, it is possible to tune the SPR. In the air an SPR is excited at the photon energy of 0.130 eV, in a KRS-5 and ZnSe medium, 0.123 eV, and in the Si medium, the SPR is excited at the photon energy of 0.110 eV. There is a sensitive shift in SPR energies for different prism materials. A device based on the SPR will have the best qualities if the shift of its resonant wavelength $\delta\lambda_{SPR}$ is significant relative to the change in the refractive index of the external medium δn_m . This property is called sensitivity and is defined as [8]

$$S = \frac{\delta\lambda_{SPR}}{\delta n_m}$$

For the most widely investigated material like gold, the sensitivity is 0.82 $\mu\text{m}/\text{RIU}$ (refractive index unit). Table.1 shows the sensitivity values for Bi_2Se_3 and Sb_2Te_3 . The sensitivity for Bi_2Se_3 is highest, and for Sb_2Te_3 it is comparable with the sensitivity of the gold. Fig. 3 shows graphs of the plasmon polariton (PP) propagation length. As can be seen, the plasmon propagation length at resonance frequencies is 0. An increase in the dielectric constant of the environment leads to a significant reduction in the PP propagation length for both the VPP and the SPP.

Resonant wavelength SPP and Sensitivity

Compound	λ_1 Mm	λ_2 μm	λ_3 Mm	$\delta\lambda_1$ Mm	$\delta\lambda_2$ μm	S_2 $\mu\text{m}/\text{RIU}$	S_3 $\mu\text{m}/\text{RIU}$
Bi_2Se_3	14.9	16.5	18.5	1.6	3.6	1.17	1.55
Sb_2Te_3	9.5	10.0	11.3	0.5	1.8	0.40	0.75

Table 1.

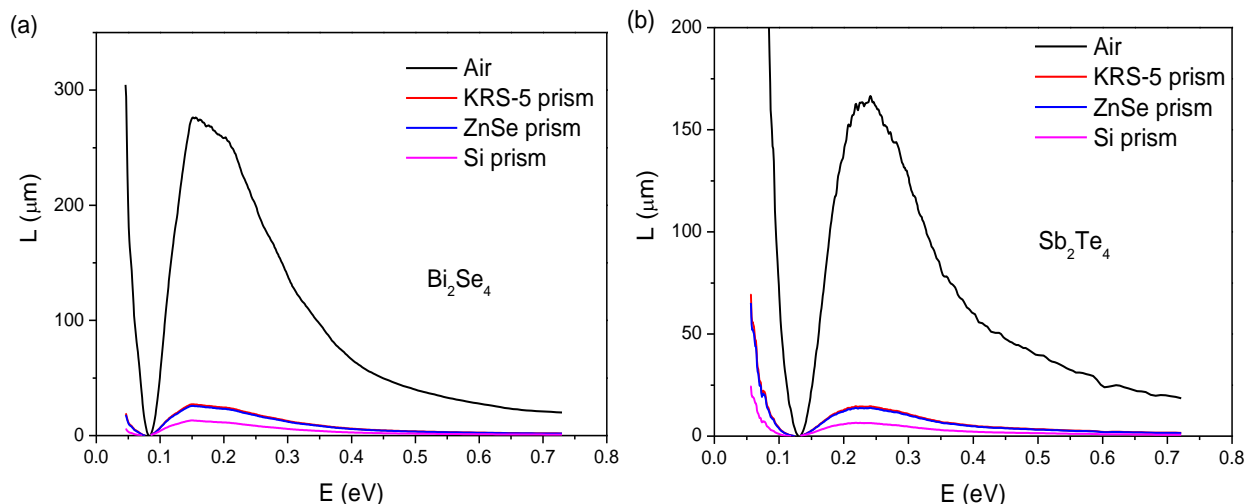


Fig. 3. PP Propagation length (a) Bi_2Se_3 and (b) Sb_2Te_3 .

5. CONCLUSION

The possibility of exciting and controlling the plasmon resonance energy in the Bi_2Se_3 and Sb_2Te_3 structures has been shown for the first time. The presented compounds Bi_2Se_3 and Sb_2Te_3 are promising for use as plasmonic materials in the IR spectrum. The PP dispersion calculated in this paper showed the

possibility for tuning of plasmon coupling in a wide range of the photon energy spectrum. The sensitivity of the plasmons in Bi_2Se_3 and Sb_2Te_3 is comparable to the sensitivity of the plasmons in gold. For some cases in Bi_2Se_3 the sensitivity is 89% and this is higher than that in gold. The calculated plasmon propagation length significantly exceeds the analogous data for gold.

- [1] C. Rhodes, S. Franzen, Jon-Paul Maria, M. Losego, D. N. Leonard, B. Laughlin, G. Duscher and S. Weibel. *J. Appl. Phys.*, 2006, vol. 100, p. 054905.
- [2] Gupta, Rajneesh K. Verma and D. Banshi. "Surface plasmon resonance based fiber optic sensor for the IR region using a conducting metal oxide film," *J. Opt. Soc. Am. A*, 2010, vol. 27, no. 4, pp. 846-851.
- [3] J. Zhang, L. Zhang and W. Xu. "Surface plasmon polaritons: physics and application," *J. Phys. D: Appl. Phys.*, 2012, vol. 45, p. 113001.
- [4] O.S. Wolfbeis. *Springer Series on Chemical Sensors and Biosensors*, Heidelberg: Springer-Verlag Berlin Heidelberg, 2009.
- [5] N.T. Mamedov, E.H. Alizade, Z.A. Jahangirli, Z.S. Aliev, N.A. Abdullayev, S.N. Mammadov, I.R. Amiraslanov, Yong-Gu Shim, Kazuki Wakita, S.S. Ragimov, A. I. Bayramov, M. B. Babanly, A. M. Shikin, and E.V. Chulkov. *J. Vac. Sci. Technol. B*, vol. 37, no. 1, pp. 062602-1, 2019.
- [6] P. Di Pietro, F.M. Vitucci, D. Nicoletti, L. Baldassarre, P. Calvani, R. Cava, Y.S. Hor, U. Schade, and S. Lupi. *PHYS. REV. B*, vol. 86, p. 045439, 2012.
- [7] Z.S. Aliev, E.C. Ahmadov, D.M. Babanly, I.R. Amiraslanov, M.B. Babanly, "The Bi_2Se_3 - Bi_2Te_3 - BiI_3 system: Synthesis and characterization of the $\text{BiTe}_{1-x}\text{Se}_x\text{I}$ solid solutions," *Calphad*, vol. 66, p. 101650, 2019.
- [8] El-Sayed, P.K. Jain and A. Mostafa. "Surface Plasmon Resonance Sensitivity of Metal Nanostructures: Physical Basis and Universal Scaling in Metal Nanoshells," *J. Phys. Chem. C*, vol. 111, p. 47, 2007.

Received: 01.06.2021

STUDY OF THE EFFECT OF IMPURITIES AND HEAT TREATMENTS ON THE STRUCTURE OF Se-As-EuF₃, Se-Te-Sm AND Ge₂Sb₂Te₅ FILMS BY X-RAY DIFFRACTION AND RAMAN SPECTROSCOPY

S.N. GARIBOVA^{1,2}, A.I. ISAYEV¹, S.I. MEKHTIYEVA¹,
S.U. ATAYEVA¹, S.S. BABAYEV¹

¹*G.M. Abdullayev Institute of Physics of Azerbaijan NAS 131, H. Javid ave., Baku, AZ 1143*

²*Department of Physics and Electronics, Khazar University 41, Mehseti str., AZ1096,*

Baku Azerbaijan

sgaribova1@gmail.com

The local structure of film samples of the Se₉₅As₅, Se₉₅Te₅ and Ge₂₀Sb_{20.5}Te₅₁ chalcogenide semiconductors have been studied by X-ray diffraction and Raman spectroscopy. The effect of EuF₃ and Sm impurities on the structure of Se₉₅As₅, Se₉₅Te₅ and the effect of heat treatment at various temperatures on structure of Ge₂₀Sb_{20.5}Te₅₁ thin films have been studied. It was shown that Ge₂₀Sb_{20.5}Te₅₁ films obtained by thermal evaporation of an unheated glass substrate are amorphous, and those that underwent heat treatment at 220 and 400 °C transforms into a crystalline phase with a cubic and hexagonal structure. The chemical bonds and the basic structural elements that form the matrix of the studied materials, as well as the changes that occur in them upon the heat treatment and addition of impurities have been determined.

Keywords: glassy semiconductors, local structure, charged defects, memory effect.

PACS: 78.66.Jg, 72.15.Rn, 61.05.C, 73.20.Hb

1. INTRODUCTION

Interest in chalcogenide glassy semiconductors (CGS) appeared after semiconductor properties were first discovered in these materials, which combined with the properties of the glassy state [1]. CGS promising materials have the ability to change their electrical, photoelectric and optical properties under the influence of light, i.e. change the refractive index of light, the edge of optical absorption. Thanks to which they are widely used as active materials in various electrical switches, storage devices, in infrared (IR) technology and acousto-optical devices.

Switching and memory effects in chalcogenide glassy semiconductors have long been known, but the physics of these effects is still unknown. Recently, interest has increased in the development of non-volatile memory elements based on the chalcogenide glass-crystal phase transition, which allows a reversible phase change between a stable amorphous and crystalline state.

The memory elements based on CGS are called variable phase state or phase memory - Phase Change Memory (PCM), Phase Change Random Access Memory (PRAM) and Ovonyx Unified Memory (OUM). The short recording time and large optical contrast between the amorphous and crystalline states made it possible to use Ge₂Sb₂Te₅ materials to create rewritable CDs, DVDs, and Blu-ray discs, which demonstrated the stability and high speed of phase transitions in the materials of this system [2-4].

This work is devoted to the study of the local structure at the level short-range and medium-range order of binary and triple chalcogenide materials. The CGS systems Se-As and Se-Te doped with EuF₃ and Sm impurities, as well as Ge₂₀Sb_{20.5}Te₅₁ have been chosen as the study objects.

The choice of rare-earth elements as an impurity is due to the fact that, as chemically active elements, they can form new structural elements with selenium atoms, i.e. can lead to a change in the local structure at the level of short-range and medium-range order and thus affect the physical properties. The Ge-Sb-Te triple chalcogenide material, depending on the temperature and the technological regime of sample preparation, can be in amorphous and two crystalline phases - cubic and hexagonal, which should be accompanied by changes in the parameters of short-range and medium-range order. X-ray diffraction and Raman spectroscopy have chosen as the research methods. Such studies make it possible to determine short-range and medium-range order parameters, as well as chemical bonds and structural elements of the matrix of samples in both amorphous and crystalline states and changes depending on the chemical composition and the presence of impurities.

2. EXPERIMENTS AND SAMPLE PREPARATION

Chalcogenide materials Se-As-EuF₃, Se-Te-Sm and Ge-Sb-Te were obtained by fusion of elementary substances of high purity in vacuumized up to 10⁻⁴ Torr quartz ampoules. The synthesis was carried out at a temperature of 900 °C for 10 hours with holding for at least 5 hours in a rotary kiln, followed by cooling in the off-furnace mode. The samples for measurements were films 0.5, 0.75 and 1.5 μm thicknesses and 3–8 μm thickness, obtained by thermal evaporation at a rate of 0.2–0.5 μm/s in vacuum on a glass substrate at a pressure of 10⁻⁴ Torr, as well as bulk samples 1.5 mm thick. X-ray diffraction analysis was performed using a “Bruker” D2Phaser diffractometer and CuKα-rays with a radiation wavelength of λ = 1.5406 · 10⁻¹⁰ m in the angle range 2θ = 5–80°.

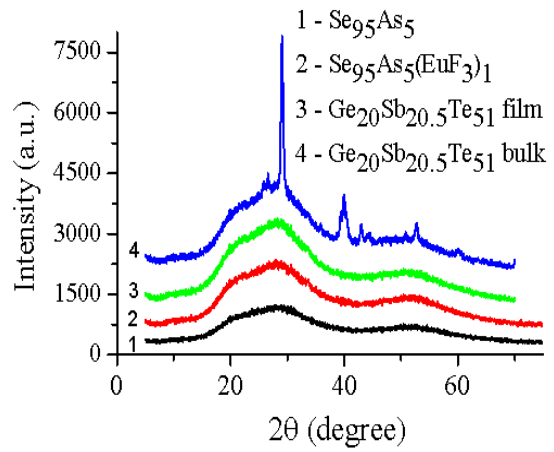
Structural studies and calculations were carried out using the EVA and TOPAZ programs. Raman spectra were studied on a three-dimensional confocal Raman microscope Nanofinder 30 (Tokyo Instr.), the excitation wavelength was 532 nm. The radius of the cross section of the laser beam incident on the film was ~ 4 μm. The radiation receiver was a cooled CCD camera (-70°C) operating in the photon counting mode with exposure time 10–20 s at a laser radiation power of 4 mW, and the spectral resolution error 0.5 cm⁻¹. The experiments were carried out at room temperature, and after heat treatment of the samples at 120, 220, 400 °C for 30 min.

3. EXPERIMENTAL RESULTS AND DISCUSSION

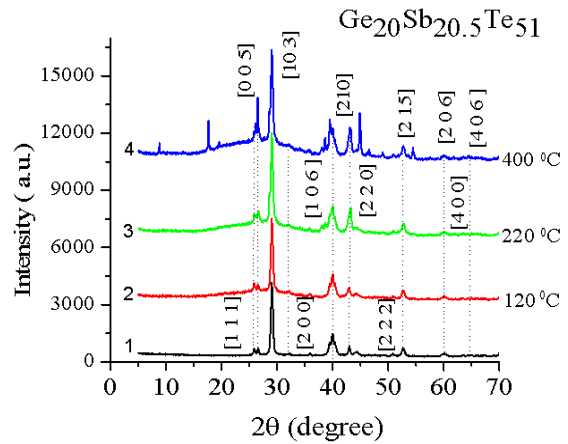
3.1. X-Rays diffraction analysis of the structure Se₉₅As₅<EuF₃> and Ge₂₀Sb_{20.5}Te₅₁ films.

Fig. 1 shows the angular distributions of the X-ray diffraction intensity of the samples Se₉₅As₅<EuF₃> and Ge₂₀Sb_{20.5}Te₅₁ systems. X-ray diffraction patterns (XRD) of the Se₉₅As₅ and Se₉₅As₅(EuF₃)₁ 8 μm, Ge₂₀Sb_{20.5}Te₅₁ 0.5 μm and 1.5 mm thickness samples are presented in Fig.1a. While Fig.1b are XRD patterns of the Ge₂₀Sb_{20.5}Te₅₁ 0.5 - 0.75 μm and 1.5 mm thickness.

As can be seen from the XRD patterns, film samples at room temperature (Fig. 1a, curves 1, 2 and 3) have a broad maximum at 2θ (θ is the Bragg angle) located in the range 15–38 °, which indicates their amorphous. Most CGSs have a similar extent, including Se-Te and Se-Te-Sm. From the XRD patterns of Se-As-EuF₃ and Se-Te-Sm have been determined the “quasiperiod” (R) of the structure of fluctuations in the atomic density [5–7], the repetition of which in a certain region can cause the appearance of the first sharp diffraction peak (FSDP), the length of the correlation (L), in which the frequency fluctuation of the density is preserved, and the diameter of the nanovoids (D) or a region with a reduced atomic density.



a)



b)

Fig.1. XRD patterns of (a) Se₉₅As₅, Se₉₅As₅(EuF₃)₁ and Ge₂₀Sb_{20.5}Te₅₁ chalcogenide samples at room temperature, (b) Ge₂₀Sb_{20.5}Te₅₁ before (curve 1) and after the treatment temperature (curves 2, 3, 4).

The values of the parameters characterizing the structure of the studied films are given in the table 1.

Table 1.

The values of short-range and medium-range orders parameters of Se-As-EuF₃ and Se-Te-Sm film samples.

	R, Å	L, Å	D, Å
Se ₉₅ As ₅	3.177	6.5443	3.654
Se ₉₅ As ₅ +1at%EuF ₃	3.318	6.0349	3.816
Se ₉₅ Te ₅	4.02	12.94	4.63
Se ₉₅ Te ₅ +1at%Sm	3.35	8.16	3.85

The XRD pattern of the Ge-Sb-Te bulk sample 1.5 mm thick (Fig. 1a, curve 4) shows that, before the treatment temperature, the presence of peaks at angles of 25.7 °, 29.7 °, 42.8 ° and 52.9 ° indicates cubic phase of the crystal structure. Figure 1b shows the XRD pattern of the Ge₂₀Sb_{20.5}Te₅₁ samples before (curve 1) and after the treatment temperature (curves 2, 3, 4). XRD pattern of a bulk sample to the

processing temperature (Fig. 1b, curve 1) obtained in the off-furnace mode has certain maxima (reflections) at angles of 25.7° (111), 29.7° (200), 42.8° (220) and 52.9° (222), which corresponds to reflections of the first and second order in the metastable face-centered cubic (FCC) phase along the (111) direction [8, 9]. At a temperature of 120°C, the peaks in the film sample (curve 2 of Fig. 1b) remain almost unchanged, but

peaks appearing in the films (curves 3, 4 of Fig. 1b) indicate crystallization. At a temperature of 220°C, the intensities of these peaks increase and new ones appear at 29.7° (103), 40.1° (106), 42.8° (210), 60.1° (206), 63.6° (400), the intensities of which also increase with a further increase in processing temperature (up to 400 °C). The positions of the fixed peaks correspond to the results of [8–10] and indicate the origin of structural changes in the sample at the stable hexagonal phase (HEX - phase structure).

The materials of the Ge-Sb-Te system have a low glass-forming ability and are easy to crystallize, and to obtain such a material in an amorphous state, it is necessary to cool the melt in a few tens or hundreds of nanoseconds. It is the high crystallization rate that allows in modern memory cells to record information in less than 50 ns. However, with decreasing temperature, the crystallization time increases exponentially and is about 100 years at room temperature [11]. Therefore, the materials of the Ge-Sb-Te system are successfully used in modern storage media.

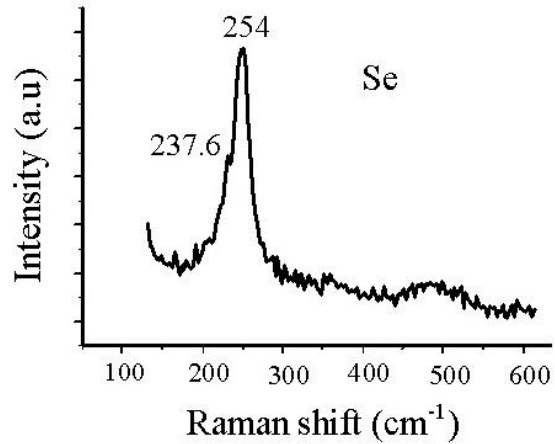
The analysis of Ge₂₀Sb_{20.5}Te₅₁ XRD patterns indicates that the film samples are amorphous to the processing temperature, while the bulk sample has a crystalline structure, in particular a cubic one. After the treatment temperature (at 120°C), the film structures crystallize, partially transforming into a cubic structure. With a further increase in temperature to 220 °C, peaks appear in the structure of the films, indicating a hexagonal phase. At 400 °C the Ge₂₀Sb_{20.5}Te₅₁ film sample transfers to the stable hexagonal phase.

3.2. Raman scattering of Se₉₅As₅<EuF₃>, Se₉₅Te₅<Sm> and Ge₂₀Sb_{20.5}Te₅₁ amorphous and crystalline films.

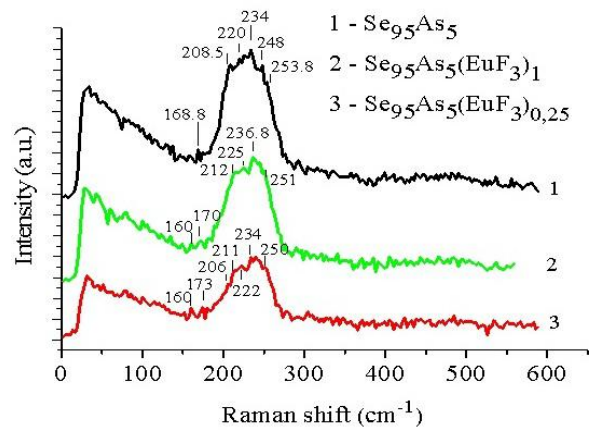
Fig. 2 shows the Raman scattering in films 3-8 μm thickness of amorphous selenium (Fig. 2a) and Se₉₅As₅(EuF₃)_x (x = 0; 0.5; 1 at%) (Fig. 2b). It can be seen that the spectrum of amorphous selenium consists of a broad maximum at a frequency of 254 cm⁻¹ and a narrow maximum at 237.6 cm⁻¹, which correspond to vibrations of ring Se₈ and chain –Se – Se– molecules [12, 13]. With the addition of arsenic to selenium, the maximum at 254 cm⁻¹ weakens and peaks appear in the frequency range 209–220 cm⁻¹, which is partially due to the destruction of ring molecules and the formation of an As₄Se₄ type molecular fragment. In addition, a peak appears at 225cm⁻¹ and is attributed to AsSe₃ structural elements [12, 14].

The weak maximum at 170 cm⁻¹ observed in all spectra shown in Fig. 2b, is attributed to vibrations of the As – As homeopolar bond [15]. The introduction of the EuF₃ impurity leads to the appearance of narrow peaks in the Raman spectrum of Se₉₅As₅ films, which is associated with the formation of new structural elements with the participation of europium atoms. Since europium atoms as a chemically active element form chemical bonds with selenium atoms. In this case, the peak at 254 cm⁻¹ is strongly attenuated,

which is due to the fact that the participation of europium atoms leads to a more efficient destruction of ring selenium molecules. In addition, it is assumed that europium atoms lead to the crosslinking of the ends of the polymer chains into a pyramidal structure and the peaks at frequencies of 220.7 cm⁻¹, 211 cm⁻¹ and 160.4 cm⁻¹ are associated with vibrations of the EuSe₃, EuSe_{3/2} pyramidal structural elements and Eu – Se bonds, respectively.



(a)



(b)

Fig.2. Raman spectra of (a) Se and (b) Se-As, Se-As-EuF₃ amorphous film samples.

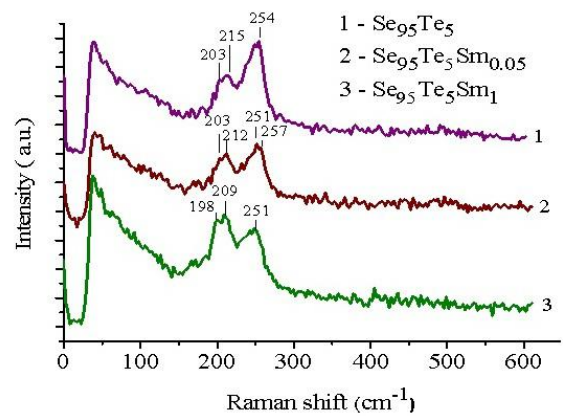
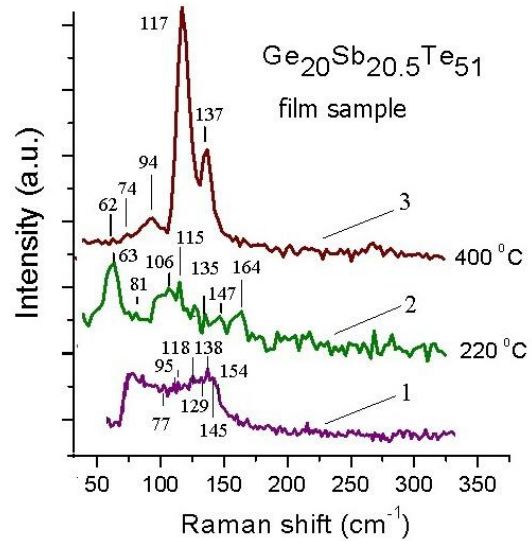


Fig.3. Raman spectra of Se-Te and Se-Te-Sm amorphous film samples.

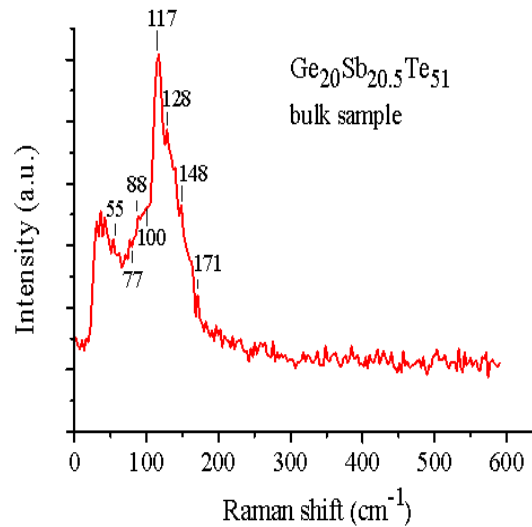
The Raman spectrum of amorphous $\text{Se}_{95}\text{Te}_5$ doped with samarium is shown in Fig. 3. Peaks at 211.7 and 253.3 cm^{-1} are observed in the $\text{Se}_{95}\text{Te}_5\text{CGS}$ composition. As already noted, the peak at 253.3 cm^{-1} belongs to ring selenium molecules, and the peak at 211.7 cm^{-1} , according to [16], corresponds to vibrations of the Se – Te bond. It is known that amorphous selenium consists of long polymer chains and eight-membered rings, inside of which covalent bonds exist between atoms, and between various structural elements the van-der-Waals bonds [17]. The addition of tellurium to amorphous selenium leads to partial destruction of ring molecules and shortening of polymer chains. As a result, the number of Se – Se bonds decreases, and Se – Te bonds are formed, accompanied by the appearance of a band of 211.7 cm^{-1} corresponding to the indicated bonds. As can be seen from the figure, doping with samarium changes the shape and intensity of the peaks in the Raman spectrum. In this case, a decrease in the intensity of the band peak at 254 cm^{-1} and an increase in the band peak at 211.7 cm^{-1} , as well as a slight expansion of the latter toward the low-frequency side of the spectrum, are observed. The latter, apparently, is associated with the chemical activity of samarium atoms, which form bonds with both selenium and tellurium (Sm – Se, Sm – Te, Se – Sm – Te), as well as pyramidal structural elements involving samarium atoms ($\text{SmSe}_x\text{Te}_{3-x}$). The frequencies of the vibrational modes corresponding to the indicated bands are close to each other and overlapping form bands.

Fig. 4a shows the Raman spectrum of a bulk 1.5 mm thick and Fig. 4b film $0.5\text{--}0.75\text{ }\mu\text{m}$ thickness samples of $\text{Ge}_{20}\text{Sb}_{20.5}\text{Te}_{51}$ obtained at room temperature (Fig. 4b curve 1) and subjected to heat treatment at $220\text{ }^\circ\text{C}$ (curve 2) and $400\text{ }^\circ\text{C}$ (curve 3). The spectrum of films at room temperature consists of a wide band covering the frequency range $75\text{--}175\text{ cm}^{-1}$ with weak maxima at $95, 105, 118, 129, 147,$ and 160 cm^{-1} (Fig. 4b, curve 2). The maxima at $160, 149, 129\text{ cm}^{-1}$, with some deviations, were observed in the Raman spectrum of bulk sample (Fig. 4a) and films obtained at room temperature and heat-treated at $220\text{ }^\circ\text{C}$ (Fig. 4b, curve 1, 2), and maximums at $115\text{--}117\text{ cm}^{-1}, 74\text{--}90\text{ cm}^{-1}$ in the spectrum of all samples. A number of works [18–25] are devoted to studying the features of the Raman scattering spectrum of amorphous and crystalline $\text{Ge}_2\text{Sb}_2\text{Te}_5$ samples. The authors of [18, 22] attributed the 160 cm^{-1} peak to vibrations of defective octahedral structural elements based on Ge. The authors of [22] calculated the Raman spectrum of amorphous and cubic crystals of the $\text{Ge}_2\text{Sb}_2\text{Te}_5$ structure using *ab initio* phonon methods and an empirical model of bond polarizability. They concluded that the observed features of both amorphous and crystalline $\text{Ge}_2\text{Sb}_2\text{Te}_5$ can be attributed to vibrations of defective octahedra. The signs of tetrahedra in the Raman scattering spectrum of amorphous samples are covered by a large cross section of the Raman scattering of defective octahedra. The authors of [19] attributed this peak to vibrations of the Sb – Sb homeopolar bond,

and the authors of [20] to the crystallization of the samples. The authors [22, 24–25] associated the maximum at 160 cm^{-1} with activation of the A_{1g} vibrational modes and their appearance was considered a sign of the formation of crystalline structural elements.



(a)



(b)

Fig.4. Raman spectra of (a) Ge-Sb-Te bulk sample before and (b) Ge-Sb-Te film samples after the processing temperature.

The band localized at $\sim 150\text{ cm}^{-1}$ (in our studies at $\sim 147\text{ cm}^{-1}$) is directly related to the Sb_2Te_3 and partially to the pyramidal SbTe_3 structural element [18]. The band with maxima of $\sim 145\text{--}150\text{ cm}^{-1}$ was attributed by other researchers to vibrations of the Sb – Te bond in the SbTe_3 pyramidal structural element [25] or in octahedrally coordinated Sb atoms [22]. A wide band at 150 cm^{-1} was also observed in [26] and associated with vibrations of the Te – Te homeopolar bond. The authors of this work noted that this band is observed only in samples subjected to low-

temperature annealing. A peak at 150 cm⁻¹ of the corresponding Te – Te bond extension modes have not observed in the Raman spectrum of bulk Ge₂Sb₂Te₅ samples [20], which has considered a sign of good crystallization of bulk samples.

Peaks at frequencies of ~127–129 cm⁻¹ in the Raman spectrum have been observed in all Ge₂Sb₂Te₅ samples except for the film, which is subjected to heat treatment at 400 °C. The position of this peak is very close to the maximum at 125 cm⁻¹ observed in [18], which the author of [27], taking into account the results of Raman scattering studies in a-GeTe thin films [28], attributed the A₁ mode of the GeTe_{4-n}Ge_n composition (n = 1, 2) - corner-sharing tetrahedra. The existence of tetrahedral units of GeTe_{4-n}Ge_n (n = 1, 2), including Ge-Ge homeopolar bonds, was also reported in [29] as the results of the EXAFS study. Tetrahedral structural elements are inherent in binary chalcogenides of the GeSe₂ and GeS₂ type [30, 31].

As can be seen from Fig. 4 peak at 115 – 118 cm⁻¹ is very weakly observed in the Raman spectrum of films (Fig. 4b) obtained at room temperature (curve 1), become pronounced after heat treatment at 220 °C (curve 2) and strongly amplifies after thermal processing at 400 °C (curve 3). The indicated peak will also be observed rather intensively in bulk sample (Fig. 4a). The indicated peak was also observed at ~115 cm⁻¹ in [20], and the peak at 120 cm⁻¹ in [21, 22, 24, 32] and was attributed to the vibration of defective octahedra.

Weak peaks in the frequency range 74– 90 cm⁻¹ observed in the Raman spectrum of all samples were also observed by the authors of [27, 34–35.] and the authors of [27], taking into account the results of studies presented in [33], were connected by the E mode of the GeTe₄ tetrahedron.

In the samples that underwent heat treatment at 220 °C, the peaks at ~127– 129 cm⁻¹ and ~145– 150 cm⁻¹ are attenuated and peaks appear at ~105– 106 cm⁻¹ and ~135 – 137 cm⁻¹ of vibrational modes for crystalline phases cubic structure (FCC configuration - Fig. 1b). According to the authors of [9], the first peak can be attributed to vibrations of A₁ mode of corner-sharing GeTe₄ tetrahedra and the second to GeTe_{4-n}Ge_n (n = 1, 2) tetrahedra. In the samples that underwent heat treatment at 400°C, these peaks disappear and low-frequency peaks remain and pronounced peaks appear at 117 and 137 cm⁻¹, i.e. crystalline phases with a hexagonal structure are formed (HEX configuration - Fig. 1b).

From the above interpretation of the results of studying the Raman spectrum of Ge₂₀Sb_{20.5}Te₅₁ samples obtained by various methods (by thermal

evaporation and cooling of the alloy), as well as crystallized by heat treatment, it follows that their positions of several peaks coincide. This coincidence of the peaks in the Raman spectrum for various samples indicates the coincidence of the short-range order in the arrangement of atoms in them.

4. CONCLUSION

Using X-ray diffraction and Raman spectroscopy, the short-range and medium-range order features in the atoms arrangement of the Se₉₅As₅<EuF₃>, Se₉₅Te₅ <Sm> and Ge₂₀Sb_{20.5}Te₅₁ chalcogenide materials have been studied. In particular, the correlation length in the atoms arrangement, the “quasiperiod” of fluctuations in the atoms density on the scale of the correlation length, chemical bonds and the main structural elements that form the matrix of the studied materials have been determined.

It was established that the technological mode of sample preparation (melt cooling, thermal evaporation in vacuum) and heat treatment significantly affect the structure of Ge₂₀Sb_{20.5}Te₅₁. Film samples of Ge₂₀Sb_{20.5}Te₅₁ obtained by thermal evaporation on an unheated glass substrate are amorphous, heat-treated at 220 and 400 °C pass into the crystalline phase with a cubic (FCC) and hexagonal (HEX) structure, and samples obtained by cooling the melt are partially crystallized.

The chemical bonds and the main structural elements that form the matrix of the studied objects, also the changes that occur in them with the heat treatment and addition of impurities have been determined. It was shown that the main structural elements of bulk sample and films obtained by thermal evaporation on an unheated glass substrate and thermally processed at 220 °C are the defective octahedra, GeTe_{4-n}Ge_n (n = 1, 2) corner-sharing tetrahedral, the Sb₂Te₃ structural and the SbTe₃ pyramidal structural element.

ACKNOWLEDGMENTS

The authors are grateful to S.S. Babayev, I.R. Amiraslanov and the late E.R. Aliyeva for the help provided during the experiments.

FINANCING

The work was carried out in the Innovation sector of the G.M. Abdullayev Institute of Physics of Azerbaijan NAS.

-
- [1] B.T. Kolomies, N.A. Qoryunova. 1955. Tech. Phy. Letter, 25 (6), 984 [in Russian].
- [2] M. Wuttig, N. Yamada. 2007. Nature Mater., 6, 824.
- [3] W. Welnic, M. Wuttig, 2008. Materials Today, 11 (6), 20.
- [4] D. Lencer, M. Salinga, M. Wuttig. 2011. Adv. Mater., 23, 2030.
- [5] T.S. Kavetskyy, O.I. Shpotyuk. 2007. J. Optoelectron. Adv. Mater., 7, 2267.
- [6] O.I. Shpotyuk, A. Kozdras, T.S. Kavetskyy, J. Filipecki, 2006. J. NonCryst. Sol., 352, 700.
- [7] S.R. Elliott. 1992. J. Phys. Cond. Matt., 38, 7661.

- [8] V. Bragaglia, B. Jenichen, A. Giussani, K. Perumal, H. Riechert, R. Calarco. 2014. Appl. Phys., 116, 054913.
- [9] X. Zemin, C. Chaonan, W. Zhewei, W. Ke, C. Haining, Y. Hui. 2018. RSC Advances., 8, 21040-21046.
- [10] Zhang Ting, Liu Bo, Xia Ji-Lin, Song Zhi-Tang, Feng Song-Lin, Chen Bomy. 2004. Chin. Phys. Lett., 21(4), 741-744.
- [11] A.L. Lacaíta. 2006. Sol. St. Electron., 50, 24.
- [12] V. Kovanda, M. Vicek, H. Jain. 2003. J. Non-Cryst. Sol., 88, 326.
- [13] V.I. Mikla. 1997. J. Phys. Condens. Matter, 9, 9209.
- [14] W. Bues, M. Somer, W. Brockner, Z. Naturforsch. 1980. 35B, 1063.
- [15] C. Zha, R. Wang, A. Smith, A. Prasad, R.A. Jarvis, Luther-Davies, B. (2007). J. Mater Sci.: Mater. Electron., 18, 389.
- [16] A. Mendoza-Galvan, E. Garcia-Garcia, Y.V. Vorobiev, Gonzalez-Hernandez. J. Microelectron. Engin. 2000. 51, 677.
- [17] Q.B. Abdullayev, J.S. Abdinov. 1975. Selenium Physics, Baku, Science [in Russian].
- [18] K. Shportko, L. Revutska, O. Paiuk, J. Baran, A. Stronski, A. Gubanov, E. Venger. (2015) Optical Mater. (Amst), 73, 489 - 496.
- [19] B. Liu, Z. Song, T. Zhang, S. Feng. Chen B. 2004. Chin. Phys., 13, 1947.
- [20] E. Cho, S. Yoon, H.R. Yoon, W. Jo. 2006. J. Korean Physical Society, 48 (6), 1616-1618.
- [21] V. Bragaglia, K. Holldack et al. 2016. Scientific Reports, 6: 28560.
- [22] G.G. Sosso, S. Caravati, R. Mazzarello, M. Bernasconi. 2011. Phys. Rev., B83, 134201.
- [23] S.A. Kozyukhin, V.H. Kudoyarova, H.P. Nguyen et al. 2011. Phys. Status Solidi C 8, 9, 2688–2691.
- [24] G. Bulai, O. Pompilian et al. 2019. Nanomaterials, 9, 676.
- [25] P. Nemeč, V. Nazabal, A. Moreac, J. Gutwirth, L. Benes, M. Frumar. 2012. Mater. Chem. Phys., 136, 935-941.
- [26] J. Tominaga, N. Atoda. 1999. Jpn. J. Appl. Phys., 38, L322.
- [27] S. Kozyukhin, M. Veres, H.P. Nguyen, A. Ingram, V. Kudoyarova. 2013. Physics Procedia, 44, 82 – 90.
- [28] K.S. Andrikopoulos, S.N. Yannopoulos, A.V. Kolobov, P. Fons. J. Tominaga. 2006. J. Phys. Condens. Matter, 18.
- [29] G. Lucovsky, D.A. Baker, M.A. Paesler. Phillips J. C. 2007. J. Non-Cryst. Solids, 353, 1713.
- [30] S. Sugai. 1987. Phys. Rev. B: Condens. Matter, 35, 1345.
- [31] J. Koblar, B. Arlin, and G. Shau. 1999. Phys. Rev. B: Condens. Matter, 60.
- [32] E. Yalon, S. Deshmukh et al. 2017. Scientific Reports, 7: 15360.
- [33] K.S. Andrikopoulos, S.N. Yannopoulos, A.V. Kolobov, P. Fons, J. Tominaga. 2006. J. Phys. Condens. Matter, 18.
- [34] P. Nemeč, A. Moreac, V. Nazabal, M. Pavlišta, J. Prikryl, M. Frumar. 2009. J. Appl. Phys., 106, 103509.
- [35] H.R. Yoon, W. Jo, E. Cho, S. Yoon, M. Kim. 2006. J. Non-Cryst. Solids, 352, 3757–3761.

Received: 04.06.2021

GROWTH AND CHARACTERIZATION OF ZnO:Eu THIN FILMS FOR SOLAR CELL APPLICATION

V.F. GREMENOK^{1,2}, E.P. ZARETSKAYA¹, A.N. PYATLITSKI³, N. AKCAY⁴,
T.V. PIATLITSKAYA³, N. N.MUSAYEVA⁵

¹SSPA "Scientific-Practical Materials Research Centre of the National Academy of Sciences of Belarus",

220072, Minsk, P. Brovka Str. 19, Republic of Belarus

²Belarusian State University of Informatics and Radioelectronics, 220013, Minsk, P. Brovka str., 6, Republic of Belarus

³JSC «INTEGRAL» – «INTEGRAL» Holding Managing Company, 220108, Minsk, Kazintsa I.P. str., 121A, Republic of Belarus

⁴Department of Mechanical Engineering, Faculty of Engineering, Baskent University, Ankara, 06790, Turkey

⁵Institute of Physics, ANAS, H.Javid ave. 131, AZ1143, Baku, Azerbaijan

Eu doped ZnO thin films were fabricated on silicon substrates by reactive magnetron sputtering. XRD spectra of the doped samples with different Eu-compositions of 0.5, 1 and 2 wt. %, have been analysed. EDX and AES spectroscopy analysis have been used for determination of Eu concentration and the morphology of the annealed samples are observed by SEM. The analysis show that the average crystal grain size of the 0.5 wt.% ZnO:Eu film is larger than those of the ZnO and 1.0 wt.% films, which is consistent with the narrow FWHM of 0.5 wt.% film and widen FWHM of 1.0 wt.% ZnO:Eu film. It is established, that increasing of concentration of Eu leads to lattice mismatch. The more intense red emission related with Eu³⁺ optical transitions observed for ZnO:Eu films after annealing at 400 °C.

Keywords: thin films, ZnO:Eu, FWHM, PL spectra.

PACS: 68.35-p, 73.50.Pz, 68.37.Hk, 41.50.+h 51.50.+v

INTRODUCTION

Zinc oxide (ZnO) thin films have been widely investigated due to their great potential for different types of applications such as gas sensors, transparent electrodes, light-emitting diodes, solar cells, UV photodetectors, among others [1,2]. However, their electrical and optical properties can be improved by doping with different elements. In recent years, the interest in preparing ZnO thin films doped with lanthanide elements (Ln³⁺) has increased due to the interesting properties that can be obtained by using 4f valence electron elements. It is well known that rare-earth (RE) ions (erbium, terbium, europium, thulium, and so on) are a special kind of photoactive centers with narrow emission lines and long emission lifetimes in various semiconductor materials. Europium (Eu) is of particular interest among rare-earth elements because it shows an intense luminescence in the red spectral region around ~ 620 nm [3 - 9].

It has been demonstrated that Eu acts as an optically active center if it is surrounded by oxygen forming a pseudo-octahedron structure [10]. That means that Eu replacing Zn in the ZnO matrix forms Eu₂O₃ and does not act as an optically active center; therefore, an annealing treatment is required to change Eu local structure, forming clusters either in the ZnO matrix or at the grain boundaries.

In the present work, the influence of Eu ions on the structural and optical properties of ZnO films thermally treated at 200 – 600°C was investigated.

1. EXPERIMENT

ZnO thin films were fabricated on silicon substrates by reactive magnetron sputtering of zinc target doped with Eu element in an argon (Ar) atmosphere with oxygen (10% Ar and 90% O₂) at a pressure of 5×10⁻³ Torr. Europium oxide (Eu₂O₃) pellets were placed on the electron race of the ZnO target surface. The films were grown on the substrates kept at 100 °C. Power density applied to the cathode was 2.0 W/cm² and the deposition time was 1 h. Prior to deposition, all substrates were submitted to the cleaning procedure in ultrasonic bath during 5 min to remove mechanical pollution, and then sent to cleaning in propanol for 5 min and drying with nitrogen flow. After cleaning all the substrates were placed in load lock chamber of deposition unit. The thicknesses of the films were about 700 - 1000 nm. The doping concentrations were in the range of 0.0 - 2.0 wt. % and the annealing temperature varied from 200 to 600 °C. The samples have been annealed for one hour in a quartz tubular furnace.

The structural characteristics of ZnO films were analyzed using Ultima IV X-ray diffractometer (Rigaku) in grazing incidence X-ray diffraction (GIXD) geometry. Chemical composition and the depth profile of elements were determined by energy dispersive X-ray analysis (EDX) and Auger electron spectroscopy (AES). Photoluminescence (PL) and photoluminescence excitation (PLE) measurements were carried out by employing a 1000 W Xe lamp as an excitation source combined with a grating

monochromator (600 grooves/mm, focal length ~ 0.3 m).

2. RESULTS AND DISCUSSION

Figure 1 shows the XRD spectra of the doped samples with different Eu-compositions of 0.5, 1 and 2 wt. %, which have peaks at around 34.5° and correspond to (002) diffraction peak of hexagonal wurtzite ZnO. According to X-ray analysis, ZnO films are polycrystalline and crystallize with a strong preferred orientation along the [001] direction and the *c*-axis perpendicular to the substrate. The diffraction patterns of ZnO films show reflection of the (002) plane of the first- and second-order reflection (004) at $2\theta = 34.5^\circ$ and 72.4° , respectively. The angular position of both peaks is in good agreement with JCPDS card data for nominally pure ZnO [11]. Experimental data indicate that single phase ZnO:Eu layers without any binary phases (europium-oxygen containing compounds) may be fabricated under technological conditions. The as-deposited ZnO thin films did not show any feature related to the Eu₂O₃ phase, suggesting that Eu atoms are either substitutionally replacing Zn in the ZnO lattice or segregated to the non-crystalline region in grain boundaries [7-9].

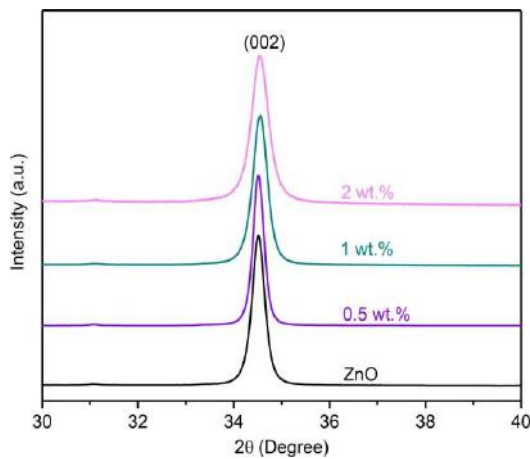


Fig. 1. XRD patterns for ZnO and Eu-doped ZnO films.

On the other hand, when the samples were annealed, the micro-structure of the films was not changed by the plausible oxidation of Eu and presented Eu₂O₃ phase in the XRD patterns (the annealing process was done in an air atmosphere). The presence of Eu₂O₃ phase was not observed in the sample, associated either to the relatively small amount of Eu atoms incorporated into the film (low doping level), or due to the absence of those phases for the employed deposition conditions. The lattice parameter value of films has been estimated from the diffraction peaks related to the ZnO wurtzite structure. All as-deposited films showed *c* parameter values slightly higher than that of ZnO powder material (*c* = 0.521 nm, *a* = 0.325 nm) [1, 10], indicating that the unit cells of thin films are elongated along the *c*-axis and the compressive forces were predominant as usual

in RF sputtered ZnO thin films [6-7]. The internal compressive stress in the as-deposited films is assigned to the bombardment of energetic particles during deposition and not to the thermal stress originating from the difference between the thermal expansion coefficients of the film and the substrate [1].

After the annealing, the peaks were shifted to higher diffraction angles and all the films showed lattice parameters (*a* and *c*) slightly lower than the ideal values for undoped ZnO films. This suggested that the stress was changing from compressive to tensile. It is possible that such high temperature of 600 °C produced tensile stress due to the mismatch between thermal energy coefficients when the films cooled down [7].

It was also observed that the annealing produces variation in the intensity of the main diffraction peak ($2\theta = 34.5^\circ$) and showed an increase in its intensity, which unequivocally indicates an enhancement of the film crystalline arrangement. The average crystallite size in the direction normal to the reflecting planes was increased after the annealing process. The *c*-axis lattice constant was calculated by the Bragg relation and the average grain size was found by the Scherrer's equation.

The composition of the thin films before and after the annealing was estimated from the EDX measurements and appeared to be invariable after the heat treatment (Table 1). The chemical composition was determined by averaging the concentration values from 10 different points on the surface of the same film. The EDX spectrum of each film shows the signals of Zn, O, Si, where the signal of Si is only from the silicon substrate. Because the Eu concentration is too low, there is no signal for Eu element due to the low doping content.

Table 1. Chemical composition of ZnO thin films fabricated on silicon substrates.

Sample	Annealing temperature, °C	Zn, at. %	O, at. %	Eu, at. %
i-ZnO	5	50.2	49.8	
ZnO:Eu	400	50.1	49.9	< 1.0
ZnO:Eu	600	49.0	50.0	< 1.0

A similar elemental composition of ZnO thin films has been confirmed by Auger electron spectroscopy method. The AES spectra were analyzed over a range of kinetic energies from 100 to 1400 eV using the primary electron beam of energy 5 keV. The spectrum of each film shows the signals of Zn, O and Si, where the signal of Si is only from the substrate. Because the Eu concentration is too low, there is no signal for Eu element due to the low doping content. The depth profile of elements is shown in Fig 2. As seen, Zn and O atomic concentrations remained fairly uniform through the depth of the ZnO thin film.

The surface morphology and microstructure of ZnO:Eu thin films were found to be dependent on the preparation conditions. As evident from SEM images the large well-faceted grains without any porosity with dense character of the material may be fabricated on silicon substrates (Fig. 3). The difference in the morphology of as-grown and Eu doped ZnO films after annealing are reflected by the size and shape of grains. ZnO films exhibit large-scale grain size about of ~ 0.1 - 0.3 μm . Actually, both films with no doping or doped could present fewer grain boundaries due to the absence of Eu ions at the grain boundaries. The annealing might have helped the grains to grow much bigger, since high temperature annealing stimulates the migration of grain boundaries and causes the coalescence of more grains.

The average crystal grain size of the 0.5 wt.% ZnO:Eu film is larger than those of the ZnO and 1.0 wt.% films, which is consistent with the narrow FWHM of 0.5 wt.% film and wider FWHM of 1.0 wt.% ZnO:Eu film. Therefore, the increasing of Eu content brings about the smaller grain size and a relatively poor crystalline structure in Eu-doped ZnO films due to the mismatch radius of Eu^{3+} (1.09 \AA) to the ZnO lattice (radius of Zn^{2+} is 0.74 \AA).

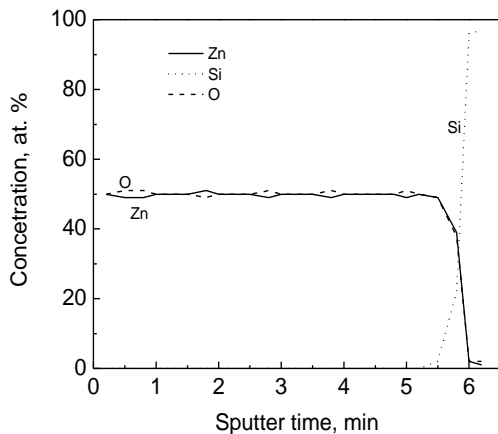


Fig. 2. AES spectra of ZnO:Eu films on a silicon substrate.

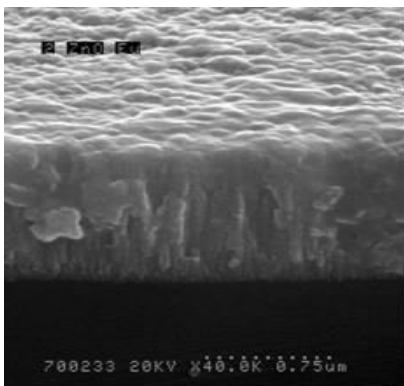


Fig.3. Micrograph of ZnO:Eu film on Si substrate after annealing at 600 °C.

Some attention was concentrated on the photoluminescence and photoluminescence excitation measurements. To determine the nature of the

emission, the experiments with varying excitation and temperature have been performed. Figure 4 shows the typical PL spectra of ZnO:Eu films on silicon substrates for different annealing temperature.

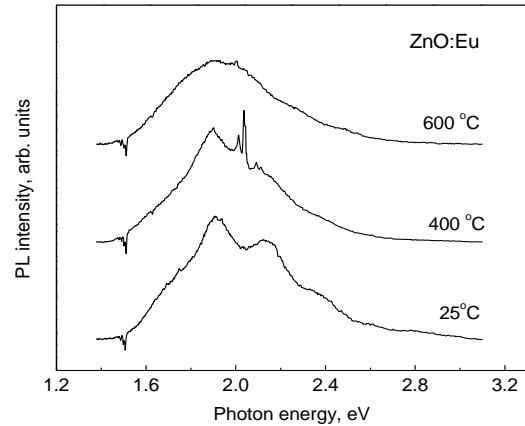


Fig. 4. Room temperature photoluminescence spectra of ZnO:Eu thin films on Si substrates taken for different annealing temperature.

Three broad bands at 2.38, 2.13 and 1.91 eV are presented in photoluminescence spectrum at room temperature for as-grown ZnO:Eu films. A small shift to higher energy about 5 meV is observed for these PL emission bands with increasing measurement temperature in range of 78 – 300 K. No noticeable spectral shifts for these bands were observed when the excitation power was varied from 1 up to 10 W/cm^2 . Therefore, we can conclude that these bands are due to energy band to deep level optical transitions. The experiments show that the relative intensity of these broad bands was depended on the growth process and annealing temperature. In particular, the intensity of green emission band at 2.38 eV decreases with annealing temperature (Fig. 4). The similar behavior of the intensity dependence on annealing temperature has been found for the band at 2.13 eV. Only one broad band at 1.91 eV can be found in PL spectra at annealing temperature higher than 600 °C. The band at 2.38 eV may be related with single ionized oxygen vacancies (V_{O}^-). The bands at 2.13 eV and 1.91 eV probably are due to optical transitions on oxygen atoms occupied Zn positions (O_{Zn}) and oxygen interstitial (O_i) [4,5,9]. The most interesting experimental result is an appearance sharp emission peaks at about 2.086, 2.031, 2.006 and 1.894 eV correspond to transitions of Eu^{3+} from $^5\text{D}_0$ to $^7\text{F}_j$ ($j = 1, 2, 3, 4$) electronic states for ZnO:Eu thin films annealed at temperatures in range of 200 – 600 °C. The more intense red emission related with Eu^{3+} optical transitions observed for ZnO:Eu films after annealing at 400 °C. High-resolution PL spectrum of ZnO:Er related red emission is shown in Fig. 5. Photoluminescence excitation spectra show the existence one broad band at 3.28 eV which is respond to the band gap energy of ZnO:Eu material. This band gap value is coinciding with that found from optical absorption measurements for thin films prepared on glass substrates [5,6,9].

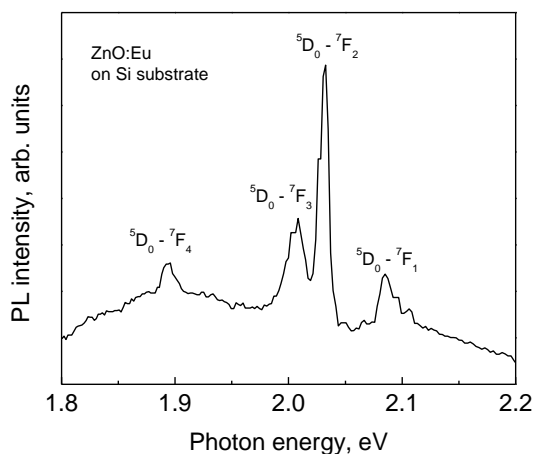


Fig. 5. Room temperature high-resolution PL spectra of ZnO films annealed at 400 °C.

3. CONCLUSION

The structural and optical properties of ZnO:Eu thin films grown on silicon substrates were studied by different experimental techniques. Intense red emission in ZnO films doped by Eu^{3+} is issued by the band-to-band excitation and energy transfer from the host ZnO to europium ions. Thus ZnO:Eu films exhibit bright red emission at low temperature annealing in range of 200 – 400 °C which may be useful for the additional generation of nonequilibrium charge carriers in semiconductor layer under sunlight illumination of thin film solar cells.

This work was carried out with support of the Belarusian Republican Foundation for Fundamental Research grant № T20UK-022 and the state Presidential Fund's financial support (2021 year).

-
- [1] K.T. Ramakrishna Reddy, N. Koteswara Reddy, R.W. Miles. *Solar Energy Materials & Solar Cells*, 2006. vol. 90, pp. 3041–3046.
- [2] V.A. Coleman, A. Victoria, C. Jagadish. *Basic Properties and Applications of ZnO, Zinc Oxide Bulk, Thin Films and Nanostructures*, Elsevier Science Ltd, Amsterdam, 2006, p.600.
- [3] Y.K. Mishra, G. Modi, V. Cretu, V. Postica, O. Lupan, T. Reimer, I. Paulowicz, R. Adelung. *ACS Appl. Mater. Interfaces*, 2015, vol. 7, pp.14303–14316.
- [4] O.M. Ntwaeaborwa, S.J. Mofokeng, V. Kumar, R.E. Kroon. 2017, *Spectrochim. Acta A.*, 2017, vol. 182, pp. 42–49.
- [5] V. Kumar, S. Som, M.M. Duvenhage, H.C. Swart. *Appl. Surf. Sci.*, 2014, vol. 308, pp.419–430.
- [6] W.L. Dang, Y.Q. Fu, J.K. Luo, A.J. Flewitt, W.I. Milne. *Superlattices Microstruct.*, 2007, vol. 42, pp.89–93.
- [7] E.M Bachari, G. Baud, S. B. Amor, M. Jacquet. *Thin Solid Films*, 1999, vol.348, pp.165–172.
- [8] Ishizumi, S. Fujita, H. Yanagi. 2011. *Opt. Mater.*, 2011, vol.33, pp.1116–1119.
- [9] H. Shahroosvand, M. Ghorbaniasl. *J. Lumin.* 2013, vol.144, pp.223–229.
- [10] L. Douglas, R. Mundle, R. Konda, C. E. Bonner, A. K. Pradhan, J-L. Huan. *Opt. Lett.*, 2008, vol. 33, pp. 815–817.

Received: 07.06.2021

TECHNIQUE OF SOLUTION CONCENTRATION CONTROL OF POLAR SUBSTANCE IN NONPOLAR SOLVENT

S.T. AZIZOV

Institute of Physics of Azerbaijan NAS

131, H.Javid ave., Baku, AZ 1143

e – mail: samir_azizov@mail.ru

The investigation data relating to creation of control devices of chemical engineering processes such as control systems of diluted solutions of polar substances in nonpolar solvent, are given.

Keywords: dielectric spectroscopy, dielectric constant, dielectric properties, reflection characteristics of electromagnetic radiation, chemical engineering processes.

PACS: 61.20. – p; 77.22. – d; 77.22. Gm;

1. INTRODUCTION

The series of technological devices in which it is necessary the maintenance of the polar substance solution concentration in nonpolar solvent with high accuracy, are known [1].

The known methods of control and maintenance of such solution concentration require regular discrete selection of solution tests, that are disadvantages of such technological devices. This leads to breakdown of technological process progress and takes a lot of time.

The closest one is the device the principle of its operation is based on application of control method of continuous supply of given solution of polar substance in nonpolar solvent [2,3]. It is necessary to note that the imperfection of mechanical system of solution supply at accuracy increase of maintenance of necessary solution concentration of polar substance in polar solvent is the disadvantage of such device.

The technique presented in the paper can be used for control of polar substance diluted solutions of polar substance in nonpolar solvent because of the fact that obtained systems can be used for formation of given wave ranges of non-reflecting absorbents containing in their composition the high-disperse polar liquids and their solutions in nonpolar solvent [4,5]. The absorbents of SHF radiation on the base of polar liquids and their solutions in non-polar solvent effectively utilize the residual and often undesirable electromagnetic radiation.

2. EXPERIMENTAL PART

The investigation task is the improvement of technique efficiency allowing us to continuously regulate the given concentration of polar substance in nonpolar solvent not stopping the technological process. The advantage of such technique is the fact that concentration accuracy doesn't decrease at decrease of solution concentration and vice versa, increases up to definite concentrations. It is established that the total absorption of incident radiation in solution can appear at definite selection of radiation frequency, solution composition and layer thickness, based on the papers on investigation of reflection characteristics of

electromagnetic radiation from polar substance layer in nonpolar solvent [6,7]. The computer with software allows us to continuously regulate the incident radiation frequency and the given polar substance concentration in nonpolar solvent not stopping technological process that allows us to obtain the required quantity of polar substance solution in nonpolar solvent. The last stabilization of this solution composition is supplied by autocompensation control system.

The method is based on creation of the device which allows us continuously regulate the incident radiation frequency and given polar substance concentration in nonpolar solvent not stopping the technological process. The device block-diagram allowing the control of the given polar substance concentration in nonpolar solvent consists in: 1 is the computer with specific software which allows us continuously regulate the incident radiation frequency and the given polar substance concentration in initial raw material not stopping the technological process; 2 is microwave radiation generator; 3 is the waveguide measure cell of flow type which is short-circuit in the end connected with generator; 4 is directed coupler with detector section. The stabilization of solution initial composition takes place by autocompensation control system; 5 is low-frequency modulator; 6 is amplifier detector section; 7 is phase detector; 8 is reversible engine; 9 is microadjust gate connected with axis of reversible engine; 10 is blender of solution polar component.

3. RESULT DISCUSSION

The stabilization system of the given composition of continuously proportioning solution of polar substance in initial raw material is given based on the effect of non-reflecting absorption of incident electromagnetic radiation.

The control of generator frequency and solution thickness layer in the cell is taken by conditions of non-reflecting radiation absorption for the given solution composition and it is supplied by computer with software during the period of whole chemical engineering process.

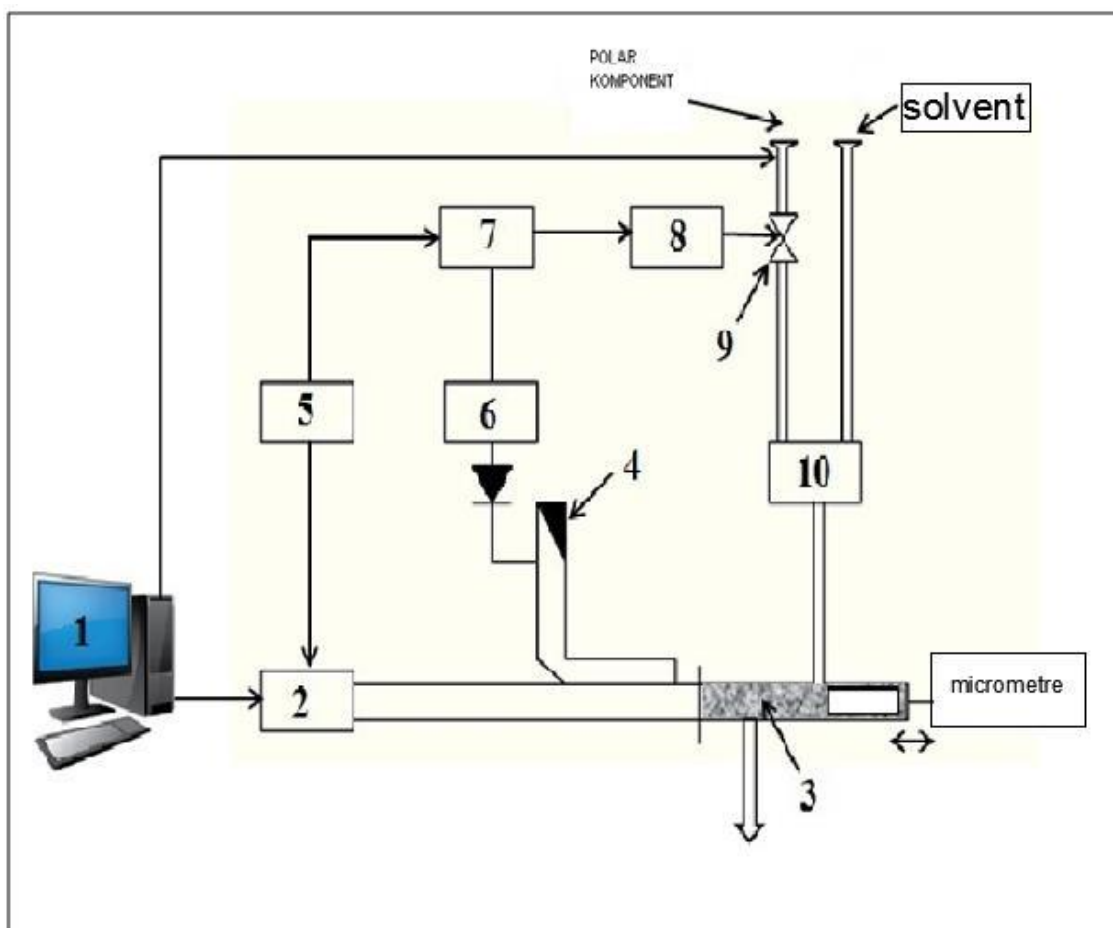


Fig. 1. The device block-diagram of concentration control of polar substance solution in nonpolar solvent.

The device works by the following way. The computer with software supplies the close control of generator frequency and also the thickness of the layer of the initial solution given into cell at which the conditions of total radiation absorption for the given solution composition are selected [8]. Further, the stabilization of solution initial composition by autocompensation control system which consists in low-frequency frequency modulator of generator output signal and amplifier for emphasizing and amplification of modulation action takes place. The outputs of these devices are connected with inputs of phase detector controlling the reversible engine work. The microadjust gate of supply of solution polar component into blender is connected with axis of reversible engine. The error signal is formed at composition value change on given one on the output of phase detector. The compensation control of composition value of proportioning solution up to the given value is carried out in the dependence on sign and value of error signal with the help of gate.

The graduation of stabilization system is carried out in two ways. Firstly, the characteristics of electromagnetic radiation reflection from layer of required solution of polar substance in non-polar solvent are taken. Later, graduation control is carried out at chosen concentration with switched off system of automatic maintenance of the given concentration.

4. CONCLUSION

The system of continuous control of chemical engineering processes and such as the control system of diluted solution concentrations of polar substances in non-polar solvent are supposed.

The improvement of device work efficiency allowing the continuously regulate the given concentration of polar substance in non-polar solvent not stopping technological process, is the task of the supposed technique. The computer with specific software is connected to device which allow us the continuous control the incident radiation frequency and given concentration of polar substance in non-polar solvent not stopping technological process. The given advice can be used for control of diluted solution concentrations of polar substances in non-polar solvent because of which obtained systems can be used at projection for the given range of wave length of SHF radiation absorbers consisting in the high-disperse polar liquid solutions in non-polar solvent. The task of the supposed technique is the improvement of device efficiency allowing continuously control the given concentration of polar substance in non-polar solvent not stopping technological process. The supposed technique is based on investigation of characteristics of electromagnetic radiation reflection from polar substance layer in non-polar solvent.

- [1] *T.N. Kosareva, R.S. Begunov, A.N. Valayeva, U.S. Yakovleva.* The main and side processes at reconstruction of 2,4-dinitroanisole by stannum chloride (II), Bashkir chemical journal, 2010, vol.17. № 4, pp.1–15, (in Russian).
- [2] *S.T. Azizov, M.A. Sadikhov, S.R. Kasimova, Ch.O. Qadjar.* The method of automatic control of polar substance concentration in non-polar solvent, ANAS Transactions, Physics-Math, Math, Astronomy, №2, vol. XXV, Baku, 2005, pp.161–163, (in Azeri).
- [3] *S. Sudo, N. Shinyashiki, Y. Kitsuki, S. Yagihara.* Dielectric Relaxation Time and Relaxation Time Distribution of Alcohol –Water Mixtures, J. Phys. Chem. 106, 3 (2002) 458–464.
- [4] *S.T. Azizov, O.A. Aliyev.* Dielectric dispersion of absorption of glucine water solution, AJP “Fizika”, vol. XXIII, №4, 2017, pp.13–16.
- [5] *S.T. Azizov, Sh.K. Agamuradova, A.J. Khalilov.* Absorber of electromagnetic radiation on the base of composite materials, Azerbaijan, Patent İ 2012 0097, 2012.
- [6] *N.E. Kazantseva, N.G. Rivkina, I.A. Chmutin.* Perspective materials for absorbers of electromagnetic waves of super-high-frequency range, Radiotechnique and electronics, vol. 48, №2, pp.196–209, 2003.
- [7] *A. Chaudhari, A.G. Shankarwar, B.R. Arbad, S.C. Mehrota.* Dielectric Relaxation in Glycine – Water and Glycine – Ethanol – Water solutions using time domain reflectometry, Journal of Solution Chemistry, Volume 33, №3, pp.313–322, 2004.
- [8] *S.T. Azizov.* The development of microwave investigation methods of strongly absorbing substances and amide dielectric properties, PhD thesis, 103 p., Baku, 2000.

Received: 31.05.2021

TlGa_{1-x}Er_xSe₂ SOLID SOLUTIONS, THEIR ELECTRICAL AND OPTICAL PROPERTIES

E.M. KERIMOVA, S.N. MUSTAFAEVA, N.Z. GASANOV, K.M. HUSEYNOVA,
Q.M. SHARIFOV

Institute of Physics, National Academy of Sciences of Azerbaijan, Baku, AZ-1143

*e-mail: *ngasanov@yandex.ru*

The complex permittivity, dielectric loss tangent, and conductivity σ_{ac} of TlGa_{1-x}Er_xSe₂ solid solutions ($x = 0; 0.001; 0.005$) were studied in the temperature range 150-300 K in an alternating electric field (25-10⁶ Hz). The change in dielectric constant as a function of temperature in the studied crystals is due to the presence of low-frequency relaxation polarization. Conductivity obeys the law $\sigma_{ac} \sim f^{0.8}$ at frequencies of 10²-10⁴ Hz, which, in the studied crystals, indicates the presence of hopping conductivity by states localized near the Fermi level. The parameters of the states localized in the TlGa_{1-x}Er_xSe₂ band gap are estimated. It was shown that an increase in the Er impurity leads to an increase in the density of localized states in TlGaSe₂ and a decrease in their energy spread. The optical absorption edge of TlGa_{1-x}Er_xSe₂ crystals was studied, and the temperature dependence of the band gap in them was obtained.

Keywords: solid solutions, complex dielectric permittivity, frequency dispersion, dielectric loss, conductivity, optical absorption edge.

PACS: 72.20.-i ; 78.00.00

1. INTRODUCTION

TlGaSe₂ crystal has a layered structure of A^{III}B^{III}C^{VI}₂ thallium chalcogenide type compounds. This crystal has a monoclinic structure, C2/c-C_{2h}⁶ space group, with unit cell parameters $a = 10.772$, $b = 10.771$, $c = 15.636$, $\beta = 100.6^\circ$ [1].

TlGaSe₂ is a p-type wide-gap semiconductor and possesses practically important physical characteristics: high photo- and X-ray sensitivity. On its basis, photoelectric converters, spectrum analyzers, X-ray, gamma, and neutron detectors [2,3,4] are developed, and the possibility of creating a phototransistor is shown [5].

In [6,7], hopping conductivity in TlGaSe₂ single crystals was studied. The results of studying the effect of γ radiation on the conductivity and dielectric characteristics of TlGaSe₂ single crystals are presented in [8,9]. Many works, for example [10,11], are devoted to the study of the optical properties of the TlGaSe₂ compound.

Specific feature of A^{III}B^{III}C^{VI}₂ family crystals is that these semiconductors also possess ferroelectric properties. Due to the layered structure, polytypic modifications occur, resulting in changes in their physical properties [12]. In addition, a large number of crystals of this type are characterized by consecutive phase transitions [13,14].

Our assessment of the solubility of erbium in the TlGaSe₂ lattice, taking into account the known effective ionic atomic radii, indicates that the radius of the implanted Er³⁺ impurity atom (1.03Å) is closer to the Ga³⁺ radius (0.76Å) than to the Tl¹⁺ radius (1.64Å), i.e. the partial replacement of gallium with erbium in layered TlGaSe₂ crystals corresponds to the condition for the formation of a substitution solution. The aim of this work is to study the electrical, dielectric, and optical properties of TlGa_{1-x}Er_xSe₂ solid solutions ($x = 0; 0.001; 0.005$).

2. METHODS OF THE INVESTIGATION

The synthesis of TlGa_{1-x}Er_xSe₂ solid solutions ($x = 0; 0.001; 0.005$) was carried out by fusing highly pure chemical elements taken in stoichiometric ratios in quartz ampoules evacuated to 10⁻³ Pa. Samples were homogenized by annealing at a temperature of 750K for 120h. Single crystals of TlGa_{1-x}Er_xSe₂ were grown from the synthesized compounds by the Bridgman method [15]. The crystals were layered and easily chipped along the basic plane. X-ray phase analysis of the obtained samples was carried out on a D8-ADVANCE diffractometer in the mode 0.5° < 2 θ < 80° (CuK α radiation, $\lambda = 1.5418\text{Å}$).

The dielectric constant ϵ and the dielectric loss tangent $\tan\delta$ were measured using the capacitor method in the temperature range 150-300 K using an E7-25 digital device on single-crystal wafers 0.2-0.3 mm thick. The contacts were made of silver paste. The frequency range of the alternating electric field was 25-10⁶ Hz.

The measurements of the capacity of the samples were carried out with an accuracy of ± 0.01 pF, and the error in measuring the quality factor ($Q = 1/\tan\delta$) was 0.001%.

The electrical conductivity σ was measured along the layers by the four-probe method in the mode of continuous increase (decrease) in the sample temperature at a rate of ≈ 0.1 K/min. The amplitude of the alternating electric field applied to the samples was within the ohmic region of the current-voltage characteristic.

Samples for studying the optical absorption spectra of layered semiconductor crystals of TlGa_{1-x}Er_xSe₂ ($x = 0; 0.001; 0.005$) were chipped from a single-crystal ingot and had the form of thin plates with a thickness of 20 to 140 μm . Light was directed to the samples parallel to the crystallographic axis c . The optical transmission spectra were studied using an apparatus based on an MDR-23 monochromator and a

nitrogen cryostat with temperature stabilization in the range 77–300K (stabilization accuracy ±0.5K). The resolution of the installation was 2 Å.

To measure the optical absorption coefficient in a wide range from 10 to 10⁴ cm⁻¹, we used the data of measurements of the intensity of the light beam passing through samples with different thicknesses, and to cover the entire interval, we had to break it into 3 sections and take into account the transmission measurements of three pairs of samples of corresponding thicknesses for each composition studied. For each plot, the absorption coefficient was calculated by the formula $\alpha = 1/(d_2 - d_1) \ln(I_1/I_2)$, where d_1 and d_2 are the thicknesses of the samples, and I_1 and I_2 are the intensities of the light transmitted through them. Since the value of αd was greater than unity for each sample and the corresponding section, the interference of light beams passing through and reflected from the back plane of the crystal plate was very weak, and we did not observe it.

3. EXPERIMENT RESULTS AND DISCUSSION

When processing X-ray data of TlGa_{1-x}Er_xSe₂ solid solutions, it was found that the amount of Er impurity element used ($x = 0.001; 0.005$) has little effect on the lattice parameters of the initial TlGaSe₂ compound. However, the addition of Er to TlGaSe₂ leads to a change in the color of the initial crystal to a darker one (see Fig.1).

The results of X-ray analysis of the crystals under study are presented in Tables 1, 2 and 3. X-ray studies showed that TlGa_{1-x}Er_xSe₂ ($x = 0; 0.001; 0.005$) single crystals have a monoclinic structure, space group C_s^4 , and the following lattice parameters were obtained: $a = 10.744 \text{ \AA}$, $b = 10.773 \text{ \AA}$, $c = 15.623 \text{ \AA}$, $\beta = 100.04^\circ$, $z=16$, which is in good agreement with [1]. The frequency dependences of the conductivity of TlGa_{1-x}Er_xSe₂ crystals at room temperature are shown in the Fig.2.



Fig. 1. Single crystals grown by the Bridgman method: TlGaSe₂ on the left, TlGa_{0.995}Er_{0.005}Se₂ on the right.

Table 1.

Calculation of the X-ray diffraction pattern of the TlGa_{0.999}Er_{0.001}Se₂ crystal.

N ₀	2θ	I/I ₀ , %	d _{exp} (Å)	d _{calc} (Å)	hkl
1	11°46'	17,4	7,715	7,695	200
2	23°11'	100	3,845	3,878	422
3	23°6'	8,1	3,767	3,778	122
4	24°95'	2,8	3,566	2,568	222
5	26°30'	2	3,386	2,398	031
6	27°54'	6,4	3,236	2,236	322
7	31°09'	18,9	2,875	2,878	422
8	33°82'	2,9	2,648	2,650	140
9	34°97'	31,8	2,564	2,544	522
10	37°80'	2,1	2,378	2,382	404
11	47°26'	7,7	1,922	1,924	215
12	47°80'	5,8	1,901	1,902	144
13	53°84'	2,8	1,702	1,703	740
14	56°27'	2	1,634	1,634	831
15	58°13'	2,1	1,586	1,587	362

Table 2.

Calculation of the X-ray diffraction pattern of the $TlGa_{0,995}Er_{0,005}Se_2$ crystal.

№	2θ	I/I ₀ , %	d _{exp} (Å)	d _{calc} (Å)	hkl
1	11°44'	13,8	7,726	7,625	200
2	23°11'	100	3,846	3,847	400
3	23°52'	8,3	3,779	3,777	122
4	24°98'	2,4	3,562	2,568	222
5	26°33'	2,5	3,382	2,392	031
6	27°54'	6,4	3,237	2,237	322
7	31°05'	18,5	2,878	2,878	422
8	33°83'	4	2,648	2,650	140
9	35°01'	43,1	2,561	2,565	600
10	35°40'	2,5	2,534	2,544	522
11	41°42'	1,8	2,178	2,185	711
12	47°25'	7,9	1,922	1,923	802
13	47°81'	5	1,901	1,902	144
14	50°52'	1,6	1,805	1,806	153
15	53°88'	3,4	1,700	1,702	740
16	56°18'	1,9	1,636	1,634	426
17	58°15'	1,9	1,585	1,587	362
18	64°14'	1,4	1,451	1,437	835
19	65°05'	1,8	1,433	1,433	264

Table 3.

Crystal lattice parameters of solid solutions of the $TlGaSe_2$ - $TlErSe_2$ system.

Compound	Crystal lattice system	Crystal lattice parameters, (Å)			The number of formula units in a unit cell, Z
		a	b	c	
$TlGa_{0,999}Er_{0,001}Se_2$	monoclinic	10,744	10,773	15,623	16
$TlGa_{0,995}Er_{0,005}Se_2$	monoclinic	10,744	10,773	15,623	16
$TlGaSe_2$	monoclinic	10,715	10,694	15,690	16

Table 4.

The parameters of localized states in $TlGa_{1-x}Er_xSe_2$ solid solutions obtained from high-frequency dielectric measurements.

Crystal composition $TlGa_{1-x}Er_xSe_2$	T, K	$N_F, eV^{-1}cm^{-3}$	$\Delta E, meV$	N_t, cm^{-3}
x = 0	180	$1.54 \cdot 10^{18}$	10	$1.54 \cdot 10^{16}$
	230	$1.76 \cdot 10^{18}$	9	$1.56 \cdot 10^{16}$
	300	$2.23 \cdot 10^{18}$	7	$1.57 \cdot 10^{16}$
x = 0.005	180	$2.48 \cdot 10^{18}$	6.7	$1.66 \cdot 10^{16}$
	230	$2.58 \cdot 10^{18}$	6.3	$1.62 \cdot 10^{16}$
	300	$3.08 \cdot 10^{18}$	5	$1.54 \cdot 10^{16}$

From this it can be seen that for compositions with 0.5% and 1% Er, the difference is small. Therefore, we studied the temperature dependences of the dielectric characteristics for the composition $TlGa_{0,995}Er_{0,005}Se_2$.

Fig. 3(a) ($TlGaSe_2$) and 3(b) (Er 0.5%) show the temperature dependence of the dielectric permittivity ϵ . It can be seen that, with increasing temperature, ϵ has a tendency to increase, especially at low frequencies.

Fig. 4 shows the temperature dependence of the electrical conductivity σ . For the $TlGa_{0,995}Er_{0,005}Se_2$ samples, as shown in the dielectric permittivity, the value of σ increases as the temperature increases. The absolute value of σ depends on the frequency of the measurement area, which is more pronounced at lower temperatures. The value of σ increases several times as the frequency increases. At low temperatures,

conductivity is practically independent of temperature. In the high temperature region, the conductivity increases exponentially with the law of $\sigma \sim e^{1/T}$. This indicates that at high temperatures σ mainly depends on the concentration of the main carriers.

Fig. 5(a) and 5(b) show the temperature dependence of the dielectric loss tangent ($\tan\delta$). As can be seen from the pictures, the values of the $\tan\delta$ of the TlGa_{0.995}Er_{0.005}Se₂ crystal increase as the temperature rises compared with TlGaSe₂. This increase can be related to the increased concentration of free charge carriers.

As can be seen from Fig.6, the value of the dielectric permittivity of TlGa_{1-x}Er_xSe₂ solid solutions decreases with increasing frequency. Such behavior of the dielectric permittivity in the studied crystals is due to the presence of low relaxation polarization at low frequencies, causing dielectric loss at low frequencies. In the $\tan\delta(T)$ curves, the semiconductor maximums

are visible and spread when the frequency of the measurement increases from 1kHz to 1MHz.

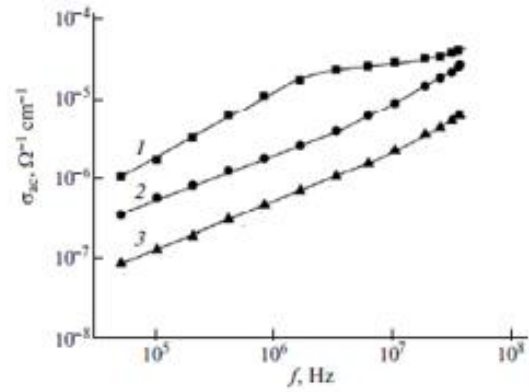


Fig. 2. Frequency dependent ac-conductivity of the TlGa_{1-x}Er_xSe₂ crystals: $x = 0$ (1), 0.001 (2), 0.005 (3). $T = 300$ K.

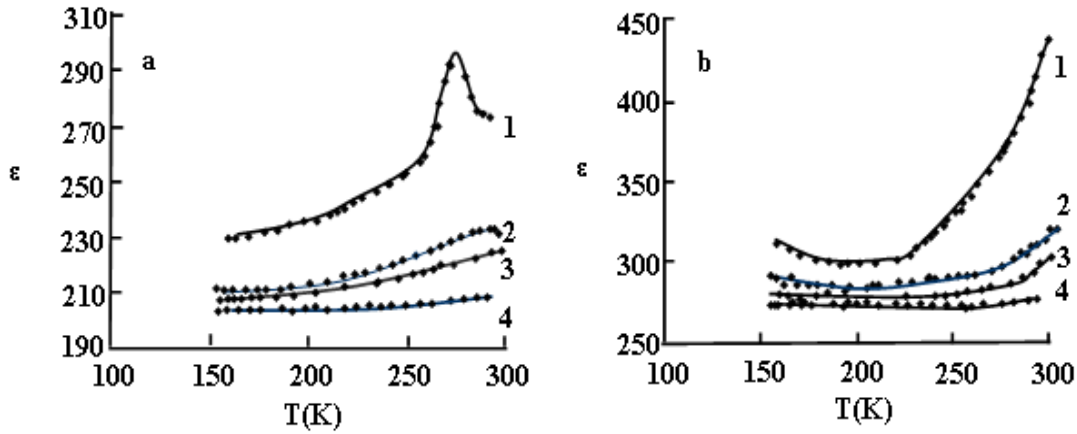


Fig. 3. Temperature dependence of dielectric permittivity of the TlGa_{1-x}Er_xSe₂ single crystal: a) $x=0$; b) $x=0.005$. (1- 1 kHz, 2- 10 kHz, 3- 100 kHz, 4- 1 MHz).

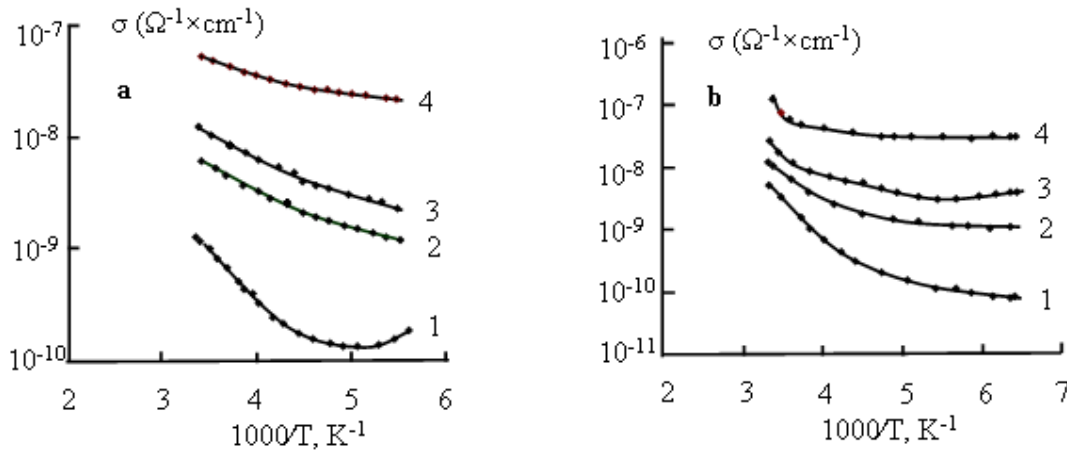


Fig. 4. Temperature dependence of the electrical conductivity of the TlGa_{1-x}Er_xSe₂ crystals: a) $x=0$; b) $x=0.005$. (1-1kHz, 2-10 kHz, 3-100kHz, 4-1MHz).

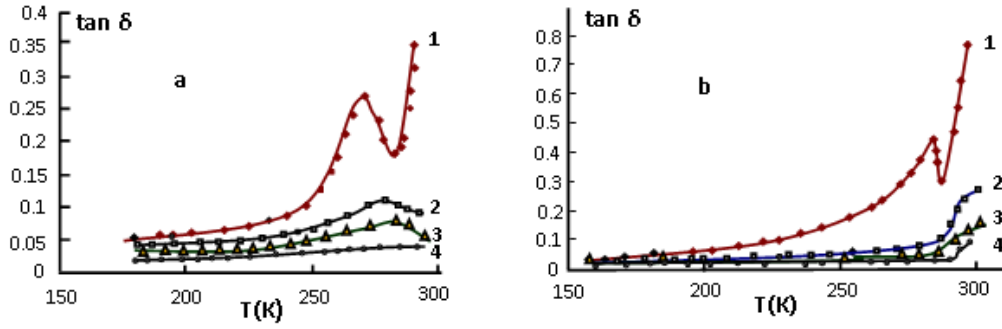


Fig. 5. Temperature dependence of the loss tangent in the $TiGa_{1-x}Er_xSe_2$ crystals: a) $x=0$; b) $x=0.005$. (1-1kHz, 2-10 kHz, 3-100kHz, 4-1MHz).

That is, these maximums are located in the temperature region, where the value of the dielectric permittivity is sharply increased. This anomaly is due to the ferroelectric phase transition in $TiGaSe_2$, which is also due to the dimensionless phase in the temperature region [16]. The real part of dielectric permittivity (ϵ') decreases with increasing frequency for $TiGaSe_2$ and $TiGa_{0.995}Er_{0.005}Se_2$. The increase in temperature, as well as the impurity of 0.5% Er in the $TiGaSe_2$ crystal, significantly increases the value of the ϵ' .

The frequency dependence of the imaginary part ϵ'' of the complex dielectric permittivity of $TiGa_{1-x}Er_xSe_2$ ($x=0; 0.005$) crystals at different temperatures is

shown in Fig. 7. It is determined that the frequency dependence of the imaginary part of the complex dielectric permittivity is of a relaxation nature.

Fig. 8 shows the comparison of the frequency dependence of the $\tan\delta$ of the $TiGaSe_2$ (curve 1) and the $TiGa_{0.995}Er_{0.005}Se_2$ (curve 2) crystals. This dependence is characterized by hyperbolic reduction, which is associated with a loss of conductivity. The increase of $\tan\delta$ at high frequencies indicates the presence of relaxation losses. Compared to $TiGaSe_2$, the value of the $\tan\delta$ of $TiGa_{0.995}Er_{0.005}Se_2$ crystal is significantly increased.

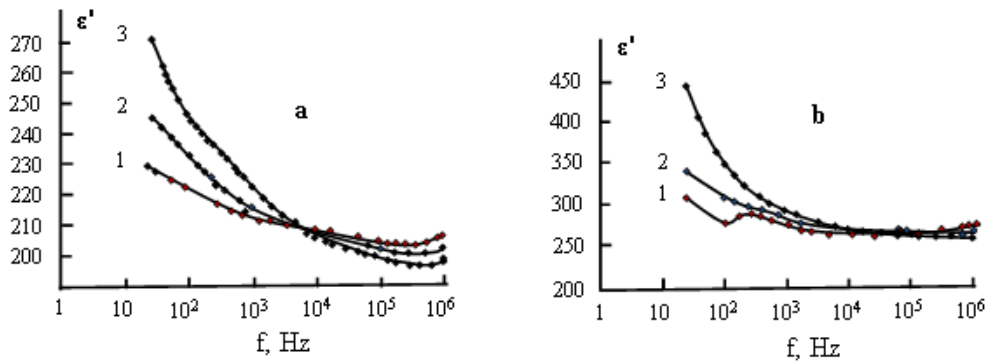


Fig. 6. Frequency dependences of the real part of the complex dielectric permittivity of $TiGa_{1-x}Er_xSe_2$ crystals: a) $x=0$; b) $x=0.005$. T: 1-180 K, 2-230 K, 3-300 K.

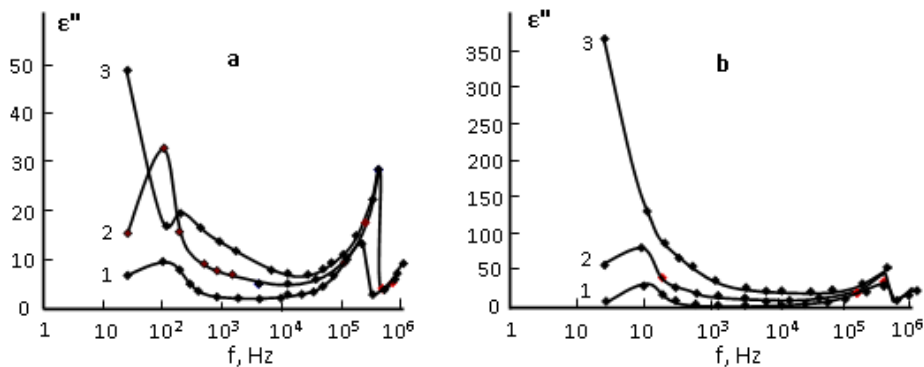


Fig. 7. Frequency dependences of the imaginary part of the complex dielectric permittivity of $TiGa_{1-x}Er_xSe_2$ crystals: a) $x=0$; b) $x=0.005$. T: 1-180 K, 2-230 K, 3-300 K.

We also investigated the frequency dependence of the ac-conductivity in TlGa_{1-x}Er_xSe₂ ($x=0; 0.005$) crystals (Fig. 9).

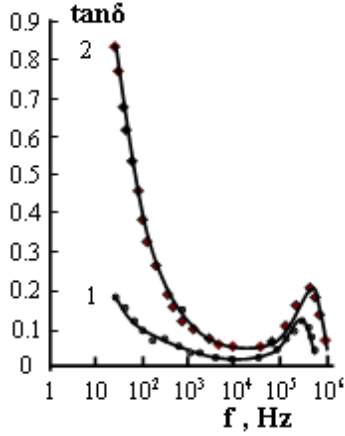


Fig. 8. Frequency dependences of dielectric loss tangent in TlGa_{1-x}Er_xSe₂ crystals: 1) $x=0$; 2) $x=0.005$, $T = 300$ K

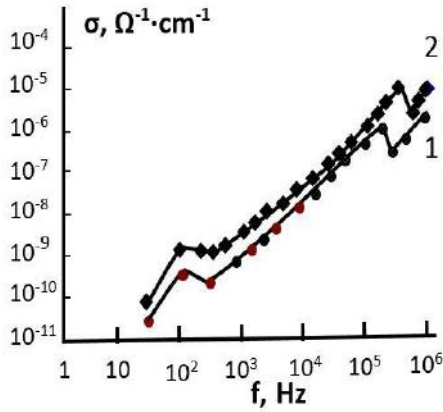


Fig. 9. Frequency dependence of the conductivity of TlGa_{1-x}Er_xSe₂ crystals: 1) $x = 0$, 2) $x=0.005$. $T=180$ K.

The σ_{ac} value for TlGa_{0.995}Er_{0.005}Se₂ solid solution is higher than for TlGaSe₂ crystal.

The dependence curves $\sigma_{ac}(f)$ of TlGa_{1-x}Er_xSe₂ ($x=0; 0.005$) solid solution are observed in 3 parts: in the first case, $\sigma_{ac} \sim f^{0.6}$ was observed and then increased to $\sigma_{ac} \sim f^{0.8}$ ($10^2 - 10^4$ Hz). Then, when the frequency was increased to 1 MHz, it was replaced by $\sigma_{ac} \sim f^{1.2}$. The fact that we obtain it from the law of $\sigma_{ac} \sim f^{0.8}$

indicates that there is the hopping conductivity in localized states near the Fermi level.

Table 4 shows the calculated parameters for TlGa_{1-x}Er_xSe₂ ($x=0; 0.005$) ($f = 10^4$ Hz) within the Mott approximation of solid solutions. The dependence of $\sigma_{ac} \sim f^{0.8}$ on the studied crystals at $10^2 - 10^4$ Hz frequencies is observed. The density of localized states (N_F) near the Fermi level for the TlGa_{1-x}Er_xSe₂ ($x=0; 0.005$) solid solutions is calculated according to Mott's theory [17] by the formula:

$$\sigma_{ac}(f) = \frac{\pi^3}{96} e^2 k T N_F^2 a^5 f \left[\ln \left(\frac{v_{ph}}{f} \right) \right]^4$$

Here e is the elementary charge, k - Boltzman constant, N_F - density of states near the Fermi level, $a = 1/a$ is the localization radius, $\psi \sim e^{-ar}$ is the wave function of the localized charge carriers; v_{ph} - phonon frequency. When calculating the density of localized states near the Fermi level, the localization radius $a = 34 \text{ \AA}$ was taken for the TlGaSe₂ crystal [15]. The value of the density of localized states (N_F) near the Fermi level calculated by Mott's theory is given in the table 1. When the temperature increases for 0.5 % Er samples, the value of the density of localized states near the Fermi level increases ($N_F = 2.23 \times 10^{18} \text{ eV}^{-1} \text{cm}^{-3}$ when $x = 0$, and $N_F = 3.08 \times 10^{18} \text{ eV}^{-1} \text{cm}^{-3}$ when $x=0.005$). According to the theory of hopping conductivity in the alternating current, the hopping distance (R) is determined by the expression [17]:

$$R = \frac{1}{2a} \ln \left(\frac{v_{ph}}{f} \right)$$

The value of the R and E_a was calculated for TlGa_{1-x}Er_xSe₂ crystals: $R=312 \text{ \AA}$ at 10^4 Hz [17]:

$$\Delta E = \frac{3}{2\pi R^3 N_F}, \quad E_a = \left(\frac{kT}{N_F a^3} \right)^{\frac{1}{4}}$$

According to this expression, the energy spread ΔE of the states localized near the Fermi level in TlGa_{1-x}Er_xSe₂ can be estimated.

Table 4 shows that the increase in temperature and the presence of Er in TlGaSe₂ increases the density of localized states near the Fermi level, narrows the energy spread ΔE , and changes the value of concentration on local levels.

Table 4.

The parameters of localized states in TlGa_{1-x}Er_xSe₂ solid solutions obtained from high-frequency dielectric measurements.

Crystal composition TlGa _{1-x} Er _x Se ₂	T, K	$N_F, \text{eV}^{-1} \text{cm}^{-3}$	$\Delta E, \text{meV}$	N_t, cm^{-3}	E_a, eV
$x = 0$	180	$1.54 \cdot 10^{18}$	10	$1.54 \cdot 10^{16}$	0.088
	230	$1.76 \cdot 10^{18}$	9	$1.56 \cdot 10^{16}$	0.102
	300	$2.23 \cdot 10^{18}$	7	$1.57 \cdot 10^{16}$	0.118
$x = 0.005$	180	$2.48 \cdot 10^{18}$	6.7	$1.66 \cdot 10^{16}$	0.078
	230	$2.58 \cdot 10^{18}$	6.3	$1.62 \cdot 10^{16}$	0.093
	300	$3.08 \cdot 10^{18}$	5	$1.54 \cdot 10^{16}$	0.109

The analysis of the absorption spectra of $\text{TlGa}_{1-x}\text{Er}_x\text{Se}_2$ crystals, namely, the dependence of $(\alpha\hbar\omega)^2$ on the photon energy $\hbar\omega$, made it possible to determine the energies of direct transitions in the studied crystals, and, consequently, their band gap E_g . In the temperature range from 77 to 300 K, the temperature dependences of the band gap of the studied solid solutions were constructed (Fig. 10).

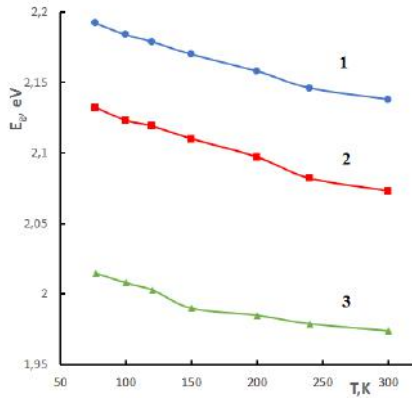


Fig. 10. Temperature dependences of the band gap of $\text{TlGa}_{1-x}\text{Er}_x\text{Se}_2$ single crystals. 1 - $x = 0$; 2 - $x = 0.001$; 3 - $x = 0.005$.

The experiment showed that the following differences are observed in the structure of the absorption edge of TlGaSe_2 single crystals and $\text{TlGa}_{1-x}\text{Er}_x\text{Se}_2$ solid solutions: at low temperatures, the

absorption band associated with the formation of an exciton near the direct edge cannot be detected in solid solutions; the absorption coefficient in $\text{TlGa}_{1-x}\text{Er}_x\text{Se}_2$ is noticeably higher than in TlGaSe_2 . The average temperature coefficient of the band gap dE_g/dT in the temperature range 77-300K for TlGaSe_2 and $\text{TlGa}_{0.999}\text{Er}_{0.001}\text{Se}_2$ is $-2.4 \cdot 10^{-4}$ eV/K, and for $\text{TlGa}_{0.995}\text{Er}_{0.005}\text{Se}_2$ is $-1.9 \cdot 10^{-4}$ eV/K. The long-wavelength band gap shift for $\text{TlGa}_{0.999}\text{Er}_{0.001}\text{Se}_2$ relative to TlGaSe_2 at $T=77$ K is 60 meV, and for $\text{TlGa}_{0.995}\text{Er}_{0.005}\text{Se}_2$ it is 177 meV.

4. CONCLUSIONS

The electrical conductivity, dielectric constant, and dielectric loss tangent of the $\text{TlGa}_{1-x}\text{Er}_x\text{Se}_2$ solid solution in an alternating electric field are investigated. In the crystals studied, the change in the dielectric constant as a function of temperature (150–300 K) at low frequencies is associated with the presence of relaxation polarization. $\sigma_{ac}(f)$ in $\text{TlGa}_{1-x}\text{Er}_x\text{Se}_2$ ($x = 0; 0.005$) crystals, at frequencies of 10^2 - 10^4 Hz obeys the law $\sigma_{ac} \sim f^{0.8}$. This indicates the presence of a hopping mechanism of charge transfer in states localized near the Fermi level. Doping the TlGaSe_2 crystal with erbium increases the density of states localized near the Fermi level and reduces their spread. An increase in the erbium concentration in $\text{TlGa}_{1-x}\text{Er}_x\text{Se}_2$ solid solutions leads to a decrease in the band gap and its temperature coefficient modulus.

- [1] D. Müller and H. Hahn: Zur Struktur des TlGaSe_2 . Z. Anorg. Allg. Chem. 438(1), 1978, 258-272.
- [2] E.M. Kerimova, S.N. Mustafaeva, D.A. Huseynova. Hard radiation detectors on A^3B^6 -based semiconductors and their complex analogues. Proceedings of Eurasia Conf. on nuclear science and its appl., Turkey, 2000, 394.
- [3] S. Johnsen, Z. Liu, J.A. Peters, J.-H. Song, S.C. Peter, C.D. Malliakas, N.K. Cho, H. Jin, A.J. Freeman, B.W. Wessels, M.G. Kanatzidis. Chem. Mater. 23, 2011, 3120-3128.
- [4] E.M. Kerimova. Crystal physics of low-dimensional chalcogenides. Baku, Elm, 2012.
- [5] S. Yang, M. Wu, H. Wang, H. Cai, L. Huang, C. Jiang, S. Tongay. Ultrathin ternary semiconductor TlGaSe_2 phototransistors with broad-spectral response. 2D Mater, 4(3), 2017, S1-S6.
- [6] S.N. Mustafaeva, V.A. Aliyev, M.M. Asadov. Physics of the Solid State, 40, 1998, 41-44.
- [7] S.N. Mustafaeva. Journal of Radio Electronics, 5, 2008, 1-11.
- [8] A.U. Sheleg, K.V. Iodkovskaya, N.F. Kurilovich. Physics of the Solid State, 40(7), 1998, 1328-1331.
- [9] S.N. Mustafaeva, M.M. Asadov, A.A. Ismayilov. Applied Physics 3, 2012, 19-23.
- [10] A.Cengiz, Y.M. Chumakov, M. Erdem, Y. Şale, F.A. Mikailzade, M.-H.Y. Seyidov. Origin of the optical absorption of TlGaSe_2 layered semiconductor in the visible range. Semicond. Sci. Technol. 33, 2018, 075019.
- [11] L.Yu Kharkhalisa, K.E. Glukhova, T.Ya Babuka, M.V. Liakha. Phase Transitions. A Multinational Journal, 2019, 92(5).
- [12] A.M. Panich. J. Phys.: Condensed Matter, 20 (29), 2008, 293202/1-42.
- [13] A.U. Sheleg, V.V. Shevtsova, V.G. Hurtavoy, S.N. Mustafaeva, E.M. Kerimova. Low Temperature X-Ray Investigations of TlInS_2 , TlGaS_2 and TlGaSe_2 Single Crystals. Surface. X-ray, synchrotron and neutron studies. 11, 2013, 39–42.
- [14] A.Say, D. Adamenko, O. Gomomai, I. Roman, I. Martynyuk-Lototska, R. Vlokh. Phase Transitions. A Multinational Journal, 2019, 92(9).
- [15] S.N. Mustafaeva, M.M. Asadov, E.M. Kerimova. Physics of the Solid State, 55(12), 2013, 2466-2470.
- [16] H.D. Hochheimer, E. Gmelin, W. Bauhofer, et al. Z. Phys. B. Condens. Matter, 73, 1988, 257-263.
- [17] N.F. Mott, E.A. Davis. Electronic Processes in Non-Crystalline Materials. Clarendon, Oxford, 1971.

Received: 02.06.2021

INVESTIGATION OF THE EFFECTS OF POLYMER-FERROCENE COMPOSITES

M.A. KURBANOV¹, A.F. GOCHUYEVA^{1,2}, F.F. YAHYAYEV¹, A.F. NURALIYEV¹

¹*Institute of Physics, Azerbaijan National Academy of Sciences,
H. Javid av. 131, AZ-1143, Baku, Azerbaijan*

²*National Aviation Academy, AZ-1045, Baku, Mardakan ave. 30
e-mail: aynuragochuyeva@gmail.com*

The article describes the effects observed in polymer-ferrocene composites. It is shown that in photo composites based on polymer (HDPE, PVDF) and di- π -cyclopentadienyl iron (π -C₅H₅)₂Fe, ferrocene), the effect of photo quenching of electrical conductivity under the action of light is observed. The photoelectret effect in PVDF-ferrocene composites is investigated.

Keywords: ferrocene, high density polyethylene, polyvinylideneflorid, electrical photo quenching, photoelectret

PACS: 78.66.Qn; 78.66.Sq

1. INTRODUCTION

A negative internal photoelectric effect was observed in the polymer-ferrocene composite. The essence of the negative internal photoelectric effect is a decrease in the electrical conductivity of a photosensitive material or a composite with a photosensitive component under the influence of electromagnetic or corpuscular rays. This effect is less noticeable than the usual internal photoelectric effect, which is an increase in the electrical conductivity of a substance under the influence of light [1-4]. The development of new light-sensitive polymer composites and the synthesis of their individual components (for example, metal compounds, various transition metal complexes) is a very important task. That is, the ability of these components to form composites with polymers with different properties has led to the emergence of new active materials with optical and electrical properties. Of particular importance is the proposed polymer-ferrocene composite (a metal compound of the di- π -cyclopentadienyl (π -C₅H₅)₂Fe type) with negative photoelectric properties. Also, in composites based on PVDF (polyvinylidene fluoride) and ferrocene, the photoelectric properties of the sample are determined by measuring the difference in electret potentials after polarization and determining the relaxation time of the electret load.

2. METHOD OF EXPERIMENT

The resulting composites were obtained as follows: powders of polymer and ferrocene (diameter \leq 50 μ m) were mechanically mixed, an approximately homogeneous system was obtained (mixing was carried out at room temperature); the volume of components in the mixture varies depending on the issue being addressed; samples from a homogeneous mixture (413-483) K in the temperature range, at a pressure of 15 MPa with a size of 20 x 10 x 0.07 mm were obtained by hot pressing. The magnitude of the photocurrent, photoresist and photovoltaic loads were measured with

an electrometric voltmeter (V7-30, U5-11). The light intensity varied in the range (200-400) mW / cm². The value applied to the component was taken equal to 100 V. An electrode system of two designs was used: 1) the distance between the electrodes of the concentric circle was 5 mm; 2) placed between two glasses with translucent metal electrodes on a composite sample.

Ferrocene and its oxygen derivatives can be used as additives to ensure the thermal stability of the polymer. The ionization potential of the ferrocene molecule is 6.72 eV. Analysis of the results obtained by various researchers shows that the ionization potential determined for ferrocene varies by up to 0.5 eV. It is also used as an inhibitor for the purposeful regulation of the oxidation of the polymer phase of thermic and photo-decomposition reactions of polymer matrix composites [5, 6]. Effective light-sensitive composite materials based on ferrocene have been obtained. If we take into account that ferrocene and its compounds are sensitive to the effects of light in the field of vision, then under certain conditions, the rotating photo may be subject to fragmentation.

In high-density polyethylene-ferrocene composites, the surface of which is exposed to light intensity of 400 mW / cm², the resistance of the composite increases 10 to 108 times when the volume fraction of ferrocene varies from 10% to 50%. That is, the permeability of the photo material decreases by the same amount (Figure 1.1, curve 2). Similar studies were performed for PVDF-ferrocene composites (Figure 1.1, curve 1). Given the stability of the applied voltage (U = 100V) and the intensity of the incident light (400 mW / cm²), the ratio of R_f / R₀ in PVDF matrix composites increased 6-67 times, while the volume fraction of the ferrocene phase in the composite varied from 10% to 50%. The results show very accurately that the effect of light extinction is more pronounced in non-polar matrix composites. It should be noted that the effect of photoconductivity extinction also depends on the intensity of the incident light. This effect is of great practical importance. For this purpose, the dependence of HDPE (80% volume fraction) - ferrocene (20% volume fraction) composites on the

intensity of incident light was studied. This dependence is shown in Figure 1.2. Here

$$tg \alpha = \frac{\Delta R_f}{\Delta E} = 18,85 \times 10^5 \frac{Om \cdot m^2}{W}$$

is the ratio of the change in the intensity of the incident light to the resistance of the composite under the influence of factor light. Figure 1.2 shows that the specific volume of the composite we are studying depends significantly on the intensity of the light falling on the resistor, and the value of the resistance increases nonlinearly with the intensity of the light.

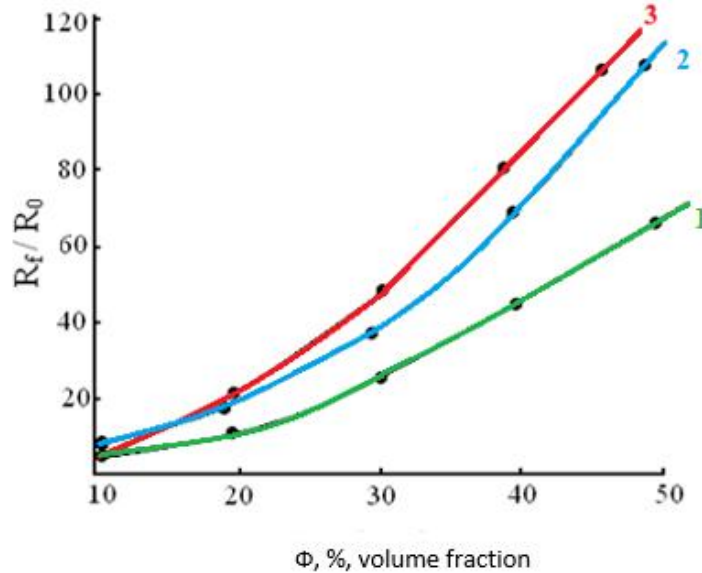


Fig. 1.1. Dependence of the ratio R_f / R_0 on the volume fraction of the composite ferrocene Φ , % phase 1. PVDF – ferrocene; 2. HDPE - ferrocene; 3. PVDF - ferrocene - 20% volume share CdS; $U = 100V$; $E_i = 400 \text{ mWt} / \text{cm}^2$.

To determine the role of ferrocene in the composite in the photoresist, the dependence of the photocurrent on the wavelength of incident light in different volumes of ferrocene is given. Studies show that the minimum value of the photocurrent, regardless of the volume fraction of ferrocene, corresponds to a value of 600 nm of light wavelength (Figure 1.3).

In polyolefins and halogen-containing polymers dispersed with ferrocene $(C_5H_5)_2Fe$, the photo quenching effect of light conductivity was observed.

Note that, this effect (photo-splitting) depends on the chemical and physical structures of the polymer phase we use in composites.

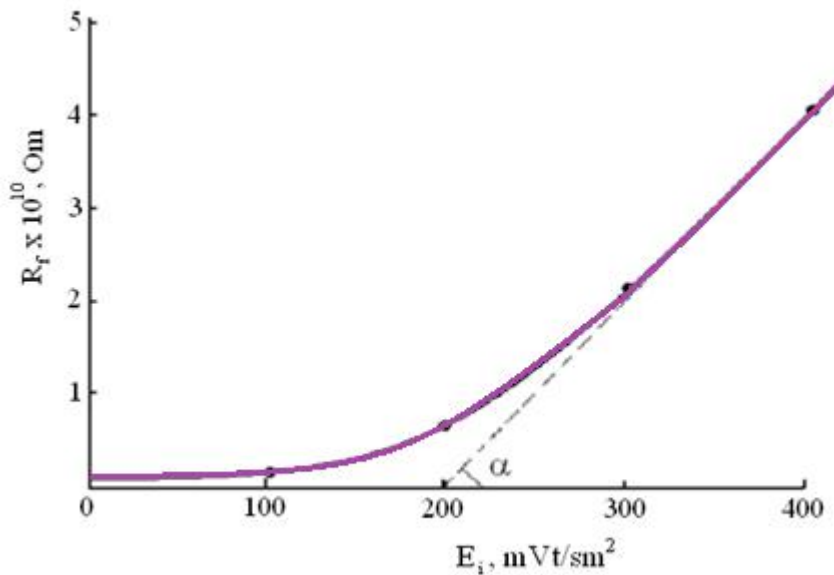


Fig. 1.2. The dependence of the photoresistance of HDPE-ferrocene composite on the intensity of incident light in the visible region of light. $U = 100V$, the volume share of ferrocene is 20%, the volume share of HDPE is 80%.

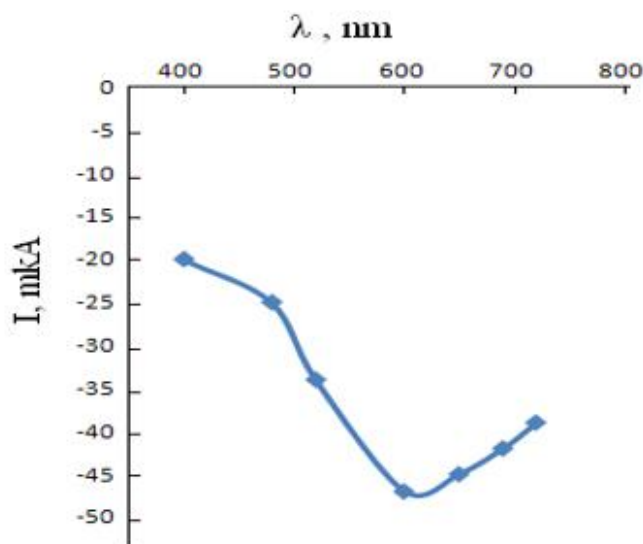


Fig. 1.3. Typical dependence of photocurrent on the wavelength of incident light for ferrocene-HDPE composites. Ferrosen - 40% volume fraction, $U = 100V$; $E_i = 400mVt / cm^2$.

If we analyze the nature of the applications of ferrocene, we can conclude that under the influence of light, many properties of ferrocene phase composites (thermal, mechanical, electromechanical), as well as the photoelectret effect, which is the main goal of our work, can be purposefully varied [7-9].

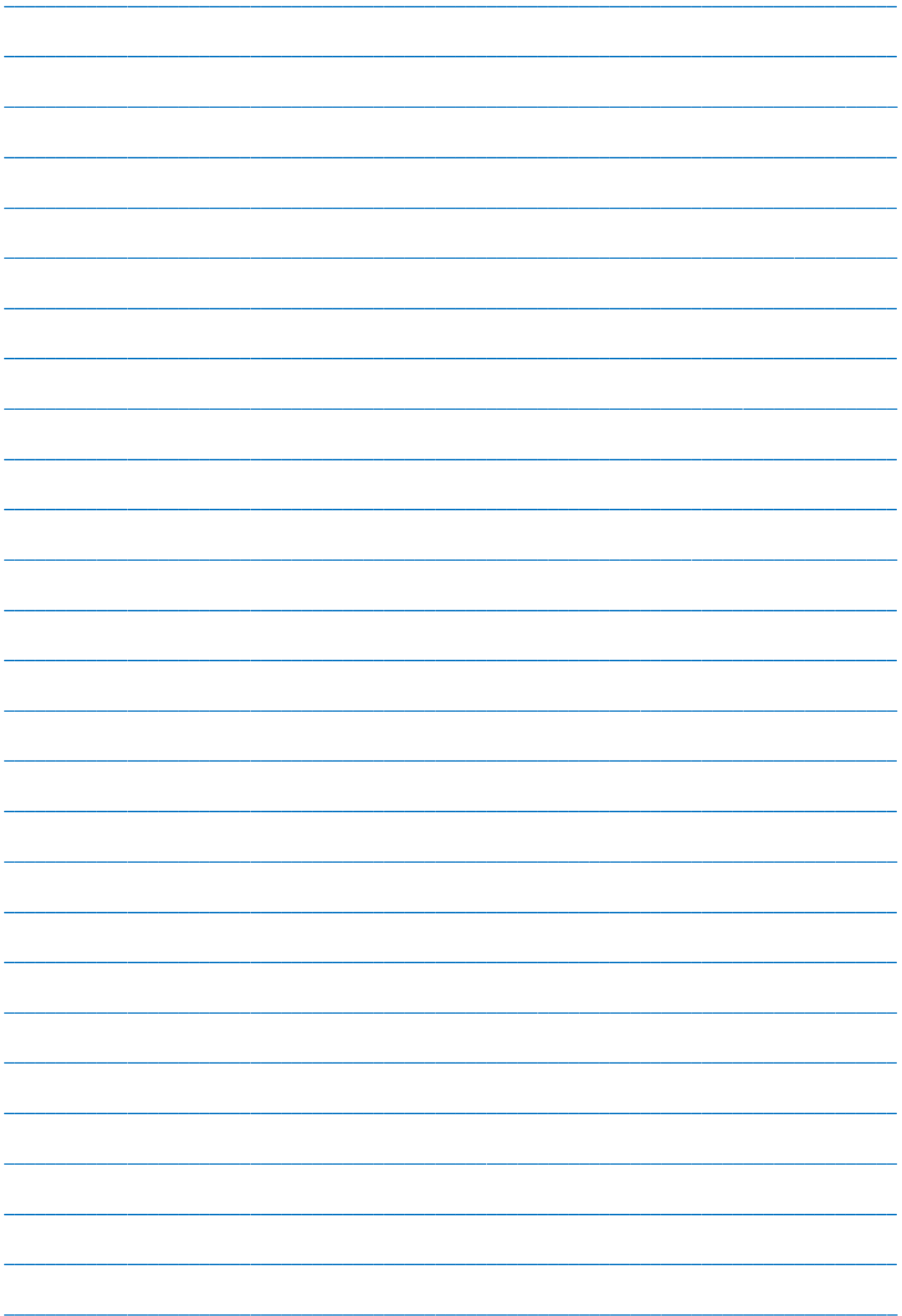
The electret properties of the investigated composite sample are determined by measuring the difference in electret potentials after polarization and determining the relaxation time of the electret load. It is assumed that the relaxation time of a photovoltaic cell based on a polymer-ferrocene composite is such that the difference between the electret load or the electret potential decreases to e [7].

3. CONCLUSION

Thus, in composites based on di- π -cyclopentadienyl iron ($(\pi - C_5H_5)_2 Fe$, ferrocene), the effect of photo quenching of electrical conductivity under the action of light was observed. The main reason for the formation of the effect of photo quenching of rotational conductivity in polyolefin-ferrocene composites is the formation of a local electric field in the direction opposite to the external field, as a result of the formation of multiply charged centers and a dipole moment in the ferrocene phase under the action of light. The photoelectret effect in PVDF-ferrocene composites is investigated.

- | | |
|---|--|
| <p>[1] Amorphous Semiconductors, Ed. M. Brodsky. M.: Mir, 1982, 419 p.</p> <p>[2] B.U. Barshevsky. Quantum - optical phenomena. M.: Higher school, 1988, 135 p.</p> <p>[3] V.S. Pershenkov, V.D. Popov, A.V. Shalnov. Surface radiation effects in the elements of integrated circuits. M.: Enegoatomizdat, 1998, 253 p.</p> <p>[4] J. Simon, J. André. J. Molecular semiconductors. Moscow: Mir, 1988, 342 p.</p> <p>[5] D.A. Lemenovsky. Sandwich metal complex connections. Ferrocene. Soros Educational Journal, 2, 1997, p. 64 – 69.</p> <p>[6] E.G. Perevalova, M.D. Reshetova, K.I. Grandverg. Research methods of organic chemistry. Ferrocene. M.: Nauka, 1983, 250 p.</p> | <p>[7] A.F. Gochuyeva. Photoelectret effect and photoquenching of the electrical conductivity in the polymer - $A^{II}B^{VI}$ and polymer-ferrocene composites: Ph.D dis. Baku, 2014, 197 p.</p> <p>[8] M.A. Kurbanov, G.Z. Suleymanov, N.A. Safarov, A.F. Gochueva, I.N. Orujov, Z.M. Mamedova. Physics and technology of semiconductors. April 2011, volume 45, issue 4, pp. 510 - 535</p> <p>[9] G.Z. Suleymanov, N.A. Safarov, A.F. Gochuyeva, M.A. Kurbanov, A.A. Bayramov, I.N. Orujov, E.A. Jafarova. Azerbaijan Journal of Physics. Volume XVI, Number 2, Series: En June, 2010, p. 378 – 652.</p> |
|---|--|

Received: 17.06.2021



CONTENTS

1.	Spectrum of laser pulses in the first order dispersion theory Sh.Sh. Amirov	3
2.	Photoluminescence properties of ZnIn ₂ Se ₄ I.A. Mamedova	8
3.	Free standing AAO nanoporous membranes for liquid filtration Sh.O. Eminov, A.Kh. Karimova, E.A. Ibrahimova, J.A. Guliyev	12
4.	The human perception and uncertainty in quantum physics E.A. Issaeva	17
5.	Influence of single-walled carbon nanotubes on dielectric and conductivity properties of smectic A liquid crystal with negative dielectric anisotropy T.D. Ibragimov, A.R. Imamaliyev, G.F. Ganizade, O.A. Aliyev	24
6.	Spatial structure of N ¹ H and N ³ H tautomers of carnosine in zwitterion form G.A. Akverdieva, I.N. Alieva, Z.I. Hajiyev, S.D. Demukhamedova	29
7.	Surface plasmon polariton observation at narrow-gap semiconductor Bi ₂ Se ₃ and Sb ₂ Te ₃ Elvin Husenaga Alizade	38
8.	Study of the effect of impurities and heat treatments on the structure of Se-As-EuF ₃ , Se-Te-Sm and Ge ₂ Sb ₂ Te ₅ films by X-ray diffraction and Raman spectroscopy S.N. Garibova, A.I. Isayev, S.I. Mekhtiyeva, S.U. Atayeva, S.S. Babayev	41
9.	Growth and characterization of ZnO:Eu thin films for solar cell application V.F. Gremenok, E.P. Zaretskaya, A.N. Pyatlitski, N. Akcay, T.V. Piatlitskaya, N.N. Musayeva	47
10.	Technique of solution concentration control of polar substance in nonpolar solvent S.T. Azizov	51
11.	TlGa _{1-x} Er _x Se ₂ solid solutions, their electrical and optical properties E.M. Kerimova, S.N. Mustafaeva, N.Z. Gasanov, K.M. Huseynova, Q.M. Sharifov	54
12.	Investigation of the effects of polymer-ferrocene composites M.A. Kurbanov, A.F. Gochuyeva, F.F. Yahyayev, A.F. Nuraliyev	61



www.physics.gov.az